Study of the Very High Energy emission of M87 through its broadband spectral energy distribution.

by

Fernando Josué Ureña Mena

Thesis submitted as partial requirement for the degree of

MASTER IN SCIENCES WITH SPECIALTY OF ASTROPHYSICS

at

Instituto Nacional de Astrofísica, Óptica y Electrónica

August 2020

Tonantzintla, Puebla

Supervised by:

Dr. Daniel Rosa González

Tenured Researcher - INAOE

Dr. Alberto Carramiñana Alonso

Tenured Researcher - INAOE

Dr. Anna Lia Longinotti

Conacyt Fellow - INAOE

Abstract

M87 is a giant radio galaxy, which is the central dominant galaxy of the Virgo Cluster. It is located at a distance of 6.5 Mpc ($z = 0.004$), and holds a supermassive black hole with a mass estimated in 6.5×10^9 $M_\odot$. Very High Energy (VHE) emission from M87 has been detected by Imaging Air Cherenkov Telescopes (IACTs) and recently by the High Altitude Water Charenkov (HAWC), which is a gamma-ray and cosmic ray observatory located in Puebla, Mexico. The mechanism that produces VHE emission in M87 remains unclear. This emission is thought to be originated in its prominent jet, which has been resolved from Radio to X-rays.

In order to explain the VHE emission of M87, a broadband Spectral Energy Distribution (SED) of M87 has been constructed and fitted by a lepto-hadronic emission model. Emission from radio to GeV gamma rays has been modeled to be produced by Synchrotron Self Compton (SSC) emission. In this scenario, an electron population moving at relativistic velocities in the M87 jet is accelerated by a random oriented magnetic field. Therefore, electrons emit synchrotron radiation which is responsible for a low energy SED component from radio to X-rays. Synchrotron photons are Inverse Compton upscattered by the same electron population producing the high energy SED component.

However, according to some authors, SSC models are not able to explain the Very High Energy (VHE) emission detected in M87. That is why an additional component has been included to produce this emission. This component corresponds to radiation produced by photohadronic cascades which are generated after the interaction between Inverse Compton photons and Fermi accelerated protons in the jet. The gamma-ray emission has been assumed to be produced in the M87 core which corresponds to the inner jet. This is based on results obtained by variability studies. Core multiwavelegth data have been collected from those bands in which core emission is constrained. The SED has been constructed to be representative of the non-flaring activity of the core. VHE emission data have been obtained from IACTs reported results and the High Altitude Water Cherenkov (HAWC) observations.

Best fit values for the model fitting parameters were obtained. Errors were estimated using Monte Carlo simulations. HAWC observations were used to obtained the mean values of the fitting parameters for the 2014-2019 period, which corresponds to a low activity period at VHE.

Resumen

M87 es una radio galaxia gigante, la cual es la galaxia central dominante del cúmulo de Virgo. Está localizada a una distancia de 6.5 Mpc ($z = 0.004$) y alberga un agujero negro supermasivo con una masa estimada en 6.5×10^9 $M_\odot$. Emisión de muy alta energía de M87 ha sido detectada por Telescopios Cherenkov de Aire (IACT, por sus siglas en inglés) y recientemente por el High Altitude Water Charenkov (HAWC), el cual es un observatorio de rayos cósmicos y rayos gamma ubicado en Puebla, México. El mecanismo que produce la emisión de muy alta energía en M87 no está aún claro. Se piensa que esta emisión se origina en su prominente chorro de partículas, el cual ha sido resuelto desde el radio hasta los rayos X.

Con el objetivo de explicar la emisión de muy alta energía de M87, se construyó una distribución espectral de energía de M87 y se le ajustó un modelo de emisión leptohadrónico. La emisión desde el radio hasta los rayos gamma de GeV se modeló como producida por emisión de sincrotrón auto Compton. En este escenario, una población de electrones moviéndose a velocidades relativistas en el chorro de M87 es acelerada por un campo magnético aleatorio. Por lo tanto, los electrones emiten radiación de sincrotrón la cual es responsable de una componente de baja de energía de la distribución espectral desde el radio hasta los rayos X. Fotones de sincrotrón son posteriormente dispersados mediante efecto Compton inverso por la misma población de electrones produciendo una componente de alta energía.

Sin embargo, de acuerdo con algunos autores, los modelos de sincrotrón auto Compton no son capaces de explicar la emisión de muy alta energía detectada en M87. Por tal motivo una componente adicional ha sido incluida para producir dicha emisión. Esta componente corresponde a radiación producida por cascadas fotohadrónicas las cuales se generan luego de la interacción entre fotones de Compton inverso y protones acelerados por mecanismo de Fermi en el chorro relativista. Esto se basa en resultados obtenidos por estudios de variabilidad. Se recolectaron de la literatura datos multifrecuencia provenientes del núcleo de M87 en aquellas bandas en que este ha sido resuelto. La distribución espectral de energía ha sido construida para ser representativa de la ac-

tividad no destellante del núcleo. La emisión de muy alta energía ha sido obtenida de los resultados reportados por telescopios Cherenkov de aire y de las observaciones de HAWC.

Se obtuvieron valores de mejor ajuste para los parámetros de ajuste del modelo. Los errores fueron estimados con simulaciones de Monte Carlo. Las observaciones de HAWC fueron utilizadas para obtener los valores de mejor ajuste de los parámetros para el periodo 2014-2019, el cual corresponde a un periodo de baja actividad a muy altas energías.

A mi familia.

Contents

Chapter 1
Introduction

Gamma rays are the most energetic electromagnetic radiation, and they are tracers of the most energetic phenomena in the universe. Active Galactic Nuclei (AGN) are the most important sources of extragalactic gamma-rays. Some of them present Very High Energy (VHE) emission in the TeV band, which is thought to be produced in their relativistic jets [1]. The physical processes involved in this emission include leptonic scenarios such as Synchrotron Self Compton (SSC) [2] and hadronic mechanisms such as photohadronic cascades [3]. Most of AGNs that are VHE emitters are classified as blazars, whose jets are pointing very nearly towards the observer. As jets travel at nearly the speed of light, relativistic beaming increases the bright of these objects. Radio galaxies correspond to the misaligned counterparts of blazars and VHE emission have been detected from six of them [4]. Since radio galaxies are located closer on average than blazars, it is possible to perform more detailed observations to test theoretical models of their emission.

The High Altitude Water Cherenkov (HAWC) gamma-ray observatory has been able to detect four blazars and one radio galaxy after 1523 days of observations. The detected radio galaxy, M87, was previously detected by Imaging Air Cherenkov Telescopes (IACTs) [5]. It presents a complex behaviour at VHE and its emission mechanism remains unidentified [6]. However, IACTs perform observations with a a few hours of exposure time. As HAWC results constitute 4.5 years of almost continuous observations, they are constraining the actual average VHE emission of the source.

The main goal of this thesis is explaining the VHE emission of the radio galaxy M87 in both high activity and low activity states. A lepto-hadronic model, which combines Synchrotron Self Compton and photohadronic scenarios, has been used. A Python code has been developed to simulate the broadband emission of M87. An average SED of M87 has been constructed collecting multifrequency observations from data archives.

The constructed SED has been fitted by the emission model. The best fit values of

the emission zone physical parameters (magnetic field intensity, Doppler factor, electron energy distribution parameters and proton energy distribution parameters) have been obtained. HAWC data are used to constrain the average values of such parameters for the 2014-2019 period in which VHE flares have not been reported. VHE data from IACTs have been also fitted for comparison.

This thesis is organized as follows: Chapter 2 is about AGNs and the radiative processes involved in their emission, Chapter 3 describes characteristics of M87 and mentions problems regarding its VHE emission, Chapter 4 provides a description of the HAWC gamma-ray observatory and reports the last results of its AGN observations, Chapter 5 explains the emission model, Chapter 6 describes the data and methods used in this thesis, Chapter 7 reports the obtained results and Chapter 8 discusses results and gives the final conclusions of this work.

Chapter 2
Active Galactic Nuclei

2.1 Active Galactic Nuclei

According to [7] the terms "Active Galactic Nuclei" (AGN) and "Active Galaxies" refer to those extragalactic objects with a compact nuclear region that emits significantly beyond what is expected from stellar processes. The most plausible explanation for this phenomenom is the presence of accreting supermassive black holes (SMBHs) in their centers.

Accretion is considered one of the most efficient processes in astrophysical objects to emit energy. It consists in "the accumulation of diffuse gas or matter onto some object under the influence of gravity" [8]. When matter reaches the surface of the object its remaining kinetic energy can be radiated. Therefore, the accretion luminosity of an object is given by,

$$L = \frac{GM\dot{m}}{r} = \left(\frac{r_s}{r}\right)\frac{\dot{m}c^2}{2}, \tag{2.1}$$

where G is the gravitational constant, M the mass of the accreting object, r the radius of the accreting object (assuming spherical symmetry), $\dot{m}$ is the accretion rate (accreted mass per unit time), c is the speed of light in vacuum and r_s is the Schwarzschild radius (defined as $r_s = 2GM/c^2$). In the case of black holes additional complications result from the lack of a solid surface. However, the innermost stable circular orbit (ISCO), which is the last position that a particle can reach without being absorbed by the black hole, can be use to estimate the accretion luminosity . For a non-rotating black hole the ISCO radius is $3r_s$ [9] and its accretion luminosity L_{BH} is given by:

$$L_{BH} = \frac{1}{6}\dot{m}c^2 \tag{2.2}$$

In general, equation 2.1 can be rewritten in a simpler form:

$$L = \eta\dot{m}c^2, \tag{2.3}$$

where η is the efficiency of conversion which depends on the object type. The value of η increases as the objects are more compact since $\eta \propto M/r$ [10], which makes accretion in black holes more efficient than in many other astrophysical systems. In the case of rotating black holes the value of η also depends on their spin [11].

In the case of AGNs, angular momentum dissipation plays an important role. Falling particles acquire angular momentum and tend to form a disk around the accreting object. Particles in the accretion disk loose angular momentum due to turbulent viscous forces and move inwards until finally being accreted (otherwise they would form stable Keplerian orbits)[8].

For some authors these SMBHs have to exceed an Eddington ratio (L_{AGN}/L_{Edd}) of about 10^{-5} [12] where L_{AGN} is the bolometric luminosity of the AGN and L_{Edd} is the Eddington luminosity (luminosity for which the radiation pressure balances the gravitational force in a system [8]) of a solar composition gas $L_{Edd} = 1.5 \times 10^{38} M_{BH}/M_{\odot}$ erg s[1] [12]. However, this limit is somewhat arbitrary.

AGNs present many interesting and peculiar properties including [13]:

- Luminosities among the highest in the universe (up to $L_{bol} \approx 10^{48}$ erg s^{-1} assuming isotropy).
- Rapid variability (mostly in optical, UV, X-rays and gamma rays), which implies a small emitting region.
- Spectral features which can not be produced by stellar emission like strong emission at radio frequencies and high energies (see Figure 2.1 for a comparison between the spectral energy distribution of the Active Galaxy M87 and the starburst galaxy M82).

2.1.1 Structure

Most AGNs include the following components [12]:

1. Super massive black hole (SMBH): it is considered the central engine of every AGN phenomenon. They have a mass in the range of $10^6 - 10^{10}$ $M_{\odot}$ [16] which

[1] https://ned.ipac.caltech.edu/

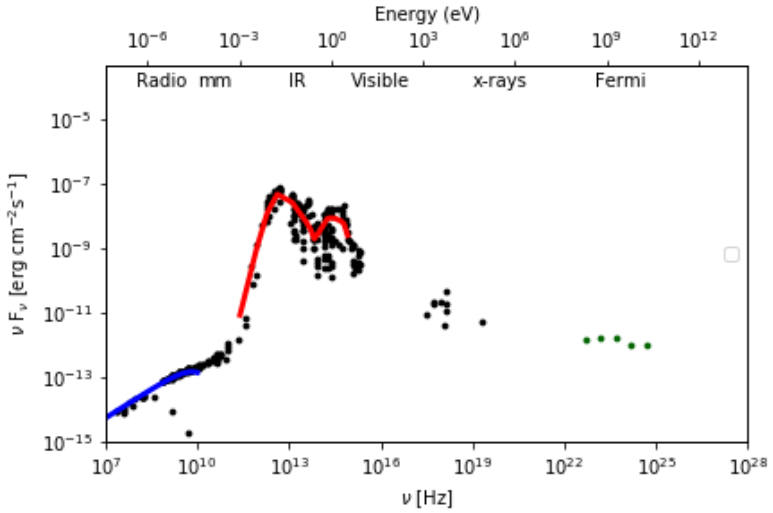

(a) Broadband SED of M82.

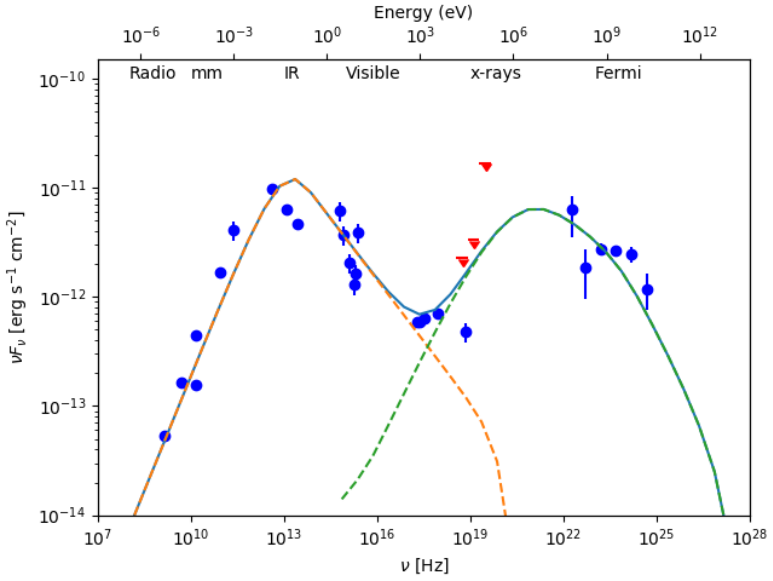

(b) Broadband SED of the active galaxy M87.

Figure 2.1: Comparison between the broadband SED of the starburst galaxy M82 (a) and the broadband SED of the AGN M87. Historical data points (black points) of M82 were obtained from the NASA/IPAC Extragalactic Database [1]. Green points correspond to *Fermi* LAT results [14]. A synchrotron radio emission model (blue curve) [15] and a stellar emission template (blue curve) are also marked. The SED of M87 has been constructed with data (blue and red data points) described in Chapter 6 and fitted by a model of jet emission that includes synchrotron emission (orange dashed line) and inverse Compton emission (green dashed line) which is described in Chapter 5. As M82 is a starburst galaxy, its SED is dominated by stellar and interstellar emission. However, an AGN is also present in M82.

can be measured through several methods including reverberation mapping [17], its relation with stellar velocity dispersion [18] and even direct imaging [19]. According to the their dynamics black holes can be classified as stationary (without rotation and modeled with the Schwarzschild metrics) and rotating (modeled with the Kerr metrics). Rotating black holes can generate rotating magnetospheres around them which can produce centrifugal acceleration of particles [20, 21].

2. Accretion disk: A subparsec accretion flow which probably has a flattened structure [7]. The physics of this component is an active research topic. However, a useful approximation is the Shakura-Sunyaev model (an optically thick but geometrically thin accretion disk) [22]. Accretion disk mostly emits in optical and UV bands.

3. Broad-Line Region (BLR): It is composed by dust-free gas clouds which move in a roughly keplerian way (with velocity ~ 3000 km s^{-1}) at a distance of around 1 parsec from the black hole. Its typical numerical density is around 10^{10}cm^{-3}. In this region are thought to be produced the broad lines seen in many AGN spectra (with Doppler widths of $10^3 - 10^4$ kms^{-1}) [7, 12], which are observed in optical bands.

4. Torus: it is an axisymmetric structure of dense gas and dust located between 0.1 and 10 pc from the black hole that can block part of the nuclear emission [7]. Optical and UV emission absorbed by the torus is reemitted at infrared bands.

5. Narrow line region (NLR): It is composed by slower (velocity $\sim$ 300 km s^{-1}) and less dense ($\sim 10^4$ cm^{-3}) ionized gas than the BLR [7, 12]. Narrow optical emission lines, which are characteristic of many AGN spectra, are thought to be produced in this region.

6. Jet: It is not present in all AGNs. Relativistic jets are formed when the black hole is spinning in the presence of a strong magnetic field. In jets, protons may be accelerated at the highest energies, producing that AGNs being considered as contributors of the cosmic ray spectrum. They are also thought to be the origin of gamma rays. Jets exist on scales from ~ 1 AU to ~ 1 Mpc, and have been resolved from radio to X-rays. [1].

2.1.2 Classification

AGNs incorporate a wide variety of different objects. This has given origin to a complex "taxonomy" of Active Galaxies which includes LINERs, Seyfert galaxies, quasars, QSOs, blazars, radio galaxies, etc.

AGNs can be classified in different ways. The most common are [7]:

- Radio classification: Radio-loud AGNs are characterized by the presence of jets and lobes which produce a strong radio emission. Radio-quiet AGN radio ejecta are energetically less significant [23]. The distinction between the two classes is usually made by the "radio loudness parameters" (R) which is defined as the ratio between the radio flux at 5 GHz and the optical flux in the B band. AGNs with $R \sim 10$ or higher are considered Radio Loud [24].

- Type 1 and type 2 AGNs: This division is based on UV, optical, Mid-Infrared and X-ray spectroscopy [7]. Some Active Galaxies spectra present broad Balmer lines and narrow forbidden lines. Those are classified as type 1. On the other side there are active galaxies whose spectra present both narrow Balmer and narrow forbidden lines which are called type 2. In the case of Seyfert galaxies there are many intermediate cases (1.1,1.2,...,1.9). Moreover, those AGN with almost no presence of emission lines are called type 0 [25].

Unification schemes consider that the differences among types of AGNs are due to their orientations toward the observer (a schematic representation of AGNs structure and its relation with classification is shown in Figure 2.2). The orientation relative to the observer would produce different beaming effects as well as different absorption in the inner AGN structures [26, 27]. Unification schemes usually refer to two different categories. The first tries to explain the difference between type 1 and type 2 AGNs by the presence of a central dusty torus. In that scheme, for some orientation angles the dusty torus blocks the emission coming from the surroundings of the black holes, causing obscuration of spectral features like the broad emission lines and the X-ray continuum in type 2 AGNs. However, the lack of coincidence between visible and X-ray classifications in many objects has been unfavourable for those unification schemes [28]. The second category, which is used in this work, explains the characteristics of radio-loud AGNs by the orientation of their jets [29].

2.2 Blazars and radio galaxies

Blazars and radio galaxies are two types of radio-loud AGNs. According to unification schemes [27, 26] they are considered to be the same kind of objects with different orientation angles.

Blazars constitute the vast majority of extra galactic gamma ray sources [30]. They are characterized by having compact radio cores, high-amplitude multi-wavelength variability and large radio and optical polarization [31]. Those characteristics are thought to be produced because their jets are closely aligned with our line of sight

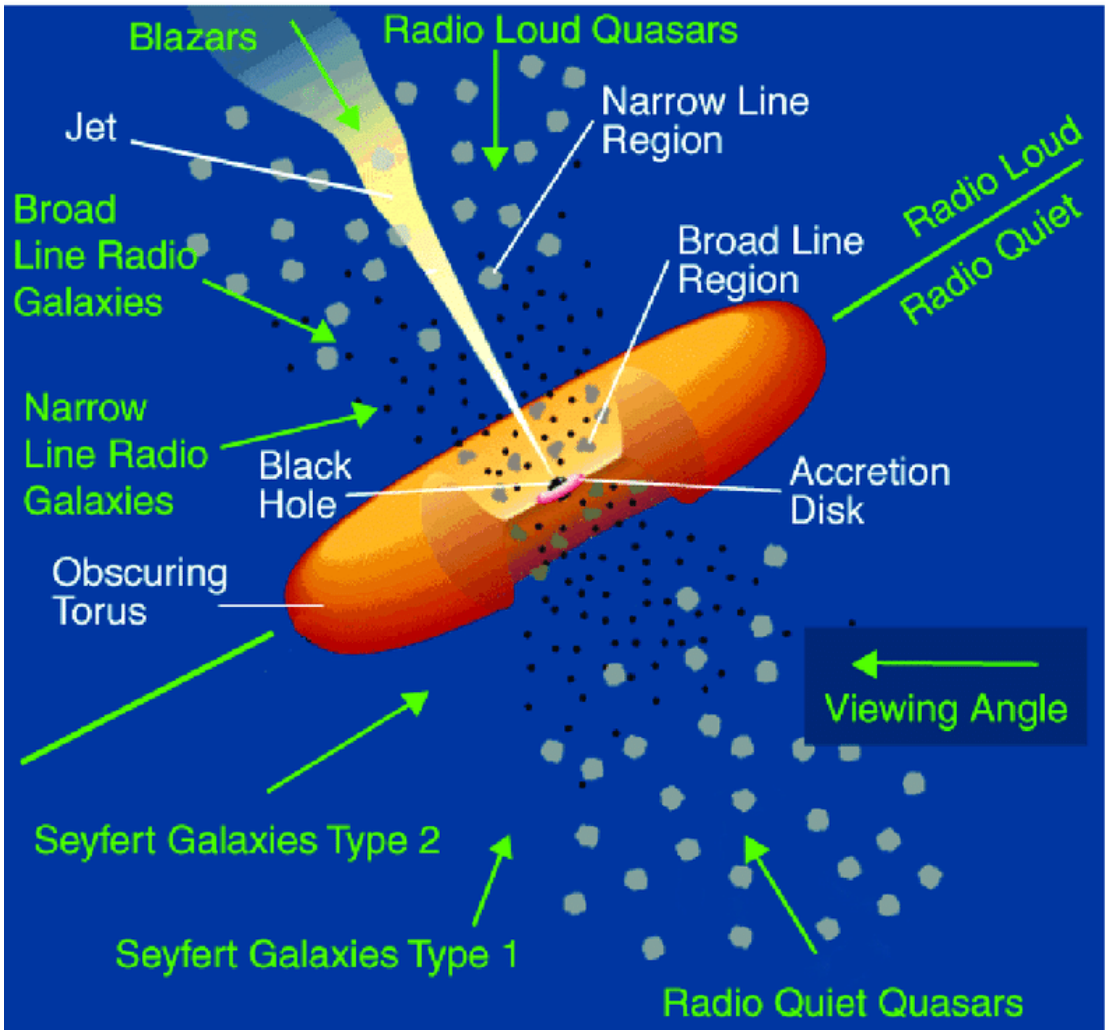

Figure 2.2: Unification model of AGNs proposed by [27]. The green arrows represent the viewing angle which is considered to be a key parameter in unification schemes. Types of AGNs are presented in green text. Structure names are written in white text. Radio-loud and radio-quiet cases are represented. In the case of Radio-loud AGNs the emission is shown to be dominated by a jet.

becoming dominant in their emission. They are classified into two different subclasses [32]:

- BL Lacertae (BL Lac) objects: These objects are distinguished by their weakness or absence of emission lines [2]. They have a non thermal continuum emission and polarization vectors which are parallel to the jet orientation [31]. Since they have an almost featureless spectrum their redshift determination becomes very difficult or even impossible sometimes [33]. Since BL Lacs have been usually found in groups of galaxies, an alternative to estimate their redshifts is using galaxies of their environments [34, 35]. In MeV-GeV energies they usually have hard spectra with $\Gamma_\gamma < 2$ with a photon flux N defined as function of energy E by $N \propto E^{-\Gamma_\gamma}$ where Γ_γ is the spectral index. [36].
- Flat Spectrum Radio Quasars (FSRQ): they are distinguished by the presence of luminous broad emission lines which are often accompanied by prominent ultraviolet–optical continuum emission (*blue bump*) of thermal origin [31] .This indicates the presence of accretion-disk radiation and a dense BLR [37]. They were the majority of blazars detected by the Energetic Gamma Ray Experiment Telescope (EGRET) which was active between 1991 and 2000 in the 30 MeV-30 GeV energy range [38]. However, BL Lacs constitute the majority of blazars detected by the *Fermi* Large Area Telescope (LAT) which works in the 20 MeV-300 GeV energy range [14]. FSRQs usually have softer gamma ray spectra $\Gamma_\gamma > 2$ and are located at higher redshifts than BL Lacs [36].

According to unification schemes radio galaxies correspond to the misaligned counterpart of blazars. They are classified into two main types based on their radio morphology [39, 4]:

- Fanaroff-Riley I (FR-I): which are lower radio luminous and edge-darkened sources.
- Fanaroff-Riley II (FR-II): higher radio luminous and edge-brightened sources. Bright hot spots characterize their radio lobes.

The radio luminosity transition between FR-I and FR-II was originally established in 2×10^{25} W Hz^{-1} sr $^{-1}$ at 178 MHz. More recent studies have found much overlap between radio luminosities of both kinds of objects but FR-II have $\sim$3 times higher average radio luminosity than FR-I [40]. FR-I radio galaxies are thought to be the misaligned counterparts of BL Lacs and FR-II radio galaxies presumably corresponding to the misaligned counterparts of FSQRs [27].

A total of 36 sources in the *Fermi* LAT 4FGL catalog are associated with radio galaxies and 6 are identified as such [14]. Moreover, the TeVCat includes 6 radio galaxies [41].

Blazars and radio galaxies are noticeable for their importance in multimessenger astronomy . AGNs and radio galaxy lobes have been proposed as possible sources of Ultra High Energy Cosmic Rays (UHECR) which are defined as cosmic rays with energies greater than 10^{18} eV [42]. According to results of the Pierre Auger Observatory, the arrival directions of UHECR present a large-scale anisotropy which is in agreement with an extragalatic origin [43]. Moreover, in September 2017 the neutrino observatory Ice Cube reported the detection of a neutrino with an energy of $\sim$ 290 TeV coming from a position in the sky coincident with the blazar TXS 0506+05. This detection was also coincident in time with a 6-month long gamma-ray flare, as it was revealed by a multifrequency campaign. Those coincidences were statistically interpreted as a possible neutrino emission from TXS 0506+056 [44]. Neutrino emission favors hadronic and lepto-hadronic processes to model the SED of AGNs. Those models are explained with more detail in Section 2.3.

2.3 Radiative Processes in AGN jets

The broadband spectral energy distributions (SED) of AGN jets (which are prominent in the emission of blazars and radio galaxy cores) are globally non thermal and they are characterized by the presence of two components or peaks. [1] (see Figure 2.3 for an example of a blazar SED). The low energy component is usually attributed to synchrotron emission. This emission is produced when relativistic particles are accelerated in the presence of a magnetic field [45]. In this case it is produced by an electron population moving in the relativistic jet. It is important to mention that the power of the synchrotron emission depends on the particles mass, that is why electrons (instead of protons or muons) have been postulated to produce this emission. If the particle energy distribution is a power law with index p over a sufficiently broad energy range:

$$N_e \mathrm{d}\gamma \propto \gamma^{-p} \mathrm{d}\gamma, \tag{2.4}$$

where γ is the electron Lorentz factor and N_e is the particle number density with Lorentz factors between γ and $\gamma + \mathrm{d}\gamma$. Then the radiation spectrum is also a power law

$$P(\omega) \propto \omega^{-\alpha}, \tag{2.5}$$

where ω is the emission frequency and P the emitted power per unit of frequency, whose index is related to the particle distribution index by [45]

$$\alpha = \frac{p-1}{2}. \tag{2.6}$$

A process called synchrotron self absorption prevents the brightness temperature of the electrons to be higher than their actual temperature (assuming local thermodynamic

equilibrium). This effect would produced an absorbed component in the synchrotron emission at low frequencies where [8]:

$$P(\omega) \propto \omega^{5/2}. \tag{2.7}$$

At higher frequencies the mean free path of the electrons is higher than the size of the region, letting them to escape, and the synchrotron spectrum behaves according to Equation 2.5.

On the other hand, the second peak (see Figure 2.3 for an example of a blazar SED where the two components are clearly distinguished) has been explained by many different models. These models can be divided into two types:

- Leptonic models: in these models the high energy component of the broadband SED is explained as inverse Compton (IC) emission produced by an electron population in the jet. In inverse-Compton scattering relativistic electrons scatter low energy photons to higher energies [8] . Unlike the Compton effect, in IC it is the photons that obtain energy from the electrons. If a photon of frequency ω_0 is upscattered by an electron with Lorentz factor γ_0 and $\hbar\omega_0\gamma_0(1 - \beta_0 \cos\theta_0 \ll m_e c^2)$ (where θ_0 is the angle between the electron trajectory and the photon, β_0 is ratio between the electron speed and the speed of light and m_e is the electron mass) the frequency of the outgoing photon (ω_1) will be:

  $$\omega_1 \sim \gamma^2 \omega_0, \tag{2.8}$$

  which means that the energy of the photons increase by a factor γ^2. However, when $\hbar\omega_0\gamma_0(1 - \beta_0 \cos\theta_0 \gg m_e c^2)$ the value of ω_1 will be:

  $$\omega_1 \sim \gamma m_e c^2/\hbar, \tag{2.9}$$

  which means that the energy of the outgoing photons will be of the order of the electrons energy.

  The seed photons for the Compton scattering could be external or they could be produced by the same electron population. In External Compton (EC) models the seed photons may have diverse origins. They could come from another region in the jet, another structure close to the black hole (such as the accretion disk, BLR or dust torus) or even the cosmic microwave background [46].

  In Synchrotron-Self Compton (SSC) models the second peak is produced by synchrotron photons which are upscattered by the same electron population that generated the synchrotron emission [47]. There are many variations of this mechanism. In one-zone SSC models all the electrons are confined in a single volume.

On the other hand, multi-zone SSC models assume the existence of multiple regions in the jet whose emissions are added to obtain the observed broadband SED [48].

- Hadronic models: in these cases the second component is produced by mechanisms involving hadrons (especially Fermi accelerated protons). The most common are proton synchrotron emission, proton-pion production and photo-pion production by energetic protons (the last two followed by pion and muon decays). The products of the different pion decays are [47]:

$$\begin{cases} \pi^0 \rightarrow \gamma + \gamma \\ \pi^{\pm} \rightarrow \mu^{\pm} + \nu_{\mu} \rightarrow e^{\pm} + \nu_e + \nu_{\mu} + \nu_{\mu} \end{cases} \tag{2.10}$$

  where π^0 are neutral pions, $\pi^{\pm}$ are charged pions, $\mu^{\pm}$ are antimuons/muons, γ are gamma ray photons, ν_e are electron neutrinos, ν_{μ} muon neutrinos and $e^{\pm}$ are positrons/electrons. Pion decays produce both gamma rays and neutrinos making hadronic models very important for extragalactic neutrino astronomy. As they require injection of accelerated protons, hadronic models are also relevant to explain the origin of Ultra High Energy Cosmic Rays [49].

Sometimes the same data can be modeled with two different scenarios, for example Figure 2.3 shows the Blazar Markarian 421 SED fitted by two different models [50]. In those cases, other criteria like variability have to be considered. Hybrid models that combine both kinds of mechanisms can also be found in literature [51].

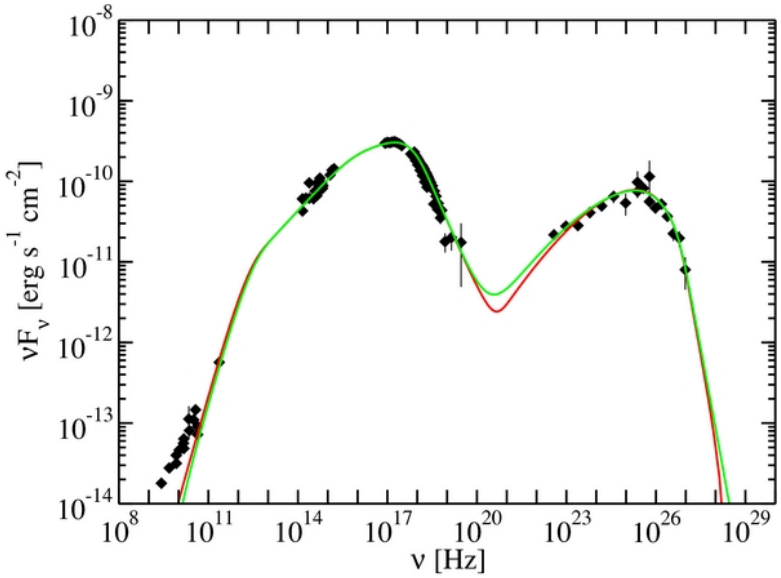

(a) One-zone SSC model fit

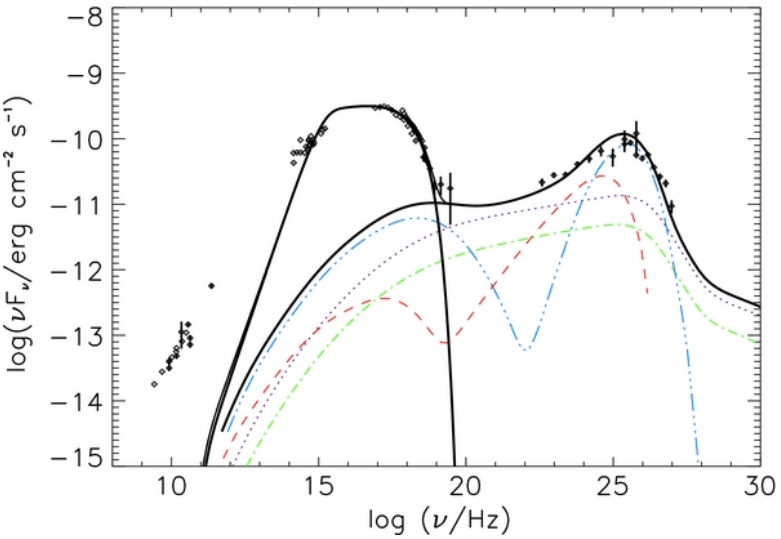

(b) Hadronic model fit

Figure 2.3: SED of the blazar Mrk 421 with two different fits [50]. According to [50] the observational data were obtained during a 4.5 month long multifrequency campaign. Panel (a) presents the fit of a one-zone SSC model with two variability times: 1 day (red curve) and 1 hour (green curve). Panel (b) corresponds to the fit of hadronic model with several components π^0- cascade (black dotted line), $\pi^{\pm}$cascade (green dash-dotted line), $\mu-$synchrotron and cascade (blue triple-dot-dashed line) and proton synchrotron and cascade (red dashed line). The first component was modeled as electron synchrotron, the black solid line corresponds to the sum of all components.

Chapter 3

The radio galaxy M87

3.1 General characteristics of M87

M87 (R.A. $12^{\rm h}30^{\rm m}47^{\rm s}.2$ Dec.$+12^{\circ}23'51''$) is a giant radio galaxy (see Figure 3.2 for a picture) which is the central dominant galaxy of the Virgo Cluster. It is located at a distance of 16.7 $\pm$ 0.2 Mpc [52] ($z = 0.0044$), which was obtained through the method of surface brightness fluctuations (SBFs). It is an elliptical galaxy with a diameter of $\sim$ 300 kpc [53], a dynamical mass within 180 kpc estimated in $(1.5 \pm 0.2) \times 10^{13}\ M_{\odot}$ [54] and an old (mostly $\gtrsim 1$ Gyr) stellar population [55]. It hosts a super massive black hole named M87* whose shadow was the first imaged by the Event Horizon Telescope [56]. Those observations have revealed a ring of $\sim$ 0.45 μas which is equivalent to 12 r_g (gravitational radius $r_g = GM/c^2$) for a mass estimated in 6.5 $\times 10^9$ $M_{\odot}$ [19].

One of its most noticeable characteristics is its prominent jet which has been studied for the last hundred years [57]. This jet has a length of about 2.5 kpc [58] and it has been resolved from radio to X-rays (see Figure 3.3). Among its main properties the most relevant for this thesis are [5]:

- Complex structures like knots and diffuse emission [59, 60]. One of its most interesting features is a group of bright knots called "*HST*-1", which is located around $0''.8 - 1''.0$ ($62 - 78$ pc) from the core. This feature has been resolved in a wide range of frequencies from radio to X-rays [61].
- Apparent superluminal motion [62]. It is a phenomenon in which bright radio components in relativistic jets appear to move at velocities higher than the speed of light due to a geometric effect [8]. In the case of the M87 jet, it was reported to have features with superluminal motion ($\sim 2 - 6c$), including *HST*-1, up to ~ 200 pc away from the nucleus [58].

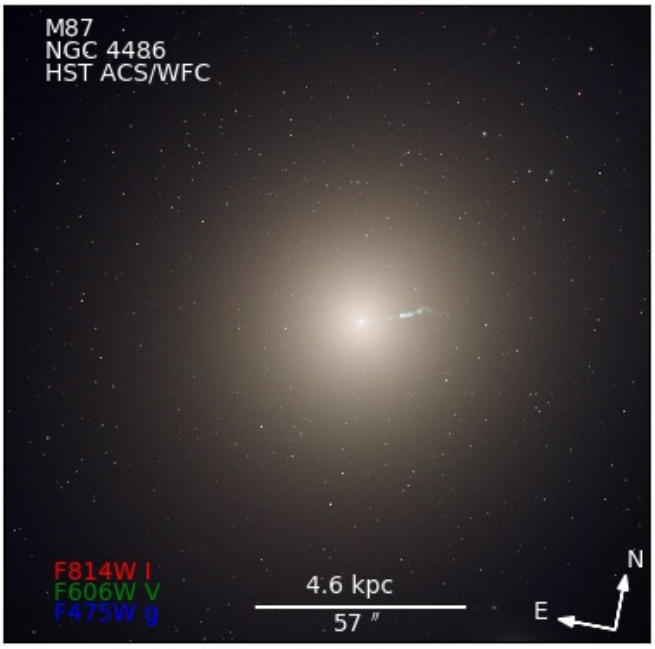

Figure 3.1: Visible image of M87 by the *Hubble Space Telescope*. It is composed by three different filters F814W, F606W and F475W. The elongated structure on the right of the galaxy corresponds to the jet. Image adapted from `https://hubblesite.org/contents/media/images/2008/30/2386-Image.html?news=true`

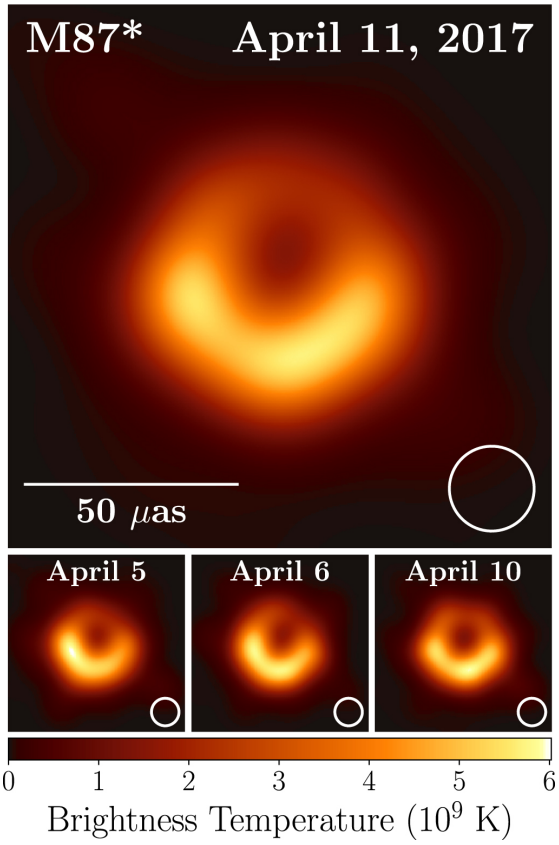

Figure 3.2: Image of the M87* shadow made by the Event Horizon Telescope [56]. Observations from four different dates are shown. The dark region at the center corresponds to the shadow. The luminous ring around the shadow is formed by lensed photons from the accretion disk. The observations were made at 1.3 mm.

- Complex variability [63] which includes a long term flare in the jet feature *HST*-1 from 2001 to 2008 whose peak was coincident with a Very High Energy (VHE) gamma ray flare in 2005 (more details about variability of M87 in Section 3.2).

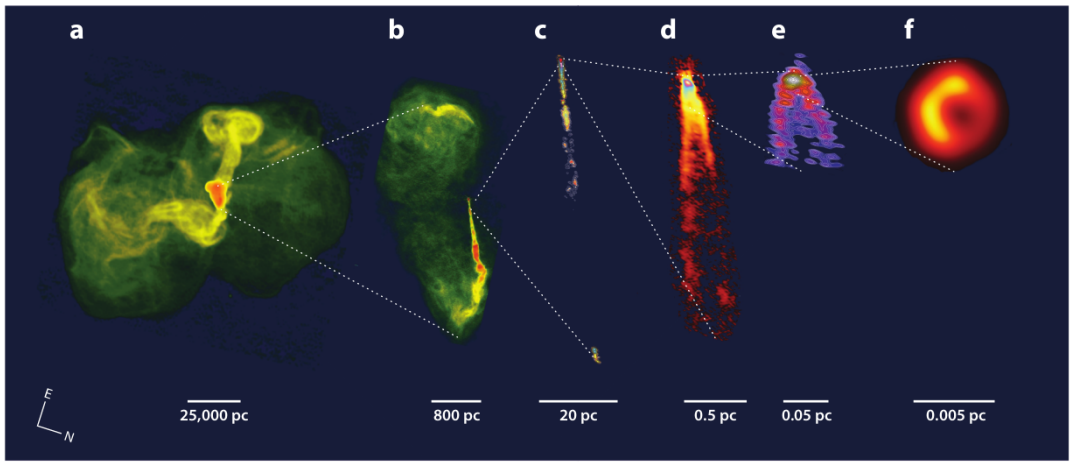

Figure 3.3: Jet of M87 imaged at different scales taken from [1].(a) Lobe jet and outer lobes, image adapted from NRAO, 90-cm VLA [scale: 25 000] (b) galaxy jet and inner lobes, 20-cm VLA [scale: 800 pc] (c) full view of the black hole jet including *HST*-1, 20-cm VLBA [scale: 20 pc] (d) innermost jet, 7-mm VLBA [scale: 0.5 pc] (e) jet launching region near supermassive black hole, 3-mm global VLBI network [scale: 0.05 pc] (f) supermassive black hole shadow, Event Horizon Telescope [scale: 0.005 pc] [1].

The most complete VLBI study of the inner M87 jet carried out so far was presented in [64]. Among its main results can be mentioned that a jet and counterjet were found in the inner 0.12 pc which are both edge-brightened. The presence of an helical magnetic field close to the core was suggested by polarization observations.

The inclination angle of the M87 jet with respect to our line of sight is a puzzling issue. It has been estimated between 10° and 20° based on optical observations of *HST*-1 [65, 62, 58]. However, [66] estimated it between 30° and 45 ° based on a measurement of proper motion and brightness ratio with VLBA at 43 GHz. This is consistent with [67] who calculated it to be between 29° and 45° based on the measured apparent motions in the jet and the counter jet with VLBI observations at 86 GHz. They claim that a viewing angle between 10° and 20° is not able to explain the fact that M87 is highly limb-brightened. However, they also explored the possibility that the viewing angle is variable throughout the jet. On the other hand, large viewing angles are disfavored by the detection of Very High Energy (VHE) emission from M87. According to [67] this could be explained by the very wide apparent opening angle of the jet base of M87 (up to 100°). Then, if the VHE emission zone were located on the outer zones of the jet base (closer to our line of sight) it could be highly beamed even if the viewing angle is

large.

The viewing angle of the jet can also be constrained using the so called "Doppler factor" of the jet. The Doppler factor is defined as:

$$\delta = \frac{\Gamma}{1 - \beta \cos(\theta)}. \tag{3.1}$$

Where δ is the Doppler factor (which can be constrained through SED modelling), Γ is the Lorentz factor of the jet, β is the ratio between the speed of the jet and the speed of light and θ is the viewing angle. According to [68]:

$$\sin\theta \leq \frac{1}{\delta}. \tag{3.2}$$

The jet power of M87 has been estimated between $10^{42} - 10^{45}$ erg s^{-1}. This is in agreement with the maximum jet power that can be extracted from M87* fed, which has been calculated in $\sim 10^{43} - 10^{44}$ erg s^{-1} [69, 70].

Regarding the gamma-ray emission of M87, it was the third radio galaxy detected by *Fermi* LAT [65] and the first one detected at VHE [71]. Other radio galaxies detected at VHE energies are Centaurus A, NGC 1275, 3C 264, IC 310 and PKS 0625-35 [4].

In 2009, it was reported that the GeV spectrum of M87 was of power law type ($dN/dE \propto E^{-\Gamma}$) with $\Gamma = 2.26 \pm 0.13$ using six months of all-sky survey data from *Fermi* LAT [65]. The LAT 8-year Source Catalog (4FGL) also reported a power law type spectrum with $\Gamma = 2.055 \pm 0.037$. Performing a more detailed analysis of the 100 MeV-300 GeV range in [6], a broken power law type spectrum was obtained with $\Gamma_1 = 2.16 \pm 0.16$ and $\Gamma_2 = 1.89 \pm 0.29$ with an energy break of $E_b = 28 \pm 11$ GeV. The last results were obtained for a *Fermi LAT* data set covering about 7.7 years from August 4, 2008 to April 12, 2016.

With regard to VHE emission ($E \gtrsim 1$ TeV), M87 has been detected by Imaging Atmospheric Cherenkov Telescopes (IACTs) like H.E.S.S [72], MAGIC [73] and VERITAS [74]. Flaring states have been observed at least three times in 2005, 2008 and 2010 [5].

3.2 Variability of M87

According to the multiwavelength campaign reported in [75], no variability was observed for the period of 2012-2015 in the whole electromagnetic spectrum (including TeV observations made with MAGIC). Multiwavelength lightcurves for this period can be seen in Figure 3.4 .This is coincident with the monitoring made with VERITAS [76].

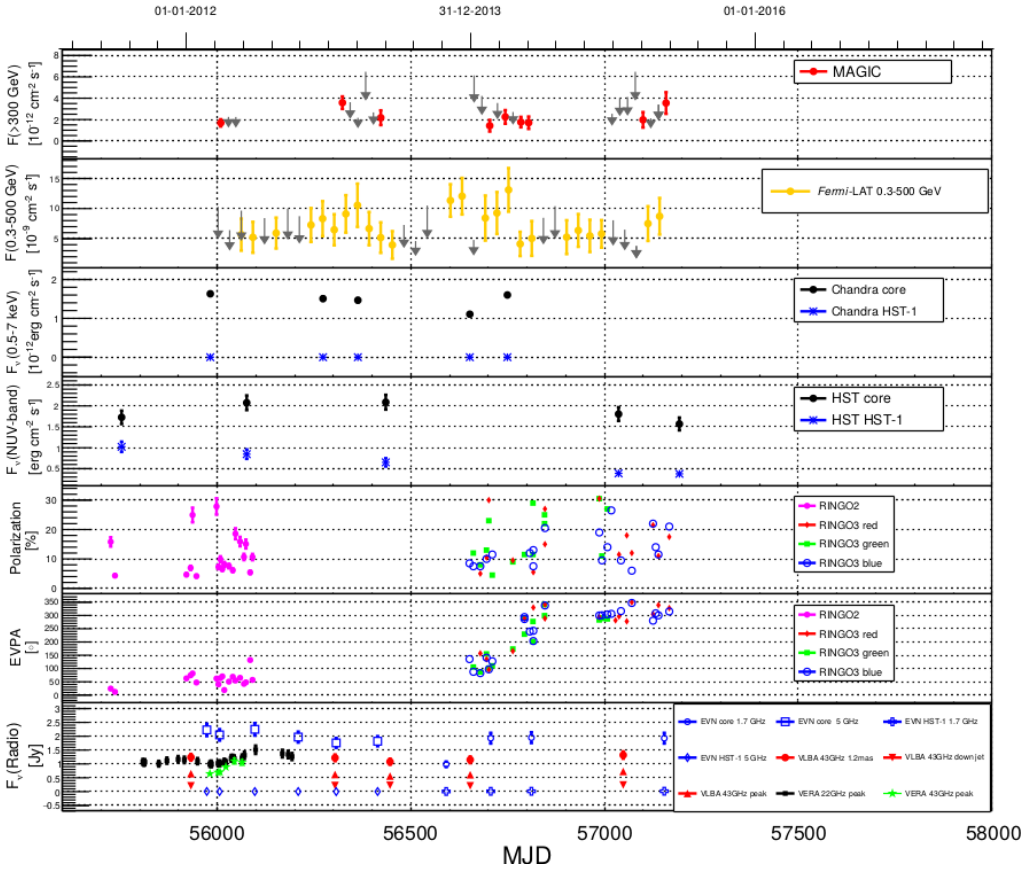

Figure 3.4: Multiwavelength lightcurves of the M87 core and the jet feature *HST-1* from 2012 to 2015 taken from [75]. From top to bottom: VHE gamma-ray observations from MAGIC, HE gamma-ray observations from *Fermi* LAT, *Chandra* X-ray observations from the core (dark points) and the jet feature HST-1 (blue asterisks), optical *HST* observations from the core (dark points) and the jet feature HST-1 (blue asterisks), optical polarization data by the Liverpool telescope with RINGO2 in 2012 and with RINGO3 in 2014-2015 (symbols are indicated in the image), radio observations taken with EVN (blue open symbols), VLBA (red filled symbols) and VERA (black empty and filled stars)

According to MOJAVE/2cm Survey Data Archive [77], there were four observations from 2014 to 2017 (coincident with the HAWC results reported in [78]). The core of M87 did not show variability in those observations.

In The *Fermi* Large Area Telescope Fourth Source Catalog (4FGL), the variability index was defined as the sum of $2\times \log$(Likelihood) difference between the flux fitted in each time interval and the average flux over the full catalog interval. The value of the variability index for M87 was 17.0 while the threshold which is considered likely variable is 18.48. Then, according to this index, M87 is likely to be a steady source [14].

H.E.S.S reported in 2005 a VHE flare in M87 [73]. During this event, no flaring activity was detected in the core at any available frequency band [5]. However, this flare was coincident in time with the peak of a long term flare in the first bright feature in the jet, *HST*-1 [5]. This flare started around 2002 and ended around 2008. It was detected in radio, optical and X-rays [63]. Because of this coincidence *HST*-1 has been discussed to be the origin of the gamma rays emission in M87 [79]. However, this possibility has been disfavored by the daily timescale variability in the VHE emission (which implies a emission zone smaller than the size of *HST*-1) and specially because of the absence of *HST*-1 flaring activity during the other two observed flares [5](which can be seen in *HST*-1 lightcurves shown in Figure 3.5).

A VHE flare in M87 was observed in 2008 by the IACTs H.E.S.S, VERITAS and MAGIC. This was coincident with high flux activity in the core observed at 43 GHz with the Very Long Baseline Array (VLBA) and in X-rays with *Chandra* [74] (see the activity during this flare in Figure 3.5).

Finally, the last VHE flare detected in M87 was in 2010 (see the VHE flares in Figure 3.5). It was observed by H.E.S.S, VERITAS and MAGIC. Unlike the previous flare, there were no detections of high activity in the core in radio and optical wavelengths. However, the X-ray observatory *Chandra* reported high activity in the core (~ 3 days after the peak of the VHE emission) [5].

In conclusion, variability studies favored the core of M87 as possible source of the VHE emission over other structures such as *HST*-1. Moreover, due to the lack of activity in other frequencies during some VHE flares (especially during the one of 2005) an emission model of M87 has to be able to explain orphan flares (which are those only detected in TeV gamma rays).

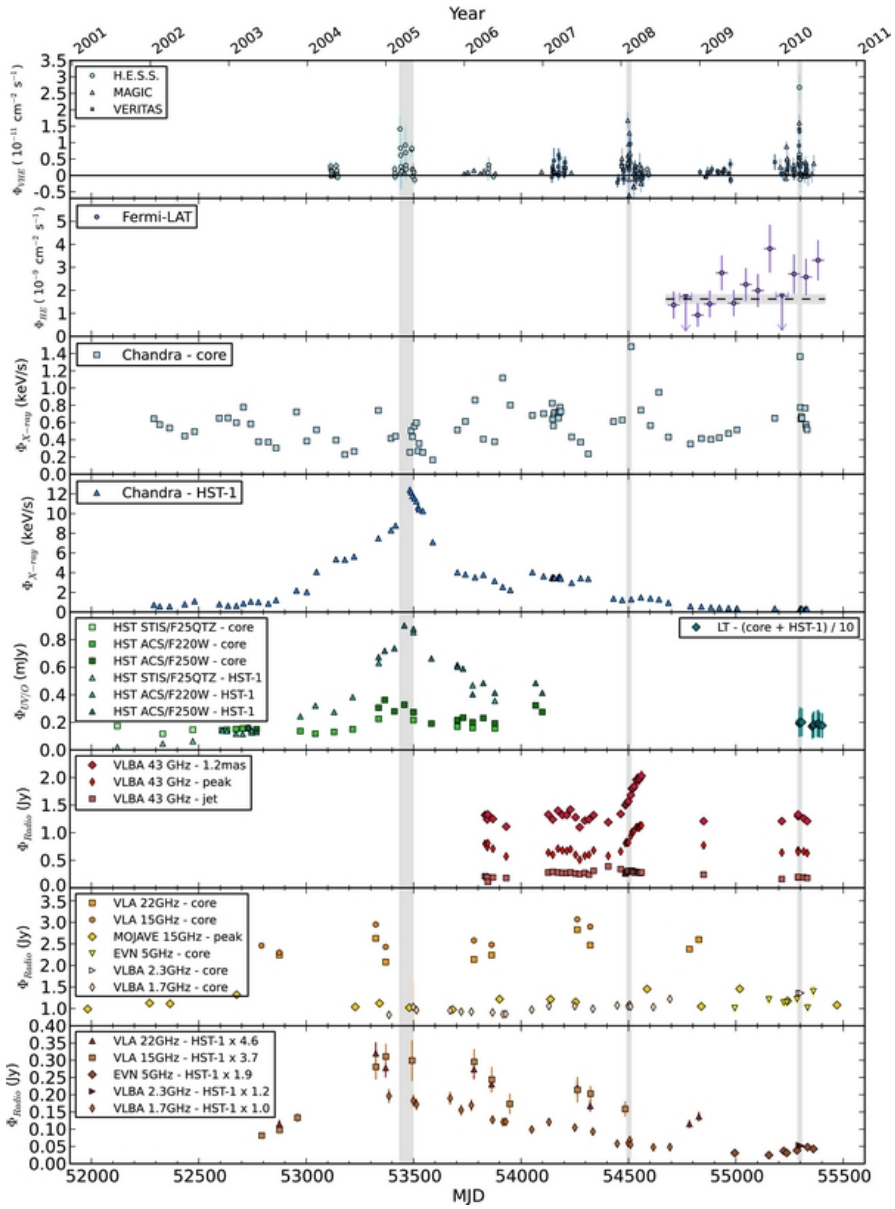

Figure 3.5: Multiwavelength lightcurves of the M87 core and the jet feature *HST-1* from 2001 to 2010, [5]. From top to bottom: - VHE gamma-ray observations made with H.E.S.S., MAGIC and VERITAS.-HE gamma-ray observations made by *Fermi* LAT.-*Chandra* observations from the M87 core.-*Chandra* observations of the jet feature *HST*-1. -*HST* observations of both the core and the jet feature *HST*-1. -VLBA observations at 43 GHz of the jet, the peak of the image (core) and 1.2 mas away from the core (*HST*-1). - Radio observations of the core. -Radio observations of *HST*-1. Gray bands correspond to the VHE flares reported for M87.

3.3 SED modeling of M87 to explain its VHE emission

The physical mechanism that produce the VHE emission in M87 remains unclear. Many alternatives have been proposed to model the broadband SED and the TeV zone.

Most authors consider that the core is the region where the VHE emission is originated. Some of them consider that one-zone SSC models could be enough to explain this emission [80, 75] (see Figure 3.6 for an example). However, some authors argue that this scenario is not able to explain VHE emission and especially VHE flares. Some of the proposed explanations are:

- Structured jet: in [81] the jet was modelled to be composed by a fast spine surrounded by a slower layer. Is this model the emission from radio to GeV is produced in the spine while the TeV emission is generated in the layer. The physical mechanisms involved in this model are electron synchrotron emission and inverse Compton scattering.
- Upstream Compton scattering: In [82] the jet was modelled to decelerate by a factor of ~ 4 over a length of ~ 0.1 pc. In this model the TeV emission is reproduced by upstream Compton (UC) scattering in which upstream faster flow electrons upscatter low energy photons of the downstream slower flow.
- Misaligned mini-jets: In this scenario proposed by [83] minijets near the main jet of M87 are thought to produce its TeV flares. According to the model if the minijets beamed their emission outside the jet cone it would result in rapidly evolving TeV flares.
- Multi-zone SSC models: In those models multiple SSC blobs are modeled to produce the broadband emission instead of one single zone. In [84] several plasma blobs are located in the large opening angle of the jet formation zone of M87.
- Dynamic processes in the supermassive black hole magnetosphere: In [85] TeV emission is produced by inverse Compton and curvature radiation in the supermassive black hole magnetosphere [20] by electron-positron pairs produced by MeV photons in the vicinity of the black hole.
- Hadronic processes: In [86] the second component of the broadband SED of M87 was modelled to be a combination of different hadronic processes including proton synchrotron, muon synchrotron, π^0 cascade and $\pi^{\pm}$ cascade emission.
- Lepto-hadronic processes: in those models the VHE emission is produced by the decaying of neutral pions π^0 that are product of interactions between accelerated protons and high energy photons [87, 88] (see figure 3.7 for an example). One of these models was assumed in this thesis (see Chapter 5 for details).

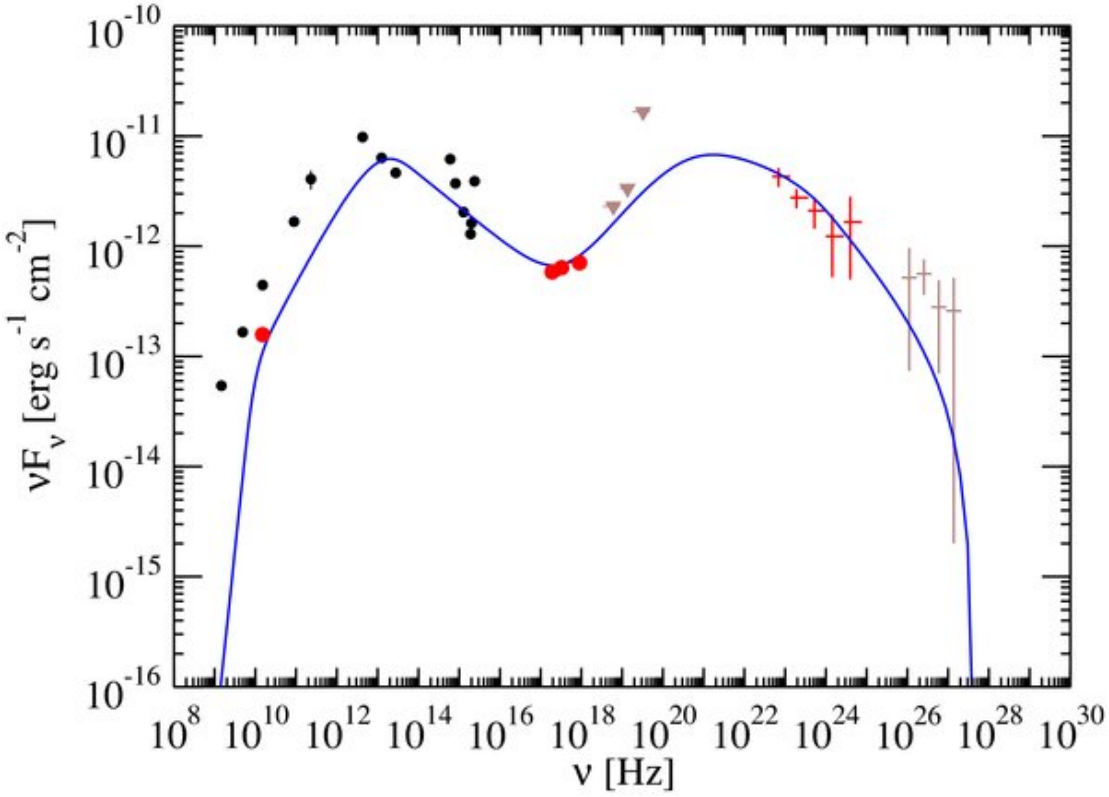

Figure 3.6: SED fitting of M87 using a one-zone SSC model including low activity state VHE observations taken from [65]. Red points correspond to observations contemporary to the *Fermi* LAT data (red crosses), black points correspond to historical data, triangles correspond to upper limits gray crosses to H.E.S.S. observations. The SSC model corresponds to the blue solid line. As can be seen in the image, TeV data does not seem to be well explained by this model.

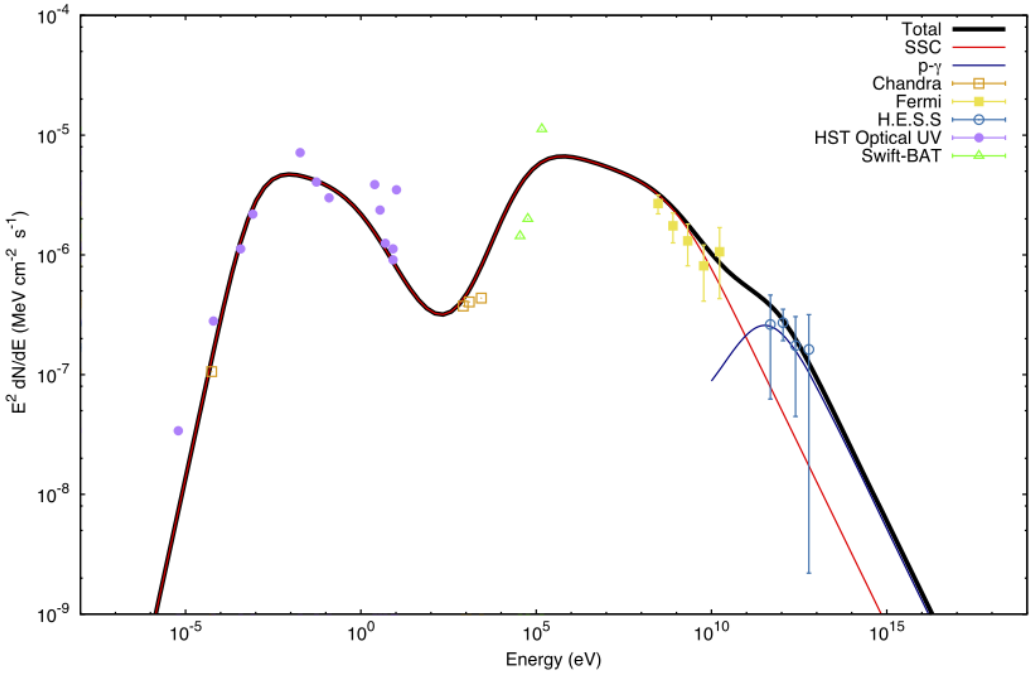

Figure 3.7: SED fitting of M87 using a one-zone SSC model and a photohadronic component to explain low activity state TeV observations taken from [88]. Data used in this fit is basically the same as in [65] whose results are shown in Figure 3.6. The red curve corresponds to the one-zone SSC model and the blue curve corresponds to the photohadronic component. The sum of both models is plotted in black.

Chapter 4

HAWC Gamma-Ray Observatory

4.1 General characteristics

The High Altitude Water Cherenkov (HAWC) is a gamma-ray and cosmic-ray observatory located in the state of Puebla, Mexico (97.3° W, 19.0° N) on the flanks of the Sierra Negra Volcano at an elevation of 4100 m above level sea. The site is close to the Pico de Orizaba, the highest mountain in Mexico and the third highest in North America (see Figure 4.1). Due to its position HAWC covers 8.4 sr every sidereal day, which correspond to 2/3 of the whole sky. The array can detect gamma rays in the 100 GeV to 100 TeV range.

The array comprises 300 water Cherenkov detectors (WCDs) covering an area of approximately 24 000 m^2. Each WCD is made of a 5 m high water tank with 7.32 m diameter containing a custom-made light-tight bladder. The array can store a total of 58 million liters of purified water. At the bottom of every WCD four photomultiplier tubes (PMTs) are mounted:

- One 10-inch Hamamatsu R7081 PMT at the center
- Three 8-inch Hamamatsu R5912 PMTs (previously used in the Milagro experiment) at 1.8 meters from the center making an equilateral triangle.

When gamma-ray photons and cosmic rays enter the atmosphere of Earth they produce cascades of particles or air showers. When these particles get to the WCDs they are absorbed by the purified water that filled them. Particles emit Cherenkov radiation which is produced when a particle travelling in a medium is faster than light

Figure 4.1: Picture of the HAWC site with the Pico de Orizaba at the bottom (image from `https://www.hawc-observatory.org/img/hawc_site_201611.jpg`)

in that medium [8]. This radiation is detected by the PMTs. Cherenkov radiation produced by air showers in the atmosphere is used by the IACTs to detect them. However, water is a more efficient medium than air for Cherenkov radiation since it has a higher refraction index.

The counting house is located at the center of the array. Signals detected in the PMTs are transmitted to it through RG-59 coaxial cables. The detector records air shower events at a rate of $\sim$ 25kHz. Most of them correspond to cosmic-ray induced air showers [90].

Not all events recorded by the instrument are included in the analysis. To optimize this process nine fraction hit bins have been defined (f_{hit} bins). Those bins are based on the shower size which is defined as the ratio of the number of PMTs hit during 20 ns of the shower front and the number of channels available at the time of the event. The definitions of the bins are given in Table 4.1.

Regarding the relation between hit bins and event energies, in Figure 4.3 shows the distributions of true photon energies in each bin from a simulated source. As can be seen, the bins are roughly correlated to the event energy, but there are significant overlaps in some of them [91].

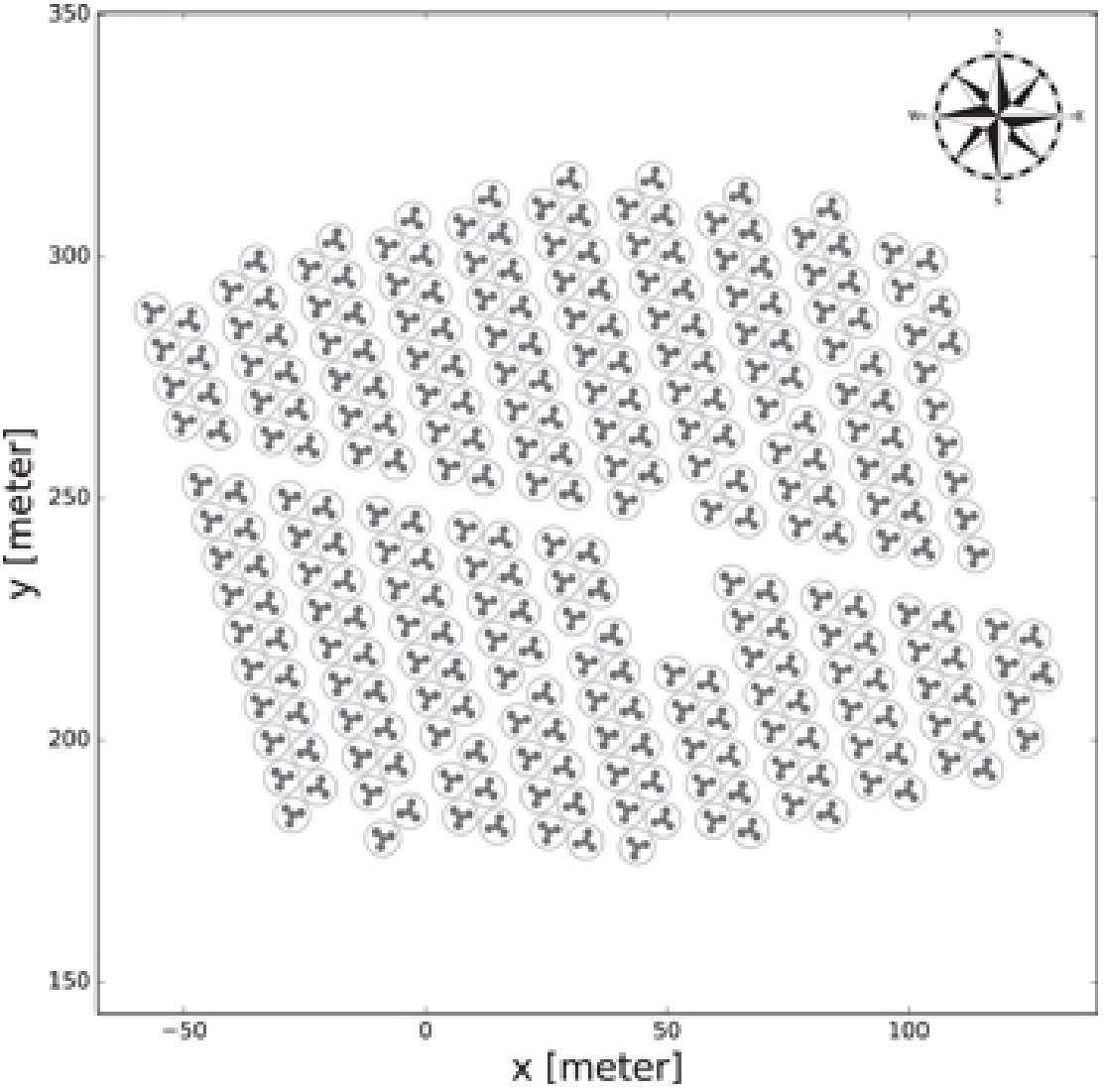

Figure 4.2: HAWC array scheme representing the location of the 300 WCDs or tanks. Open circles correspond to tanks and the small circles inside them indicate the position of the PMTs. The gap in the center corresponds to the location of the counting house [89]

Bin	f_{hit} (%)
1	6.7-10.5
2	10.5-16.2
3	16.2-24.7
4	24.7-35.6
5	35.6-48.5
6	48.5-61.8
7	61.8-74.0
8	74.0-84.0
9	84.0-100.0

Table 4.1: Definition of the fraction hit bins in terms of the shower size (number of PMTs hit during the event divided by the number of available channels).

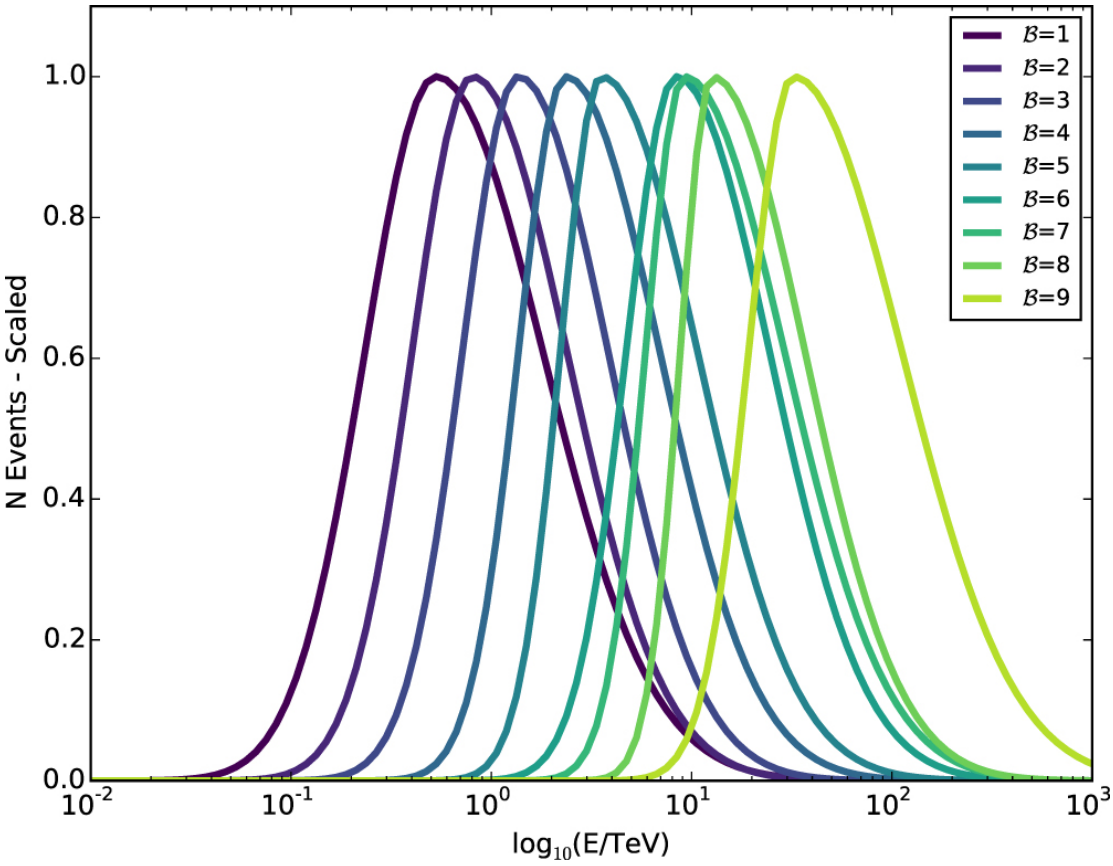

Figure 4.3: Distribution of true energies as a function of the hit bin ($\mathcal{B}$) for $\mathcal{B}$ between 1 and 9. The figure was generated using Monte Carlo simulations. A transiting source with energy spectrum of the form $E^{-2.63}$ and a declination of $+20°$N was assumed [91].

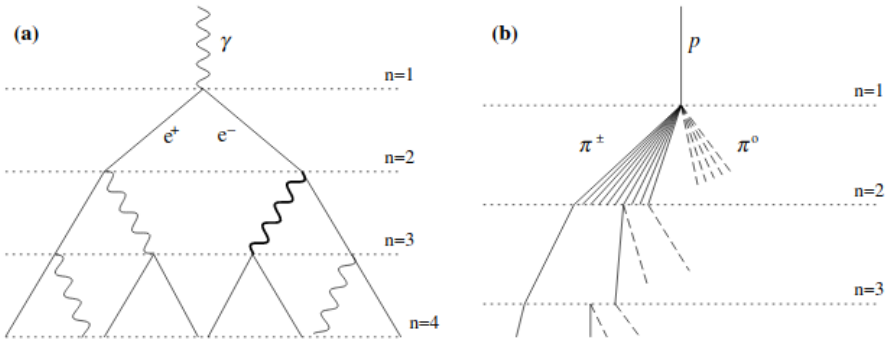

Figure 4.4: Schematic representation of electromagnetic showers (a) and hadronic showers (b) according to the Heitler model [92]. The number n corresponds to the n-th interaction after the particle gets to the atmosphere. γ represents gamma-ray photons, p is a cosmic ray, e^+ represents positrons, e^- represents electrons, $\pi^{\pm}$ are charged pions and π^0 are neutral pions. For simplicity, scales in this diagram are presented to be the same at each interaction.

4.2 Atmospheric particle cascades

According to the Heitler model [92] electromagnetic air showers start when gamma rays interact with atmospheric molecules and produce electron positron pairs. Then, after travelling some distance, those particles produce gamma rays by bremsstrahlung emission. The new gamma rays are also able to produce electron positron pairs starting the cycle again. The probability that a particle suffers an interaction after crossing a column density x is $P(x) = 1 - \exp(x/x_0)$ where x_0 is the mean free path for a high energy photon in the atmosphere $x_0 = 37\text{g/cm}^2$. As their individual energies decrease, leptons and photons tend to interact with competing processes, like Compton scattering and photo-ionization, and the cascade ceases to grow.

Cosmic rays also produce air showers when interact with atmospheric particles. Those air showers include production of neutral pions which decay in gamma rays that can produce electron-positron pairs. But there is also production of charged pions which decay in other particles such as muons. Muons have high transverse momenta making hadronic showers more extended than electromagnetic showers [92]. Figure 4.4 shows a schematic representation of the Heitler model predictions for both showers.

Because of their different compositions both kinds of air showers have different characteristics when detected by the array. Electromagnetic cascades present an uniformly decreasing energy distribution around the core and hadronic cascades are identified by isolated hits.

Two topological variables are used to separate hadronic and electromagnetic events:

1. Compactness: it is defined as the ratio between the number of PMTs hit within 20 ns of the shower front and the highest charge more than 40 meters from the shower core. Events with a higher compactness are more likely to be electromagnetic events.

2. Parameter for Identifying Nuclear Cosmic rays (PINCness): this parameter is basically a χ^2 fit and it is defined as:

$$P = \frac{1}{N}\sum_{i=0}^{N}\frac{(\log(q_i) - \langle\log(q_i)\rangle)^2}{\sigma^2}. \tag{4.1}$$

   Where N is the total number of hits, q_i is the charge in the i-nth PMT, and σ was determined by selecting a sample of high f_{hit} , extremely gamma-like events and fitting the distribution of measured charges for a variety of different predicted charge levels [93]. In this case events with a lower PINCness are more likely to be gamma-ray events.

As it was mention before, hadronic background is much higher than gamma-ray signal. Even when events are recorded at a rate of $\sim$ 25 kHz only 400 gamma-ray events per day are detected from the Crab Nebula, which is the brightest source detected by HAWC. In fact, $> 99\%$ of air showers can be rejected as gamma-ray events [91].

The energy estimation of the gamma-ray events can be done by different methods. The simplest estimator (which is used by most HAWC studies so far) is the size of the air shower event [91]. However, other more complicated methods have recently developed in order to improve HAWC sensitivity [90].

4.3 HAWC: Extragalactic results

Extragalactic TeV observations are limited by the Extragalactic background light (EBL). The EBL comprises all the radiation with wavelength between 0.1 and 1000 μm emitted by resolved and unresolved galaxies excluding the Cosmic Microwave Background (CMB). TeV radiation coming from extragalactic sources is attenuated by photon-photon interaction with EBL [94].

Due to the EBL opacity, only relatively nearby extragalactic sources can be detected by HAWC. According to the 2HWC catalog [89] with 507 days of observations only two sources detected out of the Galactic Plane have a known association, Markarian 421 (Mkn 421)and Markarian 501 (Mkn 501). Markarian 421 (J2000.0 R.A.$= 11^h04^m27.^s314$, Dec.$= +38°12'31.''80$; $z = 0.030$ [95]) is a BL Lac which was the first AGN detected at VHE [96]. Markarian 501 (J2000.0 R.A.$= 16^h53^m52.^s2$, Dec.$= +39°45'37.''0$; $z = 0.034$) is also a BL Lac.

A more detailed analysis using 1523 day of observations is reported by [97] in the $0.5 - 32$ TeV energy range. The sample consisted in 138 nearby ($z < 0.3$) AGNs from the Third *Fermi* LAT Catalog of High-Energy Sources (3FHL) [98]. A preliminary release of this study, using a smaller data set, was presented by [78]. Mkn 421 and Mkn 501 were clearly detected. Moreover, three other AGNs were detected with less significance: the BL Lac objects VER J0521+211 (J2000.0 R.A.$= 05^h21^m45^s$, Dec.$= +21°12'51.''4, z = 0.108$) and 1ES 1215+303 (J2000.0 R.A.$= 12^h17^m52^s$, Dec.$= +30°07'00.''6, z = 0.130$) as well as the radio galaxy M87. Upper limits were obtained for the rest of the sources. The analysis is based on the test statistic which is defined as:

$$TS = 2\ln\left\{\frac{\mathcal{L}(S+B)}{\mathcal{L}(B)}\right\}, \tag{4.2}$$

where $\mathcal{L}(S+B)$ is a source+background likelihood model and $\mathcal{L}(B)$ is a background likelihood model. The statistical significance is given by $s = \sqrt{TS}$. The analysis was performed optimizing the TS on each pixel. The model of the sources consists in a power law spectrum of the form:

$$\frac{\mathrm{d}N}{\mathrm{d}E} = K\left(\frac{E}{1\ \mathrm{TeV}}\right)^{-\alpha}, \tag{4.3}$$

where K is a normalization constant, E is the photon energy and α is the power law index. The observed spectra were corrected by the EBL model presented by [99]. The results obtained for the five detected AGNs are given in Table 4.2.

Object	K [TeV^{-1}s^{-1}cm^{-2}]	α	TS	f_E [erg s^{-1} cm^{-2}]
Mkn 421	$(33.0 \pm 0.6) \times 10^{-12}$	2.63 ± 0.02	4193	$(132 \pm 6) \times 10^{-12}$
Mkn 501	$(6.21 \pm 0.69) \times 10^{-12}$	2.31 ± 0.08	280.28	$(40 \pm 16) \times 10^{-12}$
M87	$(0.69 \pm 0.22) \times 10^{-12}$	2.63 ± 0.18	13.19	$(2.7 \pm 1.6) \times 10^{-12}$
VER J0521+211	$(2.39 \pm 0.89) \times 10^{-12}$	2.01 ± 0.38	10.34	$(3.8 \pm 1.4) \times 10^{-12}$
1ES 1215+303	$(3.78 \pm 1.36) \times 10^{-12}$	3.07 ± 0.37	12.80	$(6.1 \pm 2.1) \times 10^{-12}$

Table 4.2: AGN detections of the survey of Active Galaxies with HAWC reported by [97]. All the results are intrinsic (corrected by EBL). K corresponds to the spectrum normalization constant, α to the spectrum power law index and f_E the intrinsic VHE flux.

Chapter 5

Emission Model

M87 has been observed and monitored in the whole electromagnetic spectrum [5]. Its Very High Energy emission seems to be originated in the central region of the galaxy (i.e. the inner jet) and not in the extended lobes [72]. The broadband SED of BL Lac objects and FR-I radio galaxies is characterized by the presence of two components or peaks. The first component usually extends from radio to visible or X-rays. The second component covers the high energy emission. This non thermal emission is commonly explained by a Synchrotron Self-Compton (SSC) scenario [65, 80].

The first component is attributed to synchrotron radiation that is produced by electrons moving at relativistic velocities in a randomly oriented magnetic field. On the other hand, the second peak is explained by inverse Compton scattering of synchrotron photons to higher energies by the same electron population. However, some authors claim that SSC models are not able to explain VHE emission in M87. Evidence for a possible spectral turnover in the GeV regime $E \gtrsim 10$ GeV was found by [6]. This was interpreted as an additional physical component in the emission. One zone SSC models were found to have difficulties in explaining VHE/X-ray correlated variability in M87 [5], whereas [88] claimed that one zone SSC models can not be extended to VHE in FR-I radio galaxies. That is why different alternative ideas have been proposed such as seed photons coming from other regions in the jet [82] and photohadronic interactions [88].

A hybrid model has been used in this work. Low and high energy components are explained with a SSC scenario while photohadronic interactions explain the very high energy emission. Therefore, the broadband SED have been modeled with three components described in the next Sections.

5.1 Synchrotron Self Compton emission model

As it was mentioned before, according to the unification schemes FR-I radio galaxies correspond to the misaligned counterparts of BL Lacs. A SSC model for the broadband SED of BL Lacs is presented in [2]. This model considers a homogeneous spherical region or blob in the inner jet moving with a Lorentz factor Γ (blue region highlighted in the diagram of Figure 5.1). The Doppler factor δ is given by:

$$\delta = [\Gamma(1 - \beta\mu)]^{-1}, \tag{5.1}$$

where Γ is the Lorentz factor of the jet, β is the ratio of the speed of the jet and the speed of light and $\mu = \cos\theta$ where θ is the angle of the jet with the observer's line of sight (as can be seen in Figure 5.1).

The minimum variability timescale is:

$$t_{v,min} = \frac{(1+z)R'_b}{c\delta}. \tag{5.2}$$

Where R'_b corresponds to the comoving radius of the region, c to the speed of light, δ to the Doppler factor and z to the redshift of the source. Comoving quantities are primed following the convention used in [2].

The electron population of the region, which follows a energy distribution $N'(\gamma')$, is moving in a randomly oriented magnetic field producing synchrotron radiation (see the electron in the magnetic field line of Figure 5.1 and the emitted synchrotron photon). The emitted synchrotron flux at a frequency ν is given by:

$$f^{syn}(\nu) = \frac{\sqrt{3}\delta^3(1+z)\nu e^3 B}{4\pi d_L^2 m_e c^2} \int_1^\infty d\gamma' N'_e(\gamma') R(x). \tag{5.3}$$

Where e is the electron charge, z is the redshift of the source, d_L is the luminosity distance to the source, B is the mean intensity of the randomly oriented magnetic field, m_e is the electron mass, γ is the Lorentz factor of the accelerated electrons, c the speed of light in vacuum and ν the frequency of the emitted photons. $R(x)$ is a function that comes from making the electron motion arbitrary. $R(x)$ is given by:

$$R(x) = \frac{x}{2} \int_0^\pi d\theta \sin(\theta) \int_{x/\sin(\theta)}^\infty dt K_{5/3}(t), \tag{5.4}$$

with

$$x = \frac{4\pi\nu(1+z)m_e c}{3eB\gamma'^2}, \tag{5.5}$$

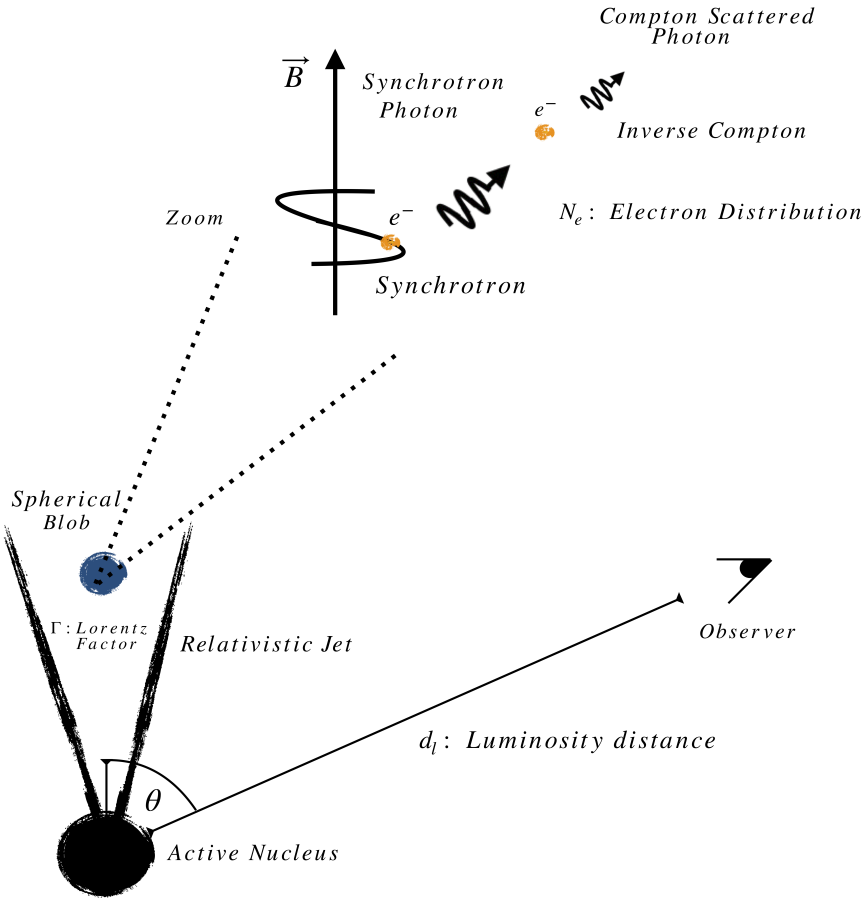

Figure 5.1: One-zone SSC model diagram. The electron population which produces the emission is confined in the spherical blob located in the inner jet. Electrons are being accelerated by the magnetic field producing synchrothron emission. Some synchrotron photons are also Compton upscattered by accelerated electrons. The emission zone is viewed with an angle θ respect to the observer's line of sight.

where $K_{5/3}$ is the modified Bessel function of the second kind of order $5/3$. According to [2] $R(x)$ can be approximated to:

$$\log(R) = A_0 + A_1 y + A_2 y^2 + A_3 y^3 + A_4 y^4 + A_5 y^5, \tag{5.6}$$

where $y = \log_{10}(x)$ and the coefficients are given in Table 5.1:

Coefficient	$10^{-2} < x < 10^{0}$	$10^{0} < x < 10^{1}$
A_0	-0.358	-0.358
A_1	-0.837	-0.797
A_2	-1.145	-1.611
A_3	-0.681	0.261
A_4	-0.228	-1.698
A_5	-0.032	0.033

Table 5.1: Coefficients for the approximated form of $R(x)$

These expressions are accurate to ~ 1 % in the range $0.01 < x < 10$. The asymptotic cases are given by:

$$R(x) = \begin{cases} 1.80842x^{1/3}, & x \ll 1 \\ \frac{\pi}{2}e^{-x}\left(1 - \frac{99}{162x}\right), & x \gg 1 \end{cases}, \tag{5.7}$$

which are accurate to better than 5 %.

The electron energy distribution for this model was assumed to be a broken power law given by Equation 5.8.

$$N_e(\gamma') = K_e \begin{cases} 0 \text{ for } \gamma' < \gamma'_1 \\ \left(\frac{\gamma'}{\gamma'_{break}}\right)^{-p_1} \text{ for } \gamma'_1 < \gamma' < \gamma'_{break} \\ \left(\frac{\gamma'}{\gamma'_{break}}\right)^{-p_2} \text{ for } \gamma'_{break} < \gamma' < \gamma'_2 \\ 0 \text{ for } \gamma'_2 < \gamma' \end{cases}. \tag{5.8}$$

As it was mentioned before, the second component is produced by inverse Compton scattering of low energy photons to higher energies by the electron population of the jet (see the interaction between a synchrotron photon and an electron in Figure 5.1 and the subsequent emission of an inverse Compton photon). The expression for the second component flux at a frequency ν_s is given by Equation 5.9.

$$f^{ICS}(\nu_s) = \frac{9(1+z)^2\sigma_T\nu_s^2}{16\pi\delta^2c^2t_{v,min}^2}\int_0^\infty d\nu \frac{f^{syn}(\nu)}{\nu^3}\int_{\gamma'_{min}}^{\gamma'_{max}} d\gamma' \frac{N'_e(\gamma')}{\gamma'^2}F_c(q,\Gamma_e). \tag{5.9}$$

Where σ_T is the Thomson cross section, ϵ_s the emitted photons energy and $F_c(q, \Gamma_e)$ is the Compton Scattering kernel for isotropic photon and electron distributions, which describes how a photon is redistributed after interacting with an electron [100]. $F_c(q, \Gamma_e)$ is given by [2]:

$$F_c(q,\Gamma_e) = \left[2q\ln q + (1+2q)(1-q) + \frac{1}{2}\frac{(\Gamma_e q)^2}{(1+\Gamma_e q)}(1-q)\right] H\left(q; \frac{1}{4\gamma'^2}, 1\right), \quad (5.10)$$

where

$$q \equiv \frac{\epsilon'_s/\gamma'}{\Gamma_e(1-\epsilon'_s/\gamma')} \quad , \quad \Gamma_e = 4\epsilon'\gamma'. \quad (5.11)$$

And ϵ' and ϵ'_s are the synchrotron and inverse Compton comoving energies of the emitted photons in units of $m_e c^2$, which are a given by 5.12:

$$\epsilon' = \frac{h\nu(1+z)}{m_e c^2} \quad , \quad \epsilon'_s = \frac{h\nu_s(1+z)}{m_e c^2}. \quad (5.12)$$

The limits on q are: $\frac{1}{4\gamma'^2} \leq q \leq 1$

Which imply the limits: $\gamma'_{min} = \frac{1}{2}\epsilon'_s\left(1+\sqrt{1+\frac{1}{\epsilon'\epsilon'_s}}\right)$, $\gamma'_{max} = \frac{\epsilon'\epsilon'_s}{\epsilon'-\epsilon'_s}H(\epsilon'-\epsilon'_s) + \gamma'_2 H(\epsilon'_s-\epsilon')$.

5.2 Photohadronic model

As it was mentioned before, one-zone SSC models have difficulties to explain VHE emission and variability in M87. One alternative is the introduction of hybrid models where the two first components of the broadband SED are modeled with a SSC scenario and the VHE emission is explained by photohadronic interactions. The model presented here is based on the one used by [101] to model VHE emission in blazars.

A Fermi accelerated proton population is assumed to be contained in a spherical volume of radius R'_f (blue region in the jet of Figure 5.2) inside the blob of radius R' (SSC blob) [3]. These particles have a power law energy distribution [101, 88]:

$$\frac{\mathrm{d}N_p}{\mathrm{d}E_p} \propto E_p^{-\alpha}, \quad (5.13)$$

where the spectral index is $\alpha > 2$.

Due to the higher photon density in this inner volume, protons interact with the background photons through the following mechanism (in this case background photons correspond to those produced by inverse Compton scattering, see Figure 5.2 for a

schematic explanation) [3, 88]:

$$p + \gamma \rightarrow \Delta^{+} \rightarrow \begin{cases} p\,\pi^0 \text{ fraction 2/3} \\ n\,\pi^+ \text{ fraction 1/3} \end{cases} . \tag{5.14}$$

After that neutral pion decays in two gamma ray photons $\pi^0 \rightarrow \gamma\gamma$.

This process requires the center of mass energy of the interaction to exceed the Δ-mass [3, 88].

$$E'_p \epsilon'_\gamma = \frac{(m_\Delta^2 - m_p^2)}{2(1 - \beta_p \cos\theta)} \cong 0.32\mathrm{GeV}^2. \tag{5.15}$$

Where E_p is the energy of the proton and ϵ_γ is the energy of the target photon. Considering collisions with SSC photons from all directions, $\beta_p \approx 1$ and viewing from the observer frame:

$$\epsilon_\Gamma \epsilon_\gamma \cong 0.32 \frac{\delta^2}{(1+z)^2} \mathrm{GeV}^2. \tag{5.16}$$

Where ϵ_Γ is the energy of the emitted photon. According to [101] the π^0 decay photon flux is given by:

$$f^{p\gamma}(\epsilon_\Gamma) = A_\gamma f^{ICS}(\nu_\gamma) \left(\frac{\epsilon_\Gamma}{\mathrm{TeV}}\right)^{-\alpha+3}, \tag{5.17}$$

where ν_γ is the frequency of a photon with energy ϵ_γ and $f^{ICS}(\nu_\gamma)$ is the flux at ν_γ which is given by Equation 5.9. Thus, the total emitted flux at VHE energies is given by the sum of the inverse Compton flux and phtohadronic flux:

$$f^{VHE}(\nu_\Gamma) = f^{ICS}(\nu_\Gamma) + f^{p\gamma}(\epsilon_\Gamma(\nu_\Gamma)), \tag{5.18}$$

where is ν_Γ is the frequency of the emitted photon and ϵ_Γ the energy of the emitted photon ($\epsilon_\Gamma = h\nu_\Gamma$ where h is the Planck constant).

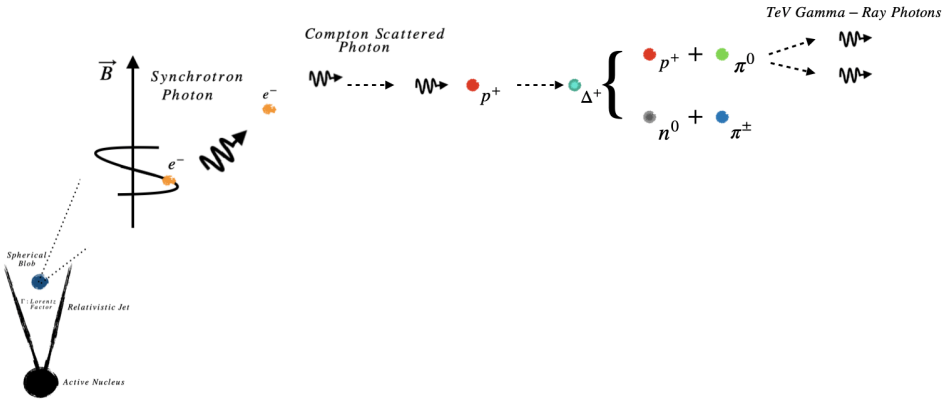

Figure 5.2: Photohadronic model diagram. This diagram is an extension of the diagram in Figure 5.1. Inverse Compton photons interact with a accelerated protons p^+ (red circles) and produce Delta baryons Δ^+ (cyan circles). Δ^+ decay in either a proton and a neutral pion (green circle), $2/3$ of the cases, or in a neutron n^0 (gray circle) and a charged pion (blue circle), in $1/3$ of the cases. Neutral pions decay into gamma ray photons which give rise to the VHE emission.

Chapter 6

Data and Methodology

6.1 Data

The broadband SED of the M87 core presented in this thesis was constructed using historical data partially based on those collected by the *Fermi* Collaboration [65] [1] . All of them described in this Section. Data cover almost all the important spectral regions used in astronomy.

6.1.1 Radio wavelengths

Radio and X ray observations of the nucleus and jet of M87 were reported in [102] . The radio observations were taken using the Very Large Array (VLA) in three frequency bands centered in 1.466 GHz, 4.885 GHz and 14.96 GHz. The observation epochs were 1985 March 1 for the lowest frequency and 1985 March 2 for the other two. The integration times were 10, 5 and 5 hours respectively. Flux density measurements were obtained for contiguous boxes along the jet on maps convolved to 1.2" FWHM angular resolution. Authors of the study that reports these results favor synchrotron emission as source of the radio spectrum.

The measurements corresponding to the core of the radio galaxy were used for fitting the SED. The corresponding results are presented in Table 6.1.

VLBA observations from the MOJAVE project [77] made on January 7 2009 reported an observed flux of $1.575 \pm 0.079 \times 10^{-13}$ erg s^{-1} cm^{-2} at 15 GHz for the core

[1] `https://www-glast.stanford.edu/pub_data/282/M87LAT/`

Frequency (MHz)	Flux ($\times 10^{-13}$ erg s^{-1} cm^{-2})	Observation Date
1466	0.539 ± 0.021	1985/3/1
4885	1.661 ± 0.044	1985/3/1
14960	4.42 ± 0.15	1985/3/2

Table 6.1: Core fluxes of M87 reported by [102]

.

of M87 [65] [2] . The angular resolution of these observations was about $0.001''$.

6.1.2 Millimeter wavelengths

Observations of M87 made with the IRAM Plateau de Bure interferometer at 87 GHz were presented in [103]. The image has a resolution of $2.9'' \times 1.8''$. Observations were made with three antennas between November 1992 and January 1993. A flux of 1.88 $\pm$ 0.1 Jy was reported for the core of M87.

In addition observations made with the Submillimiter Array (SMA) at 230 GHz presented in [104] reported a flux of 1770 $\pm$ 350 mJy for the core of M87 with a primary beam of $\sim 55''$ and a final synthesized beam of $1.2'' \times 0.8''$. These observations were made during the night of 2006 February 10 in the extended configuration with seven antennas in the array.

6.1.3 Infrared

Far infrared images from the *Spitzer Space Telescope* were obtained between 3.6 and 160 μm [105]. The authors indicate that there is an excess due to thermal emission produced by warm dust. After subtracting the thermal component the fluxes corresponding to the core of M87 were estimated in 50.7 mJy at 24 μm and 228 mJy at 70 μm. The images were convolved to the same resolution ($\sim 1.6''$) at 24 μm .

Mid infrared images from the Gemini 8 m telescope with OSCIR are reported in [60]. They constitute 7 hrs of observing time distributed between 2001 May 3 and 10 at 10.8 μ m. The reported flux for the core of M87 is 16.7$\pm$ 0.9 mJy. The angular resolution was $0.46''$. According to the authors, the nuclear emission is consistent with synchrotron emission with no evidence of a thermal component.

[2] `https://www-glast.stanford.edu/pub_data/282/M87LAT/mojave_2009jan7.dat`

6.1.4 Optical and UV

Observations of M87 from the *Hubble Space Telescope* (*HST*) made with FOC (The European Space Agency Faint Object Camera) are presented in [106]. They correspond to 29 exposures that were made during 1991. The fluxes corresponding to each filter are presented in Table 6.2. The image resolution of the images was about $\sim 0.15''$.

Band	Wavelength (μm)	Flux ($\times 10^{-13}$ erg s^{-1} cm^{-2})	Observation Dates
F120M	125.5	3.89 ± 0.78	during 1991
F140W	150.7	1.62 ± 0.32	during 1991
F152M	158.5	1.29 ± 0.26	during 1991
F220W	231.2	2.04 ± 0.41	during 1991
F372M	370.8	3.72 ± 0.74	during 1991
F501N	501.7	6.17 ± 1.23	during 1991

Table 6.2: Core fluxes of M87 reported by [106]

6.1.5 X rays

M87 has been observed with the High-Energy Transmission Grating Spectrometer in the *Chandra* X-ray telescope [107]. Data were taken on 2000 May 17 and 18 with an exposure time of 38.048 ks. The obtained flux density for the core was 5.88$\pm$ 2.40 $\times$ 10^{-13}erg s^{-1} cm^{-2} at 1 keV with a spatial resolution of $0.5''$.

Additional observations with *Chandra* were made between 2008 November and 2009 May [65]. Fluxes obtained after analyzing five resulting images (exposure time of 5 ks) are reported in Table 6.3.

Observations made with the X-ray telescope *NuSTAR* on 2017 February 15, April 11, and April 14 for 50, 24, and 22 ks, respectively were reported in [108]. The reported flux of the core was $4.8^{+0.9}_{-1.0}$ 10^{-13}erg s^{-1} cm^{-2} in the 20-40 keV band.

Upper limits for three *Swift*/BAT X-ray bands were also obtained in [65] which included four years of data from 2005 March to 2009 January. The results are shown in Table 6.3.

Band	Flux	Observation Dates	Observations made with
[keV]	[erg s^{-1} cm^{-2}]		
0-5-1.2	$(5.88 \pm 2.40) \times 10^{-13}$	between 2000/5/17 and /5/18	*Chandra*
0.5-1.2	$(5.84 \pm 0.29) \times 10^{-13}$	between 2008/11 and 2009/5	*Chandra*
1.2-2.0	$(6.38 \pm 0.31) \times 10^{-13}$	between 2008/11 and 2009/5	*Chandra*
2.0-7.0	$(7.07 \pm 0.39) \times 10^{-13}$	between 2008/11 and 2009/5	*Chandra*
20-40	$(4.8 \pm 1.0) \times 10^{-13}$	between 2017/2/15 and 4/14	*NuSTAR*
14-35	$< 2.30 \times 10^{-12}$	between 2008/3 and 2009/1	*Swift*/BAT
35-75	$< 3.34 \times 10^{-12}$	between 2008/3 and 2009/1	*Swift*/BAT
75-195	$< 1.66 \times 10^{-11}$	between 2008/3 and 2009/1	*Swift*/BAT

Table 6.3: Fluxes for the core of M87 in X-ray bands reported by [107],[65] and [108]

.

6.1.6 Gamma rays

The fourth *Fermi* Large Area Telescope catalog (4FGL) is based on the first eight years of data the *Fermi* Gamma-ray Space Telescope [14][3] . This catalog covers an energy range from 50 MeV to 1 TeV which is split in six bands. Results for M87 are shown in Table 6.4:

Energy band	Flux	Upper error	Lower error
[GeV]		[$\times 10^{-12}$ erg s^{-1} cm^{-2}]	
0.05-0.1	6.4	2.9	2.1
0.1-0.3	1.84	0.88	0.92
0.3-1	2.72	0.35	0.35
1-3	2.63	0.27	0.27
3-10	2.48	0.40	0.42
10-30	1.16	4.0	4.6
30-300	1.8	2.6	3.1

Table 6.4: Flux of M87 for the energy bands of the 4FGL catalog [14] made with data taken between 2008 and 2016

.

The first detection of M87 by the High Energy Stereoscopic System (HESS) gamma-ray observatory is reported in [72][4] . The energy range of these observations is from

[3] https://fermi.gsfc.nasa.gov/ssc/data/access/lat/8yr_catalog/

[4] https://www.mpi-hd.mpg.de/hfm/HESS/pages/publications/auxiliary/M87_

400 GeV to 10 TeV, which include 89 hours of data taken between 2003 and 2006. Data from 2005 show a higher energy state than the ones from 2004. Energy bands and fluxes corresponding to data from 2004 and 2005 are shown in Tables 6.5 and 6.6, respectively.

Energy band	Flux	Error
[TeV]	[TeV^{-1} s^{-1} cm^{-2}]	
0.300-0.695	1.55 $\times 10^{-12}$	1.33 $\times 10^{-12}$
0.695-1.609	3.13 $\times 10^{-13}$	1.11$\times 10^{-13}$
1.609-3.728	2.92$\times 10^{-14}$	2.19$\times 10^{-14}$
3.728-8.635	5.03$\times 10^{-15}$	4.99$\times 10^{-15}$

Table 6.5: Flux of M87 for the energy bands of the HESS observations in 2004 [72] between February 17 and May 23

Energy band	Flux	Error
[TeV]	[TeV^{-1} s^{-1} cm^{-2}]	
0.359-0.551	5.86$\times 10^{-12}$	2.90$\times 10^{-12}$
0.551-0.843	3.07$\times 10^{-12}$	0.72$\times 10^{-12}$
0.843-1.292	1.28$\times 10^{-12}$	0.26$\times 10^{-12}$
1.292-1.979	2.71$\times 10^{-13}$	1.05$\times 10^{-13}$
1.979-3.032	1.85$\times 10^{-13}$	0.50$\times 10^{-13}$
3.032-4.644	8.33$\times 10^{-14}$	2.37$\times 10^{-14}$
4.644-7.114	1.21$\times 10^{-14}$	0.98$\times 10^{-14}$
7.114-10.897	1.39$\times 10^{-14}$	0.54$\times 10^{-14}$

Table 6.6: Flux of M87 for the energy bands of the HESS observations in 2005 [72] between February 12 and May 15.

M87 observations corresponding to 150 h of exposure time with the MAGIC-I Cherenkov Telescope were reported in [109]. They were made in five different epochs between 2005/March and 2007/May and they were not coincident with VHE flares. The resulting spectrum was a power law $dN/dE = f_0(E/300\text{GeV})^{-\Gamma}$ with normalization constant $f_0 = 7.7 \pm 1.3 \times 10^{-12}$ TeV^{-1} cm^{-2} s^{-1} and $\Gamma = 2.21 \pm 0.21$ in the 0.1-2 TeV energy range. The differential flux corresponding to each energy band in presented in Table 6.7.

HAWC observations of M87 in the $0.5-32$ TeV, using data taken between November 26, 2014, and June 3, 2019, were reported by [97]. The resulting intrinsic flux was

`auxinfo.html`

Energy band	Flux	Error
[TeV]	[$\times 10^{-12}$ TeV^{-1} s^{-1} cm^{-2}]	
0.100-0.158	76.6	44.2
0.158-0.250	15.2	6.08
0.250-0.395	3.63	0.728
0.395-0.625	0.681	0.268
0.988-1.56	0.299	0.106

Table 6.7: Flux of M87 for the energy bands of the MAGIC-I observations between 2005/March and 2007/May [109].

$f_E = (2.7 \pm 1.6)$ adn the resulting spectrum was a power law $dN/dE = f_0(E/1 \text{ TeV})^{-\Gamma}$ with normalization constant $f_0 = (0.69 \pm 0.22) \times 10^{-12}$ TeV^{-1} cm^{-2} s^{-1} and $\Gamma = 2.63 \pm 0.18$ with a significance $\sqrt{TS} = 3.63$. See Section 4.3 for more details.

6.1.7 All data

The program developed for carrying out this work accepts as input observed frequencies in Hertz (Hz) and observed fluxes in cgs units (erg s^{-1} cm^{-2}). All data in those units are reported in Table 6.8.

Table 6.8: All data in cgs units as they were introduced in the fitting code.
The data point numbers are used to identify each data point in Tables and Figures of the following sections. In the case of *Fermi* LAT results, an average value of the error is used

Data point #	Frequency [Hz]	Flux [erg s^{-1} cm^{-2}]	Flux error
Radio			
I	1.47×10^{9}	5.39×10^{-14}	2.05×10^{-15}
II	4.89×10^{9}	1.66×10^{-13}	4.04×10^{-15}
III	1.50×10^{10}	4.43×10^{-13}	1.50×10^{-14}
IV	1.50×10^{10}	1.57×10^{-13}	7.88×10^{-15}
mm			
V	8.90×10^{10}	1.67×10^{-12}	8.90×10^{-14}
VI	2.30×10^{11}	4.07×10^{-12}	8.05×10^{-13}
IR			
VII	4.27×10^{12}	9.73×10^{-12}	4.27×10^{-14}
VIII	1.25×10^{13}	6.34×10^{-12}	1.25×10^{-13}

Table 6.8 – Continued from previous page

Data point #	Frequency [Hz]	Flux erg s^{-1} cm^{-2}	Flux error
IX	2.78×10^{13}	4.64×10^{-12}	2.50×10^{-13}
Visible and UV			
X	6.03×10^{14}	6.17×10^{-12}	1.23×10^{-12}
XI	8.13×10^{14}	3.71×10^{-12}	7.41×10^{-13}
XII	1.29×10^{15}	2.04×10^{-12}	4.07×10^{-13}
XIII	1.91×10^{15}	1.29×10^{-12}	2.57×10^{-13}
XIV	2.00×10^{15}	1.62×10^{-12}	3.24×10^{-13}
XV	2.40×10^{15}	3.89×10^{-12}	7.76×10^{-13}
X-rays			
XVI	2.42×10^{17}	5.92×10^{-13}	2.42×10^{-14}
XVII	1.91×10^{17}	5.84×10^{-13}	2.87×10^{-14}
XVIII	3.27×10^{17}	6.38×10^{-13}	3.10×10^{-14}
XIX	9.02×10^{17}	7.07×10^{-13}	3.88×10^{-14}
XX	7.25×10^{18}	4.80×10^{-13}	1.00×10^{-13}
XXI	6.09×10^{18}	$\leq2.30\times10^{-12}$	UL
XXII	1.35×10^{19}	$\leq3.34\times10^{-12}$	UL
XXIII	3.27×10^{19}	$\leq1.66\times10^{-11}$	UL
Gamma rays	(*Fermi* LAT)		
XXIV	1.81×10^{22}	6.41×10^{-12}	2.49×10^{-12}
XXV	4.84×10^{22}	1.84×10^{-12}	8.99×10^{-13}
XXVI	1.57×10^{23}	2.72×10^{-12}	3.49×10^{-13}
XXVII	4.84×10^{23}	2.63×10^{-12}	2.72×10^{-13}
XXVIII	1.57×10^{24}	2.48×10^{-12}	4.10×10^{-13}
XXIX	4.84×10^{24}	1.16×10^{-12}	4.31×10^{-13}
TeV gamma rays	(H.E.S.S. 2004)		
XXX	1.11×10^{26}	5.18×10^{-13}	4.44×10^{-13}
XXXI	2.56×10^{26}	5.61×10^{-13}	2.00×10^{-13}
XXXII	5.93×10^{26}	2.80×10^{-13}	2.10×10^{-13}
XXXIII	1.37×10^{27}	2.59×10^{-13}	2.57×10^{-13}
TeV gamma rays	(H.E.S.S. 2005)		
XXXIV	1.10×10^{26}	1.94×10^{-12}	9.61×10^{-13}
XXXV	1.68×10^{26}	2.39×10^{-12}	5.61×10^{-13}
XXXVI	2.58×10^{26}	2.34×10^{-12}	4.83×10^{-13}

Table 6.8 – Continued from previous page

Data point #	Frequency [Hz]	Flux erg s^{-1} cm^{-2}	Flux error
XXXVII	3.95×10^{26}	1.16×10^{-12}	4.49×10^{-13}
XXXVIII	6.06×10^{26}	1.86×10^{-12}	5.00×10^{-13}
XXXIX	9.28×10^{26}	1.97×10^{-12}	5.59×10^{-13}
XL	1.42×10^{27}	6.71×10^{-13}	5.43×10^{-13}
XLI	2.18×10^{27}	1.81×10^{-12}	6.97×10^{-13}
TeV gamma rays	(MAGIC)		
XLII	4.94×10^{25}	1.02×10^{-12}	4.06×10^{-13}
XLIII	7.80×10^{25}	8.54×10^{-13}	3.27×10^{-13}
XLIV	1.23×10^{26}	1.51×10^{-12}	3.03×10^{-13}
XLV	1.95×10^{26}	7.09×10^{-13}	2.79×10^{-13}
XLVI	3.08×10^{26}	7.78×10^{-13}	2.76×10^{-13}
TeV gamma rays	(HAWC)		
XLVII	$1.2\times10^{26}-7.7\times10^{27}$	2.7×10^{-12}	1.6×10^{-12}

6.2 Methodology

A code for simulating the broadband emission from a blazar or radio galaxy was developed using the programming language *Python*. This code reproduces the lepto-hadronic model presented in Chapter 5. The broadband SED was fitted by this emission model. The best fit values for the physical parameters were obtained. Errors were estimated using Monte Carlo simulations.

6.2.1 Fitting Technique: SSC component

As it was mentioned in Chapter 5, the first SED component (from radio to X-rays) was modeled as synchrotron emission (Equation 5.3) and the second component (from X-rays to GeV gamma rays) as inverse Compton emission (Equation 5.9). According to [2] the model shows low dependence on the minimum and maximum electron Lorentz factors (γ'_1 and γ'_2 respectively). That is why they were fixed to the values given by [65] $\gamma'_1 = 1$ and $\gamma'_2 = 10^7$. Following [65] the normalization constant K_e in Equation 5.8 was fixed to $K_e = 10^{46}$. The minimum variability timescale was assumed to be $t_{v,min} = 1.2 \times 10^5$ s,$= 1.4$ days, which by Equation 5.2 corresponds to the emission

zone radius of $R'_b = 1.4 \times 10^{16}$ cm $= 4.5$ mpc chosen by [65] for being consistent with the highest resolution of VLBA observations and the few day timescale TeV variability. Therefore, five fitting parameters were used in the SSC model (see Table 6.9)

Parameter	Symbol	Initial value
Magnetic Field	B	0.055 G
Doppler factor	δ	3.9
Electron distribution parameters		
Power law index (low energy)	p_1	1.6
Power law index (high energy)	p_2	3.6
Cutoff Lorentz factor	γ'_c	4000

Table 6.9: Fitting parameters for the SSC component with their initial values corresponding to best fit values obtained by [65].

The fitting technique was based on the technique used by [2]. It was performed as following:

1. The results obtained by [65] (see black curve in Figure 6.1 for a plot) were used as initial values for the fitting parameters: magnetic field $B = 0.055$ G, Doppler factor $\delta = 3.9$, electron distribution power law index for low energies $p_1 = 1.6$, electron distribution power law index for high energies $p_2 = 3.6$ and electron distribution cutoff Lorentz factor $\gamma'_c = 4000$.

2. First, the values of B and δ were fixed while the electron distribution parameters (p_1,p_2,γ_c) were varied in a set of quantities centered on the initial values. B and δ are not correlated with the electron distribution parameters [110]. The SSC SED was calculated for each combination of generated values and the χ^2 with the observed core data (without including TeV measurements) was obtained for each of them. Because of the importance of the X-ray data to explain the gamma-ray fluxes, solutions that overcome the *Swift*/BAT upper limits or that differ from *Chandra* data more than 20 $\%$ were excluded. The set with the minimum χ^2 was defined as the new set of initial values. Then, the process was iteratively repeated until it converged.

3. After finding the best values for the electron distribution parameters, they were kept constant while B and δ were varied. Following the same procedure as in the last item the best fit values for those other two parameters were obtained.

6.2.2 Error estimates: SSC component

Errors were estimated using Monte Carlo simulations explained in [111] with the following procedure:

1. 10 000 random values for each observed data point were drawn from their error distributions using the Python function $numpy.random.normal$ [5] . The error distributions were defined to be normal and centered in their observed fluxes with their reported errors as standard deviations. Histograms of the random samples can be found in Figures A.1,A.2,A.3,A.4, A.5 and A.6.

2. 10 000 synthetic SEDs were created using the random values (see Figure 6.1 for a representation of the simulated data points). The best fit values for each synthetic SED were obtained using the procedure described in the last Section with the best fit values for the observed data as initial values. Since the distributions were centered in the observed fluxes, the best fit values for the synthetic SEDs were assumed to be obtained after the first iteration.

3. The error distributions were made using the 10 000 best fit values for each parameter. Confidence limits of 68$\%$, 97$\%$ and 99.5 $\%$ were defined on every error distribution.

6.2.3 Fitting Technique: Photohadronic component

The TeV emission was modeled to be produced by photohadronic interactions (Equation 5.17). Four different sets of data were used for determining the photohadronic model parameters:

1. H.E.S.S observations from 2004: which were taken during a TeV low activity state [72].

2. H.E.S.S observations from 2005: which were taken during a TeV high activity state but without evidence of core activity in the rest of the broadband core spectrum [72].

3. MAGIC-I observations from 2005-2007: Corresponding to an observation campaign where no flaring activity was detected [109].

[5] `https://numpy.org/doc/stable/reference/random/generated/numpy.random.normal.html?numpy.random.normal`

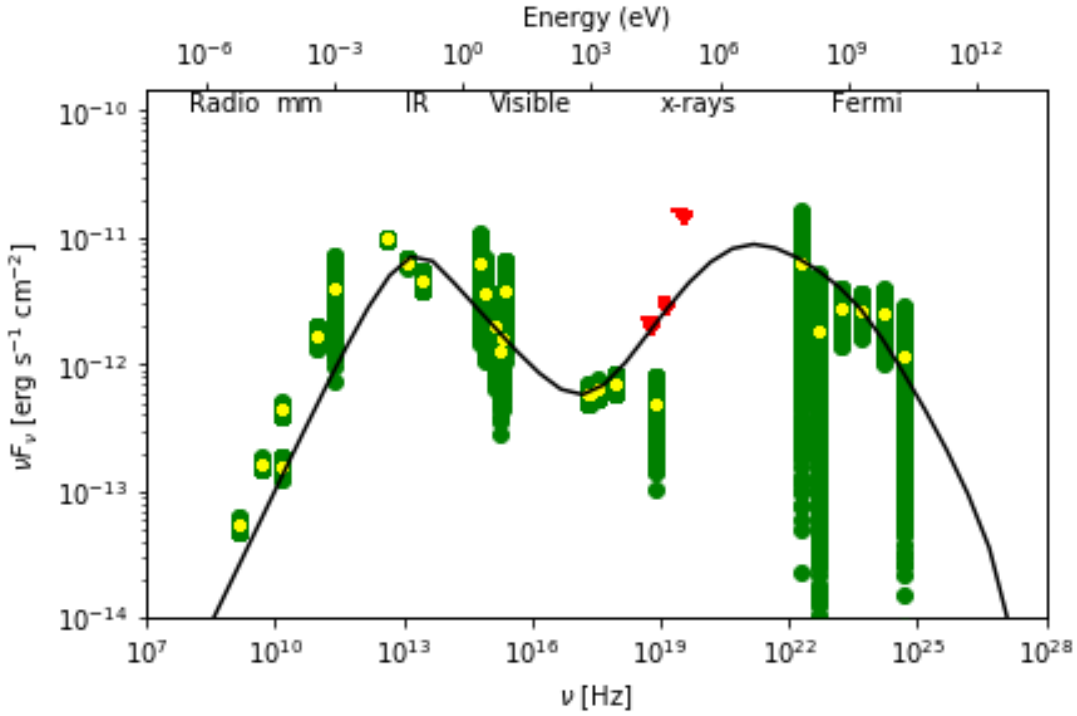

Figure 6.1: SED of M87 constructed with the data points of the Table 6.8. Yellow points correspond to observed data points which were used as mean values for the Monte Carlo simulations. Red triangles correspond to the *Swift*/BAT upper limits. Green points correspond to the data points of the 10 000 synthetic SEDs for the SSC model error estimates. The black curve represents the SSC model fit obtained by [65] whose best fit values were used as initial values in this work.

4. HAWC observations: which cover a long low state period from 2014 to 2019 [78, 97].

Each set of data was separately fitted by the photohadronic model presented in Chapter 5. The fitting parameters are presented in Table 6.10.

It is important to mention that the VHE gamma-ray flux depends on the second component of the SSC model (Equation 5.17):

$$f^{p\gamma}(\epsilon_\Gamma) = A_\gamma f^{ICS}(\nu_\gamma) \left(\frac{\epsilon_\Gamma}{\text{TeV}}\right)^{-\alpha+3}, \tag{6.1}$$

The SSC flux $f^{ICS}(\nu_\gamma)$ was calculated using the best fit values obtained in the SSC model fitting.

The fitting procedure was the following:

1. The corresponding value of $f^{ssc}(\nu_\gamma)$ was calculated for each observed data point with the already obtained best fit values for the SSC model parameters.
2. A set of possible values for α and A_γ (Table 6.10) were defined. The gamma-ray flux was calculated for each combination of parameters at each gamma-ray frequency (including both TeV and MeV-GeV data). The gamma-ray flux was calculated as the sum of the flux corresponding to the photohadronic component and the already obtained inverse Compton component.
3. The χ^2 with the observed data fluxes were calculated for each combination of α and A_γ and the parameters with the minimum χ^2 were defined as the best fit values.

6.2.4 Error estimates: Photohadronic component

The procedure to estimate errors in the photohadronic component is similar to the procedure used for the SSC component. However there are some differences which are explained in this Section:

Parameter	Symbol
Proton distribution power law index	α
VHE gamma-ray flux normalization constant	A_γ

Table 6.10: Fitting parameters for the photohadronic model component

1. It was necessary to generate random samples of values for the SSC model parameters. They were drawn from normal distributions centered on their best fit values with their errors (which were obtained following the procedure described in Section 6.2.2) as standard deviations. Histograms of the random samples for the SSC model parameters are shown in Figure A.10.

2. After generating 10 000 random values for each parameter, 10 000 random values for the VHE fluxes were also generated. They were drawn from normal distributions centered on the observed fluxes and with the observational errors as standard deviations. The Python function $numpy.random.normal$ was used in both cases. Histograms of the random samples made from the TeV data points are plotted in Figure A.7 for the 2004 H.E.S.S. data, in Figure A.8 for the 2005 H.E.S.S. data and in Figure A.9 for the MAGIC data.

3. Then, 10 000 VHE synthetic SEDs were built using the random values for the TeV fluxes. These SEDs were fitted to the photohadronic component model without fixing the SSC model parameters but using the 10 000 random values generated for them (this was done to propagate the errors obtained in the fit of the other two components).

4. The best fit values for each synthetic VHE SED were obtained using the procedure described Section 6.2.3. Using all those results, error distributions for the two model parameters were defined. As it was done for the other parameters, confidence limits of 68$\%$ 97$\%$ and 99.5$\%$ were established on the error distributions.

Chapter 7

Results

As it was mentioned in Chapter 5, the SED fitting was divided into two parts. First, data between radio and GeV gamma rays were fitted with the SSC model presented in Chapter 5. Then VHE gamma rays data were fitted by the sum of the SSC model and the photohadronic model presented in the same Chapter assuming the results obtained in the first fit.

7.1 SSC model fitting

The SSC model fitting has been done following the procedure described in Section 6.2.1. The best fit values of the physical parameter are presented in Table 7.1.

Two restrictions had to be defined during the fitting process. The best fit model was fixed to be below the flux corresponding to the *Swift*/Bat upper limits and it could not differ more than 20 $\%$ from the rest of X-rays fluxes except for the *NuSTAR* data (see Section 8.1). This is because modeling the second component is considered a priority in order to explain the gamma ray emission, while the observational data from the first component could include emission from a more extended region (as it was considered in [75]). Moreover, additional contributions for the X-ray emission (intracluster diffuse emission and unresolved low-mass X-ray binaries) were constrained and subtracted from the fitted data [108].

The best fit model is plotted together with the observational data in Figure 7.1.

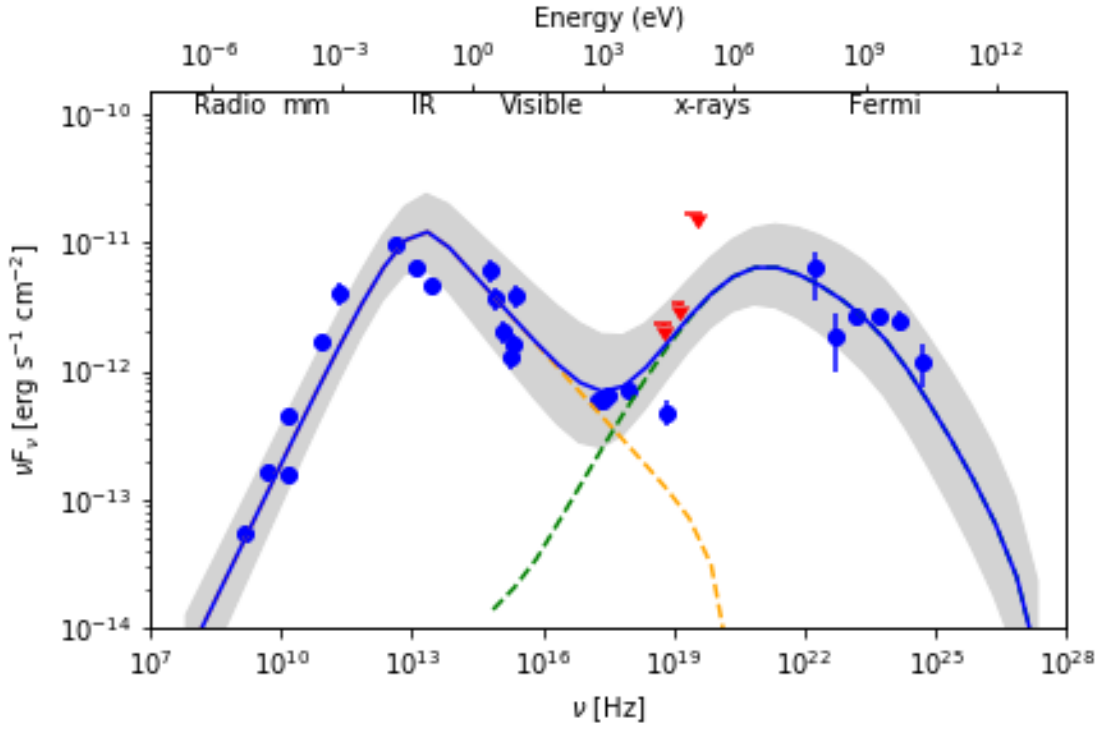

Figure 7.1: SED of M87 with the best fit SSC model. Blue points mark measured core fluxes. The model of the synchrotron component is the orange dashed curve and the model of the inverse Compton component is the green dashed curve. *Swift*/BAT upper limits are marked by red triangles. Gray region corresponds to the 1 σ error of the best fit model parameters

7.2 SSC component: error estimates

Errors of the SSC model parameters were estimated following the procedure described in Section 6.2.2. The obtained error distributions for the parameters are represented in Figure 7.2. Best fit values for the SSC model parameters are given in Table 7.1 with their estimated errors, which correspond to the 68% confidence limits.

Parameter	Value
Magnetic Field B (G)	0.031 ± 0.004
Doppler Factor δ	5.9 ± 0.4
Electron distribution parameters	
Power law index (lower energies) p_1	$1.60^{+0.05}_{-0.10}$
Power law index (higher energies) p_2	3.75 ± 0.10
Break Lorentz factor γ'_c	4400^{+200}_{-100}

Table 7.1: Best fit values for the SSC model parameters with estimated errors.

7.3 Photohadronic model fitting

As it was mentioned before, four different VHE data sets have been considered for modeling the VHE emission of M87.

7.3.1 Fit with H.E.S.S. 2004 data

The photohadronic model fitting parameters have been obtained assuming the SSC model parameters obtained in Section 7.1. The best fit values for parameters are presented in Table 7.2. The best fit model has been plotted together with the observational data in Figure 7.3.

7.3.2 Fit with H.E.S.S. 2005 data

As it was done for the above case, results from Section 7.1 have been assumed. The best fit values for the fitting parameters are presented in Table 7.2. The best fit model has been plotted together with the observational data in Figure 7.4.

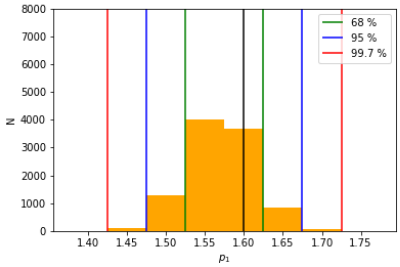

(a) Error distribution obtained for the electron low energy distribution index p_1.

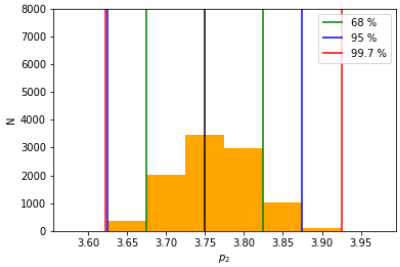

(b) Error distribution obtained for the electron high energy distribution index p_2.

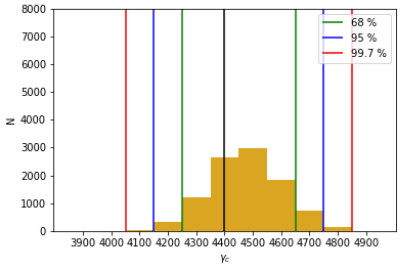

(c) Error distribution obtained for the electron energy distribution break Lorentz factor γ'_c.

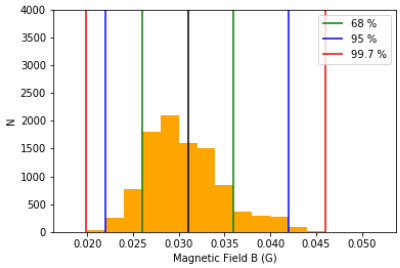

(d) Error distribution obtained for magnetic field B.

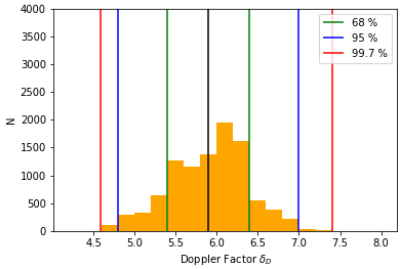

(e) Error distribution obtained for Doppler factor δ.

Figure 7.2: Error distributions obtained for the SSC model parameters. Three confidence limits are indicated in the images (68%, 95%, 99.7% respectively marked by green, blue and red vertical lines) as well as the best fit values which correspond to the black lines.

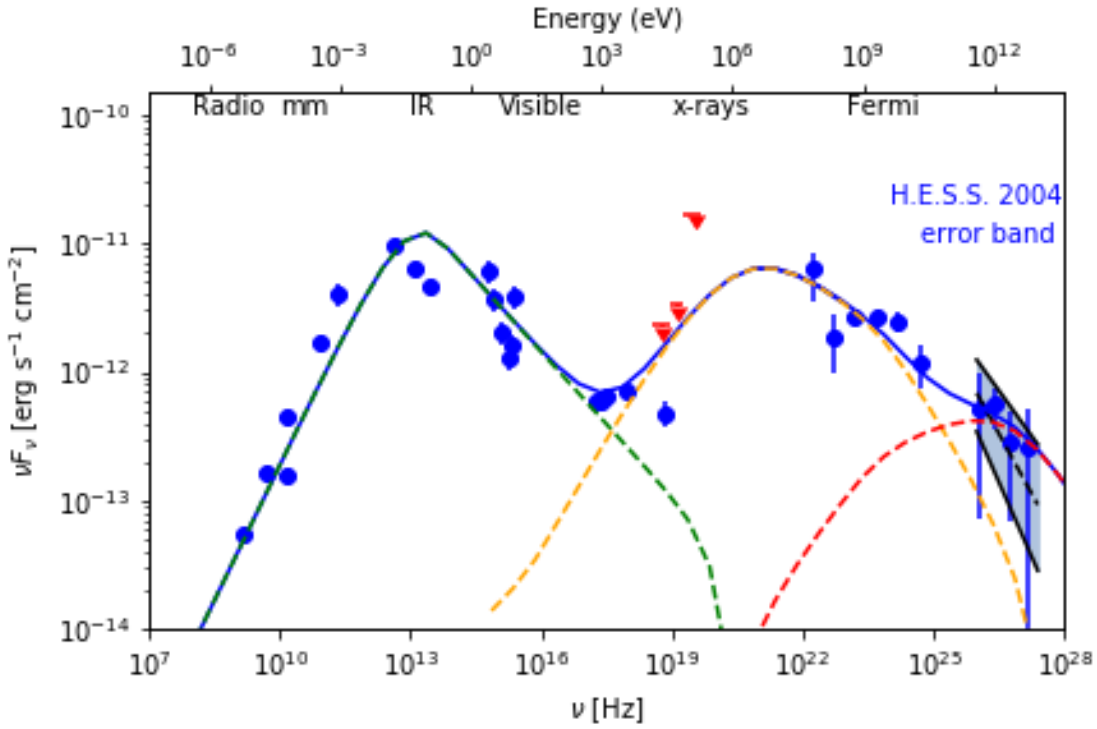

Figure 7.3: SED of M87 with the photohadronic model fit for H.E.S.S. 2004 data. Measured core fluxes are plotted in blue points. The model of the synchrotron component is the green dashed curve and the model of the inverse Compton component is the orange dashed curve. *Swift*/BAT upper limits are presented in red triangles. The model of the photohadronic component is the red dashed curve. H.E.S.S. observed flux band is presented in light blue

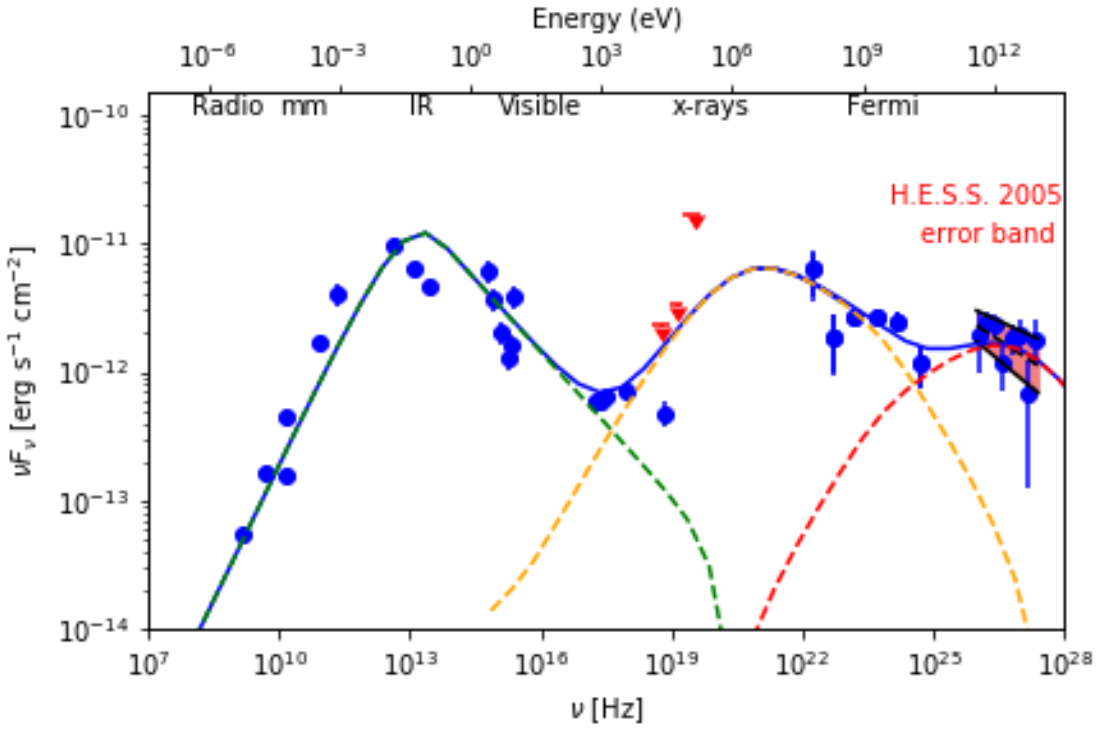

Figure 7.4: SED of M87 with the photohadronic model fit for H.E.S.S. 2005 data. Measured core fluxes are plotted in blue.The model of the synchrotron component is the green dashed curve and the model of the inverse Compton component is the orange dashed curve. *Swift*/BAT upper limits are presented in red. The model of the photohadronic component is the red dashed curve. H.E.S.S. observed flux band is presented in red

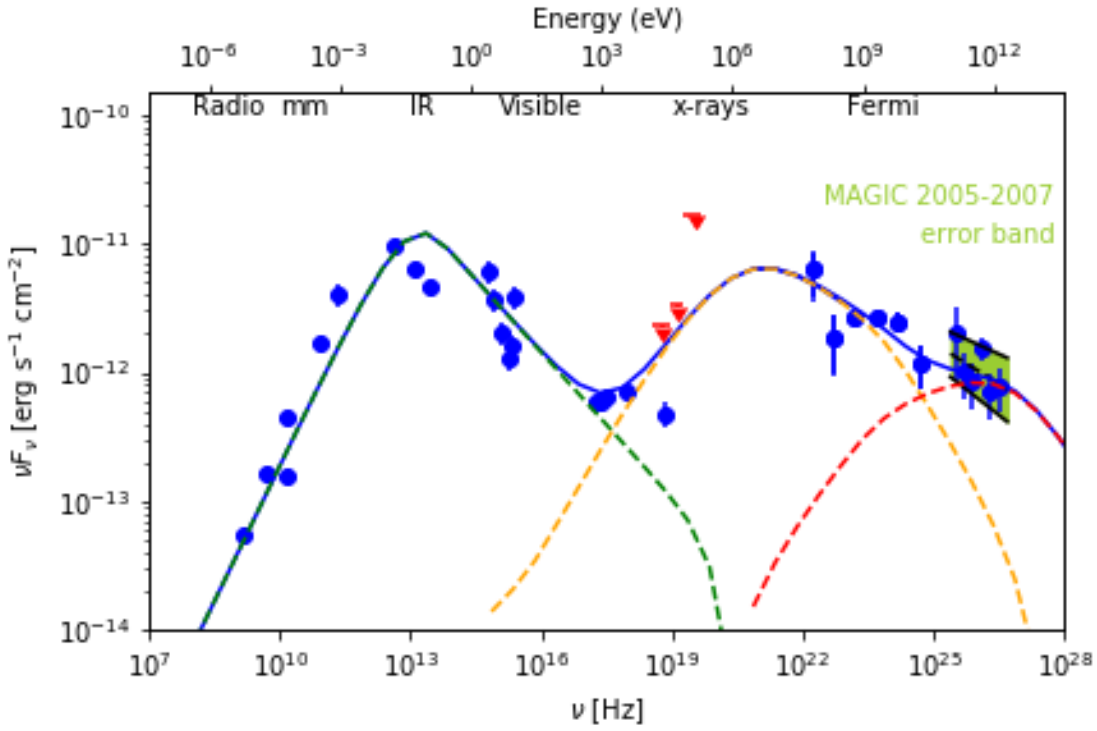

Figure 7.5: SED of M87 with the photohadronic model fit for 2005-2007 MAGIC data. Measured core fluxes are plotted in blue. The synchrotron component is the orange dashed curve and the inverse Compton component is the green dashed curve. *Swift*/BAT upper limits are presented in red triangles. The model of the photohadronic component is the red dashed curve. MAGIC observed flux band is presented in green

7.3.3 Fit with MAGIC data

MAGIC-I observations were also fitted by the photohadronic model. Results for the fitting parameters are presented in Table 7.2. The best fit model and data were plotted in Figure 7.5. As in the other cases, previous SSC results were assumed.

7.3.4 Fit with HAWC data

HAWC results were fitted by the sum of the SSC and the photohadronic models. The results for photohadronic model best fitting parameters are presented in Table 7.2 and they are plotted in Figure 7.6.

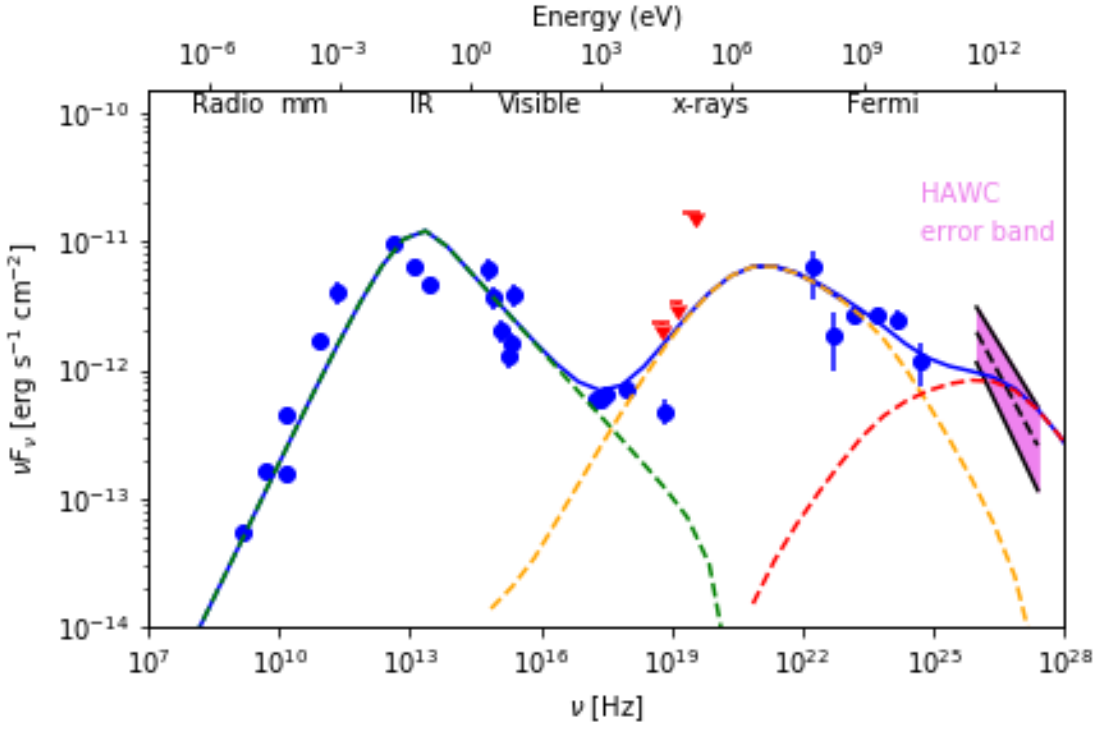

Figure 7.6: SED of M87 with the photohadronic model fit for HAWC data. Measured core fluxes are plotted in blue. The synchrotron component is the orange dashed curve and the inverse Compton component is the green dashed curve. *Swift*/BAT upper limits are presented in red triangles. The model of the photohadronic component is the red dashed curve. HAWC flux band is marked in violet.

7.4 Photohadronic component: error estimates

Errors for the photohadronic component parameters have been estimated using the method explained in Section 6.2.4. Obtained error distributions for both parameters are represented in Figures 7.7,7.8, 7.9 and 7.10. Best fit values with their estimated errors are presented in Table 7.2.

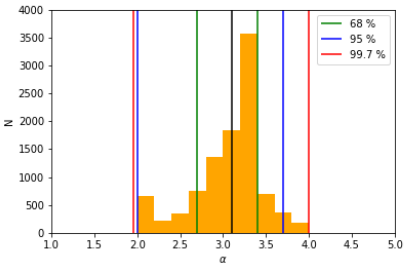

(a) Error distribution of the proton energy distribution index α.

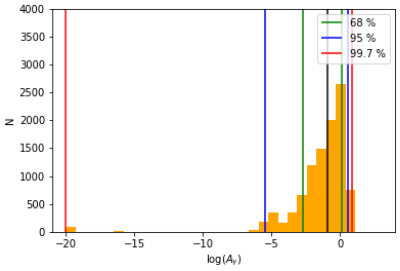

(b) Error distribution of the TeV gamma-ray flux normalization constant A_γ.

Figure 7.7: Error distributions of the photohadronic component fitting parameters for the 2004 H.E.S.S observations. Confidence limits are indicated on the plots (68%, 95%, 99.7% respectively marked by green, blue and red vertical lines). The black lines correspond to the best fit values.

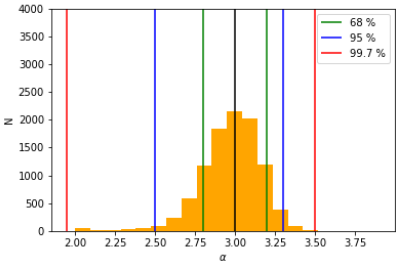

(a) Error distribution of the proton energy distribution index α.

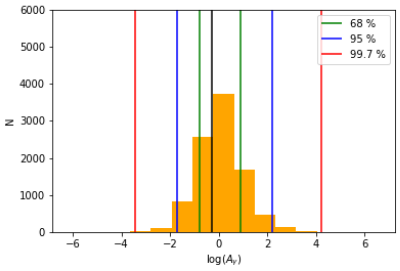

(b) Error distribution of the TeV gamma-ray flux normalization constant A_γ.

Figure 7.8: Error distributions of the photohadronic component fitting parameters for the 2005 H.E.S.S observations. Confidence limits are indicated on the plots (68%, 95%, 99.7% respectively marked by green, blue and red vertical lines). Best fit values are marked by black vertical lines.

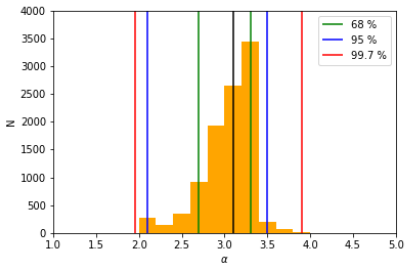

(a) Error distribution of the proton energy distribution index α.

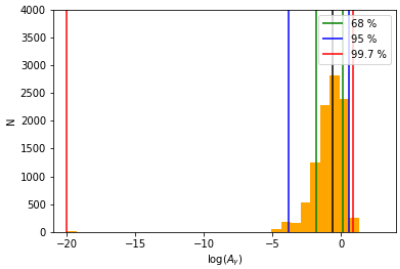

(b) Error distribution of the TeV gamma-ray flux normalization constant A_γ.

Figure 7.9: Error distributions of the photohadronic component fitting parameters for the 2005-2007 MAGIC observations. Confidence limits are indicated on the (68%, 95%, 99.7% respectively marked by green, blue and red vertical lines). Best fit values are marked by black vertical lines black.

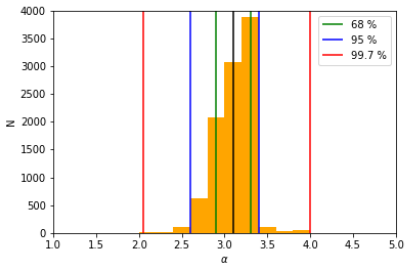

(a) Error distribution of the proton energy distribution index α.

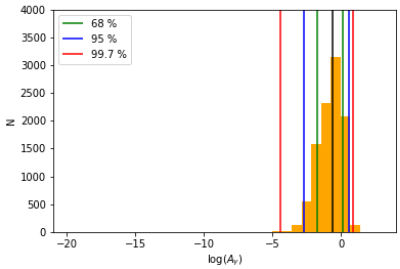

(b) Error distribution of the TeV gamma-ray flux normalization constant A_γ.

Figure 7.10: Error distributions of the photohadronic component fitting parameters for the 2014-2019 HAWC observations. Confidence limits are indicated on the plots (68%, 95%, 99.7% respectively marked by green, blue and red vertical lines). Best fit values are marked by black vertical lines.

Parameter	Value
H.E.S.S. : 2004 observations	
Proton distribution power law index α	$3.1^{+0.3}_{-0.4}$
Gamma-ray flux normalization constant $\log(A_\gamma)$	$-0.9^{+1.0}_{-1.8}$
H.E.S.S.: 2005 observations	
Proton distribution power law index α	3.0 ± 0.2
Gamma-ray flux normalization constant $\log(A_\gamma)$	$-0.6^{+0.6}_{-0.9}$
MAGIC: 2005-2007 observations	
Proton distribution power law index α	$3.1^{+0.2}_{-0.4}$
Gamma-ray flux normalization constant $\log(A_\gamma)$	$-0.6^{+0.7}_{-1.2}$
HAWC observations: 2014-2019	
Proton distribution power law index α	3.1 ± 0.2
Gamma-ray flux normalization constant $\log(A_\gamma)$	$-0.6^{+0.7}_{-1.0}$

Table 7.2: Best fit values for the photohadronic component fitting parameters (see Equation 5.17) with their estimated errors.

Chapter 8

Discussion and Conclusions

8.1 Discussion

Variability studies have suggested that the core of M87 is the most likely to be the source of the VHE emission. The other candidate was the jet feature *HST*-1 but it was disfavored by the VHE timescale variability and the lack of correlated activity in other bands during TeV flares. The broadband SED was built using core data from low activity epochs.

The broadband SED was built using core data from low activity epochs. It was fitted by self-synchrotron Compton and lepto-hadronic models in order to explain its VHE emission. The lepto-hadronic model is a combination between the one-SSC model proposed by [2] and the photohadronic model used by [3]. As it is explained in Chapter 5 the model proposes the existence of three components: a synchrotron dominated component from radio to X-rays, an inverse Compton dominated component from X-rays to GeV gamma rays and a photohadronic dominated component in the range of TeV gamma rays.

The two first SED components were fitted by the SSC model. However, the second component was considered a priority due to the possible contamination of the first component [75] by radio extended emission (due to the low resolution of non-VLBI data), accretion disk emission (as suggested by the Event Horizon Telescope (EHT) observations at 230 GHz [56]) and NUV emission from the region where the jet is launched (as suggested by General Relativistic Radiation Magnetohydynamics [75, 112]). X-ray emission was of particular interest for corresponding to the transition between both regimes and for being important to produce the VHE emission in the photohadronic

scenario. The only X-ray data point which could not be well fitted was the *NuSTAR* 20-40 KeV observation. The authors of the paper that reported this observation also discussed its inconsistency with inverse Compton models to explain gamma-ray emission. According to them, the observation uncertainties are limited by the statistic of their data and deeper observations are necessary to solve the controversy [108].

Table 8.1 shows a comparison of the SSC parameters values obtained by different studies. Two of them (the magnetic field intensity and the break Lorentz factor) present a dispersion of several orders of magnitude. This dispersion can be caused by degeneration in the SED models, different assumptions in the emission zone geometry or different level of completeness in the data sets. In the case of magnetic field intensity (B), most of the degeneration comes from the relation $B\delta^2 R'_b \approx$ constant [2], which was first derived by [113]. As this relation is held in every case of Table 8.1 ($B\delta^2 R'_b \approx (2-4)\times 10^{16}$), variations in the magnetic field intensity (B) can be caused by different assumptions regarding the radius of the emission zone R'_b. The other parameters present a lower dispersion. It is important to remark the absence of error reports in most of the parameter estimations from literature that prevents a more precise comparison of these results.

Parameter	This study	[65]	[80]	[88]	[75]
B(G)	0.031 ± 0.004	0.055	0.002	1.61	0.0031
δ	5.9 ± 0.4	3.9	5	2.8	5.3
p_1	$1.60^{+0.05}_{-0.10}$	1.6	-1.8	3.21 ± 0.02	1.9
p_2	3.75 ± 0.10	3.6	3.4	4.21	3.2
γ'_c	$4.4^{+0.2}_{-0.1} \times 10^3$	4×10^3	4.0×10^2	1.7×10^3	1.4×10^4
R'_b(cm)	$(2.1 \pm 0.1) \times 10^{16}$	1.4×10^{16}	5.6×10^{17}	2.1×10^{15}	4.0×10^{17}

Table 8.1: Comparison of results for the SSC parameters from different studies. All the SEDs were constructed to model the average low-flux state of M87. The value of R'_b for this study was calculated with Equation 5.2

The viewing angle (θ) plays an important role in AGN properties. According to unification schemes, the transition between blazars and radio galaxies is produced around $\theta \sim 10^\circ$. The Doppler factor can be constrained from θ by [68]:

$$\delta \leq \frac{1}{\sin(\theta)}. \tag{8.1}$$

Higher Doppler factors enhance the HE and VHE emission which explains that much more blazars have been detected at gamma-ray energies than radio galaxies.

The Doppler factor value obtained in this work ($\delta = 5.9 \pm 0.4$) is coincident with the lowest estimates for the viewing angle ($\theta \approx 10^\circ - 20^\circ$) [58] which have been based mainly on optical observations of the jet feature *HST*-1. However, it is in disagreement with other estimates ($\theta \approx 30^\circ - 45^\circ$) [66] based on VLBI observations of the jet base of M87. In fact, all the values for δ presented in Table 8.1 are not consistent with the VLBI measurements. A way to solve this controversy is taking into account the width of the jet base. According to [67] the M87 jet base has an apparent opening angle of $\sim 100^\circ$ which would correspond to an intrinsic opening angle of $\sim 50^\circ$ (if $\theta \sim 30^\circ$). Therefore, an VHE emission zone located in the outer zones of the jet base could have a viewing angle as low as $\sim 5^\circ$ which would be consistent with a Doppler factor $\delta \leq 11.5$.

The photohadronic component is able to explain the VHE emission in both low and high activity states. This component is produced by the interaction between inverse Compton photons and accelerated protons of the jet. The low activity case was studied using three different sets of TeV data: H.E.S.S. observations from 2004, MAGIC observations from 2005-2007 and HAWC observations from the 2014-2019 period (the three of them without VHE flares). The high activity state was studied using H.E.S.S. data corresponding to the 2005 VHE flare. There were no reports of core high activity in other bands during that flare. That is why the same broadband SED was used to model the non-flaring state . HAWC results were in agreement with 2004 H.E.S.S. observations and MAGIC observations, but they are lower than the flux of the 2005 flaring state. This indicates that HAWC observations are constraining the average VHE emission from M87 during low activity periods.

The proton energy distribution index α was estimated on the four VHE data sets . The results were $\alpha = 3.1^{+0.3}_{-0.4}$ for the 2004 H.E.S.S. observations $\alpha = 3.0 \pm 0.2$ for the 2005 H.E.S.S. observations, $\alpha = 3.1^{+0.2}_{-0.4}$ for MAGIC observations and $3.1^{+0.7}_{-1.0}$ for HAWC observations . Those measurements agree with the result obtained by [88] $\alpha = 2.80 \pm 0.02$ where a similar lepto-hadronic model was used to fit the 2004 H.E.S.S. data. It is important to remark the change in α observed in the 2005 H.E.S.S. observation respect to other TeV results and the lack of high activity in the other bands during this flare. Those results indicate that the flare was likely caused by an energy increase of the accelerated proton population.

The normalization constant A_γ presents relatively large uncertainties in its determinations (see Table 7.2). This can be caused by the large observational errors in gamma-ray flux measurements. However, it can be noticed (see Figures 7.7, 7.8, 7.9 and 7.10) that Monte Carlo simulations give results as low as $A\gamma \sim 10^{-20}$. Those extremely low values could be interpreted as simulated cases where a SSC model can explain the VHE emission by itself. Extremely low values correspond to only 138 of

10000 for the H.E.S.S. data from 2004, only 4 of 10000 for the H.E.S.S. data from 2005, only 26 of 10000 for the MAGIC data an and only 1 of 10000 for the HAWC results.
It is important to mention that HAWC data are the only continuous TeV measurements. The IACTs observations are made with exposure times corresponding to a few hours that could be affected by rapid VHE flux variations. Therefore, HAWC results represent an actual constraint to the mean VHE emission of M87 during the study period.

Regarding the results of some other alternative models. In [88] the SED of M87 was fitted by a very similar lepto-hadronic model. However, X-ray results are not well fitted and the model is above the *Swift*/BAT upper limits (see Figure 3.7). Moreover, VHE emission is represented only by the 2004 H.E.S.S. results that were obtained with just ~ 50 hours of observation. However, the best fitting values of the photohadronic parameters were in agreement, within their uncertainties, with those obtained in this work.

Multi-zone SSC models include many additional parameters that are difficult to fit. Most of them were proposed before data from *Fermi* LAT were available and they predicted MeV-GeV fluxes higher than observed during flaring states. The relatively low X-ray flux that is observed in M87 also disfavours these models. However, multi-zone SSC models are still good candidates to explain the VHE emission of M87 and they could be complementary to the photohadronic scenario [82, 84].

Some other models like the misaligned minijets proposed by [83] need more observations to be confirmed or discarded. Hadronic models are also capable of explaining the VHE emission of M87. However, low-energy emission (including X-rays) is hardly explained by these models and leptonic emission has to be included [114].

8.2 Conclusions

A broadband SED of the M87 core has been fitted by a lepto-hadronic model with the aim to explain the VHE emission from the galaxy. Emission from radio to GeV gamma has been modelled to be produced in a SSC scenario explained in Chapter 5. The best fit values for SSC model parameters were for the Doppler factor $\delta = 5.9 \pm 0.4$, for the mean magnetic field intensity $B = 0.031 \pm 0.004$ G, for the electron energy distribution parameters $p_1 = 1.60^{+0.05}_{-0.10}$, $p_2 = 3.75 \pm 0.10$ and $\gamma'_c = 4.4^{0.2}_{0.1} \times 10^3$. The value of the Doppler factor is in agreement with a low viewing angle of the jet base. However, a large viewing angle is also possible if the opening angle of the jet base is enough to

place the emission zone closer to the observer's line of sight.

The VHE emission is fitted by a photohadronic model. Results show that this model is able to explain the VHE low activity emission represented by H.E.S.S., MAGIC and HAWC observations. H.E.S.S. data corresponding to the 2005 VHE flare were also fitted using this model. The results show that the model can explain the so called "orphan flares" that are only detected at VHE bands such as the one observed in 2005. Those flares would be produced by changes in the proton energy distribution.

HAWC observations constrained the VHE emission from M87 for the 2015-2019 period in which no evidence of VHE flares was reported. A proton energy distribution power law index of $\alpha = 3.1 \pm 0.2$ and TeV gamma-ray flux normalization constant of $\log(A_\gamma) = 0.6^{+0.7}_{-1.0}$ were obtained. HAWC will be taking data for a few more years. Therefore, the significance of the M87 detection will probably be improved allowing a better estimation of the photohadronic model parameters.

8.3 Future work

A future study could take into account variability effects in M87 broadband SED. Even if the basic state of the emission is well identified it would be interesting to study variability in the model parameters. This is particularly important to explain the 2008 and 2010 VHE flares in which the M87 core flux increased in other bands.

The model could be also extended to include additional considerations such a more complex geometry (e.g. a second emission zone [115]). Those consideration would add more free parameters to the model (in the case of two zone models, twice as many as in single-zone ones). However, additional data such as optical polarization and VLBI observations could help to constrain some of those parameters [116].

Another possible future development is to calculate the Ultra High Energy Cosmic Rays (UHECR) flux and neutrino flux produced by M87 which could be detected from Earth. Neutrinos are produced by charged pion decays in photohadronic cascades and part of the UHECR particles could be accelerated in Active Galactic Nuclei. Due to its proximity and activity M87 is an excellent candidate to make a contribution in this field [88].

Finally, it would be interesting to perform this analysis in other radio galaxies such as IC 310 and NGC 1275, which have shown VHE emission in the past and may be detected by HAWC in the next years.

Appendix A

Random samples for the Monte Carlo simulations

A.1 Histograms of random samples for SED data points and random samples SSC model parameters

The random samples for the Monte Carlo simulations were obtained using the Python function $numpy.random.normal$. They were drawn from a Gaussian distribution for each data point with the observed flux as mean and the reported error as standard deviation. Random samples of SSC model parameters were drawn from a Gaussian distribution for each data point with the best fit values as mean and its error as standard deviation. Histograms representing the samples used at each data point are shown in the following figures:

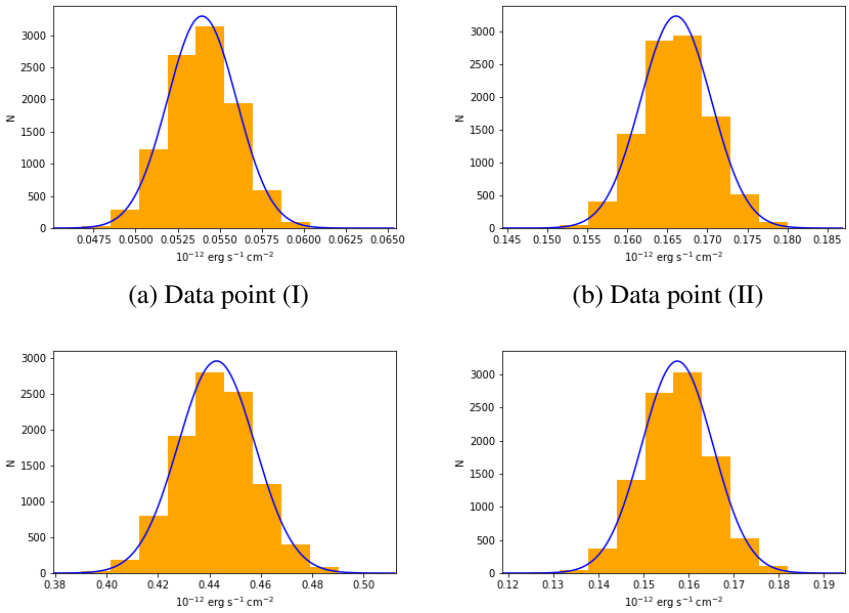

(a) Data point (I)

(b) Data point (II)

(c) Data point (III)

(d) Data point (IV)

Figure A.1: Random sample histograms for radio data points. Fluxes, errors and frequencies for each data point are written in Table 6.8 . Observational details are summarized in Section 6.1.1

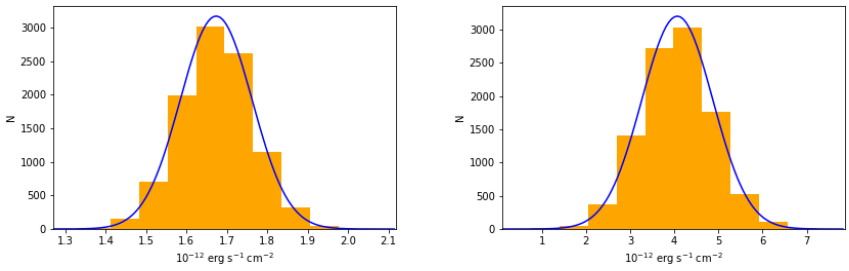

(a) Data point (V)

(b) Data point (VI)

Figure A.2: Random sample histograms for mm data points. Fluxes, errors and frequencies for each data point are written in Table 6.8 . Observational details are summarized in Section 6.1.2

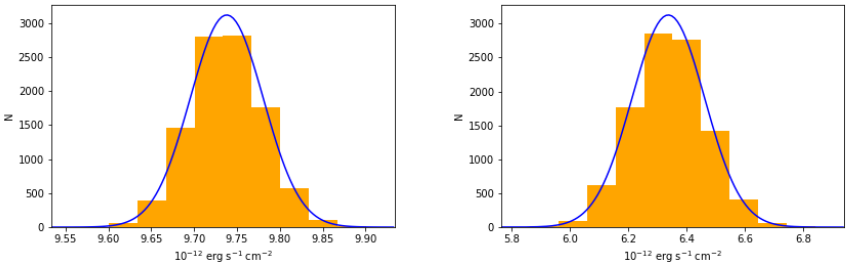

(a) Data point (VII)

(b) Data point (VIII)

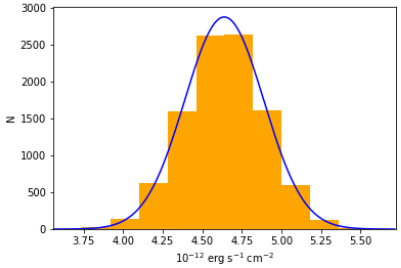

(c) Data point (IX)

Figure A.3: Random sample histograms for IR data points. Fluxes, errors and frequencies for each data point are written in Table 6.8 . Observational details are summarized in Section 6.1.3

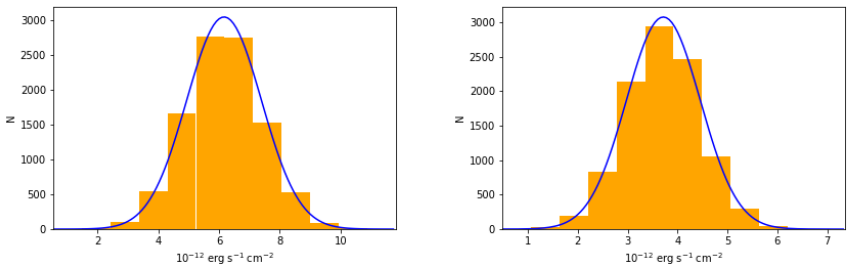

(a) Data point (X)

(b) Data point (XI)

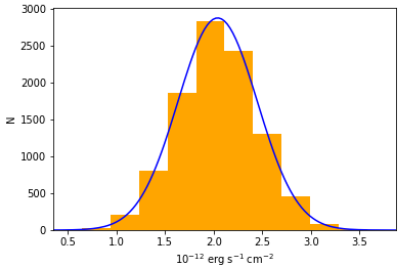

(c) Data point (XII)

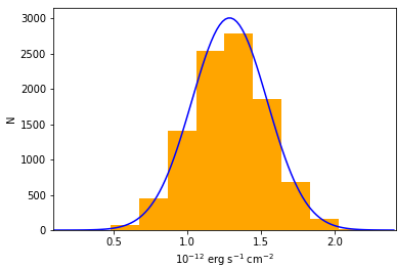

(d) Data point (XIII)

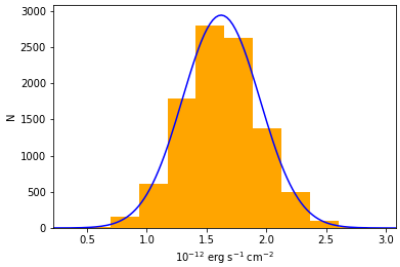

(e) Data point (XIV)

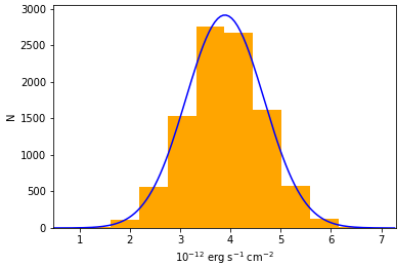

(f) Data point (XV)

Figure A.4: Random sample histograms for visible and UV data points. Fluxes, errors and frequencies for each data point are written in Table 6.8 . Observational details are summarized in Section 6.1.4

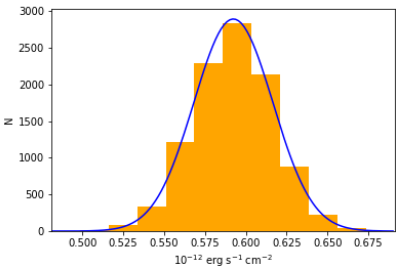

(a) Data point (XVI)

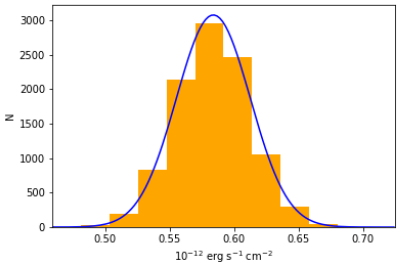

(b) Data point (XVII)

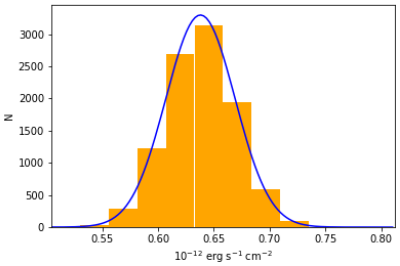

(c) Data point (XVIII)

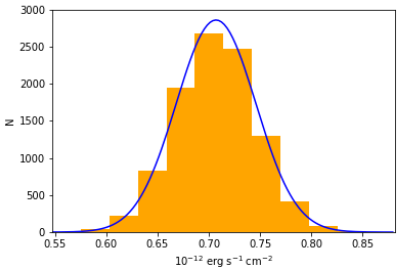

(d) Data point (XIX)

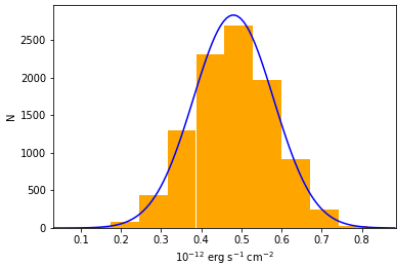

(e) Data point (XX)

Figure A.5: Random sample histograms for X-ray data points. Fluxes, errors and frequencies for each data point are written in Table 6.8 . Observational details are summarized in Section 6.1.5

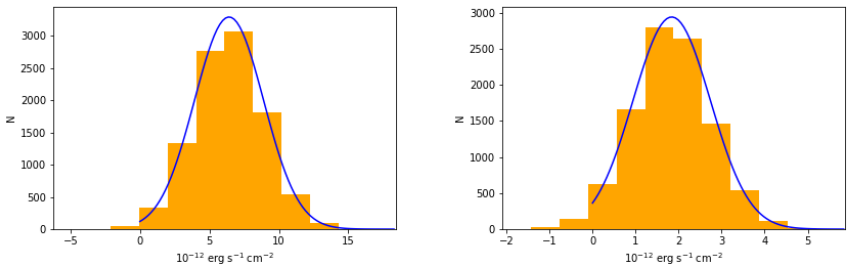

(a) Data point (XXIV)

(b) Data point (XXV)

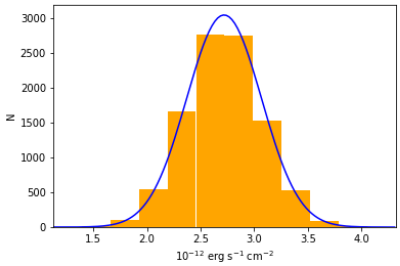

(c) Data point (XXVI)

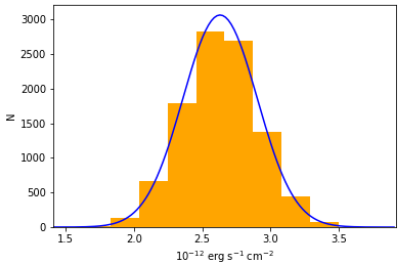

(d) Data point (XXVII)

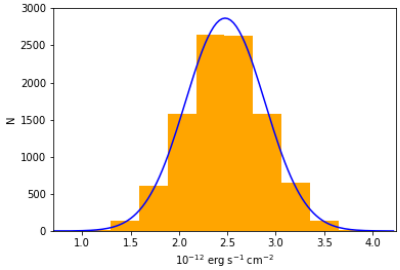

(e) Data point (XXVIII)

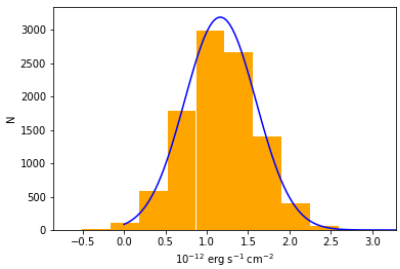

(f) Data point (XXIX)

Figure A.6: Random sample histograms for MeV-GeV gamma-ray data points. Fluxes, errors and frequencies for each data point are written in Table 6.8 . Observational details are summarized in Section 6.1.6

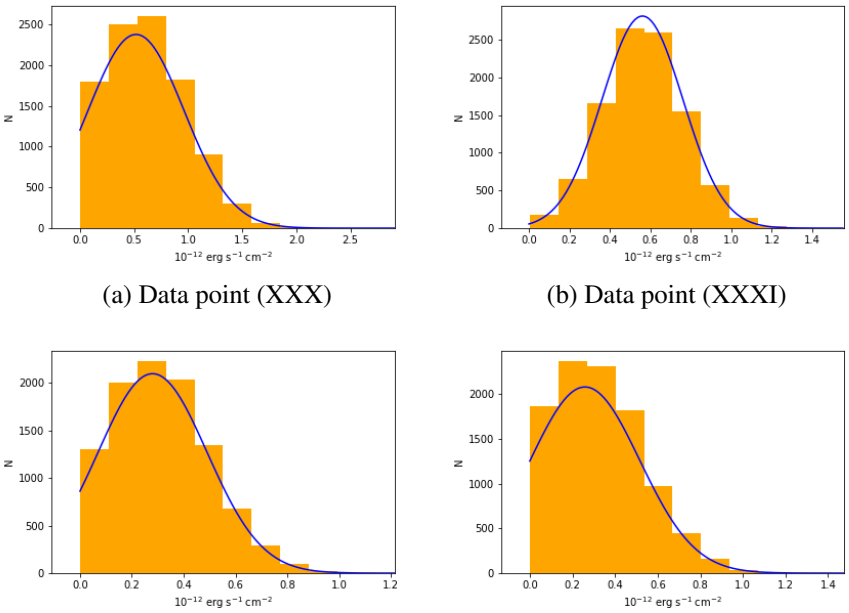

(a) Data point (XXX)

(b) Data point (XXXI)

(c) Data point (XXXII)

(d) Data point (XXXIII)

Figure A.7: Random sample histograms for TeV gamma-ray data points from 2004 H.E.S.S. observations [72] . Fluxes, errors and frequencies for each data point are written in Table 6.8 . Observational details are summarized in Section 6.1.6

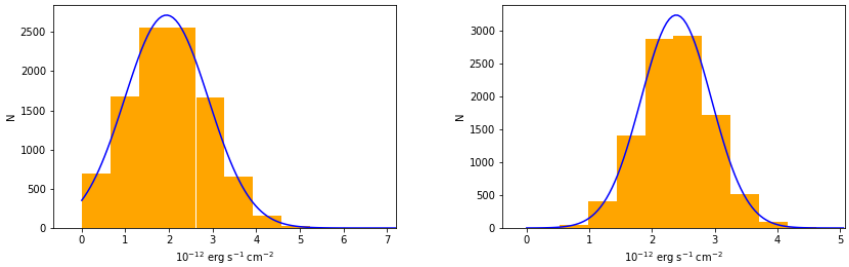

(a) Data point (XXXIV)

(b) Data point (XXXV)

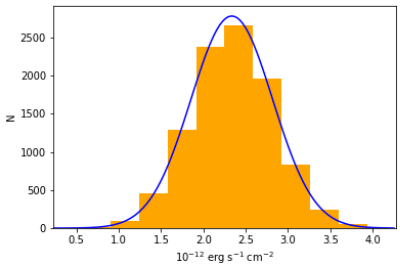

(c) Data point (XXXVI)

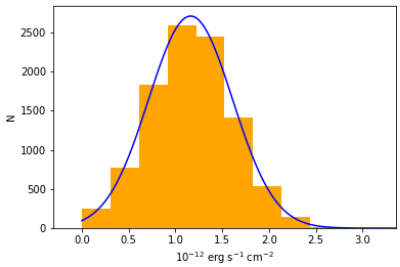

(d) Data point (XXXVII)

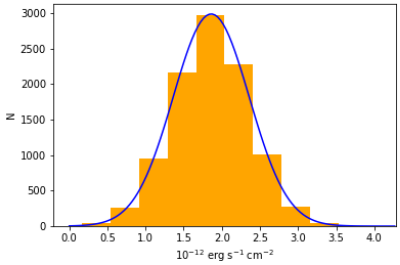

(e) Data point (XXXVIII)

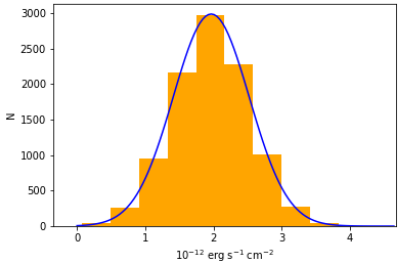

(f) Data point (XXXIX)

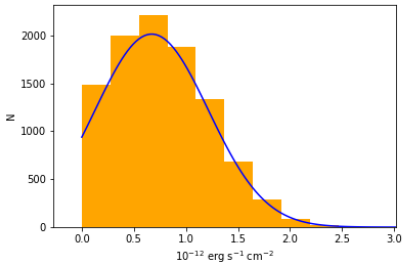

(g) Data point (XL)

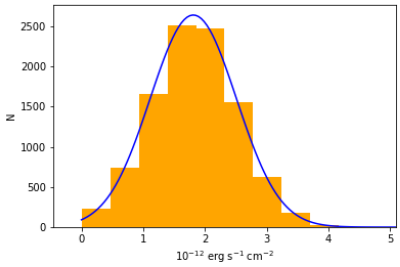

(h) Data point (XLI)

Figure A.8: Random sample histograms for TeV gamma-ray data points from 2005 H.E.S.S. observations [72] . Fluxes, errors and frequencies for each data point are written in Table 6.8 . Observational details are summarized in Section 6.1.6

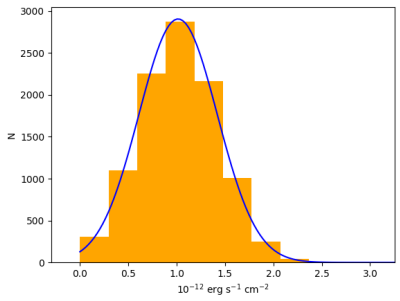

(a) Data point (XLII)

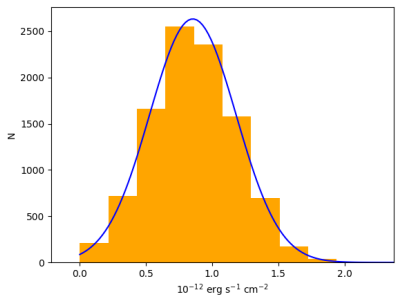

(b) Data point (XLIII)

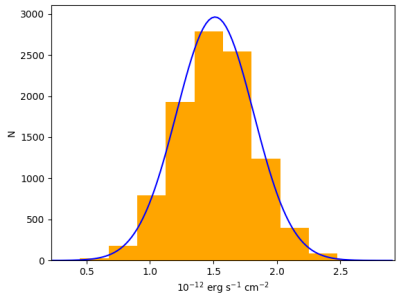

(c) Data point (XLIV)

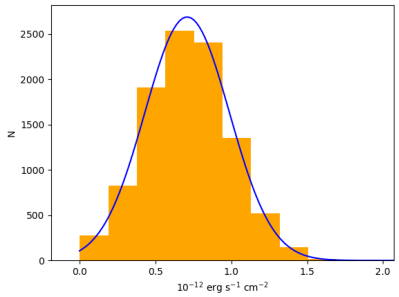

(d) Data point (XLV)

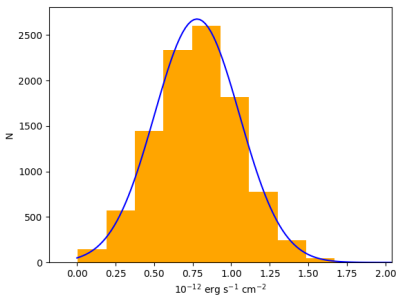

(e) Data point (XLVI)

Figure A.9: Random sample histograms for TeV gamma-ray data points from 2005-2007 MAGIC observations [72] . Fluxes, errors and frequencies for each data point are written in Table 6.8 . Observational details are summarized in Section 6.1.6

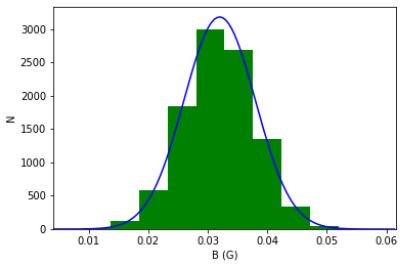

(a) Magnetic field B (G)

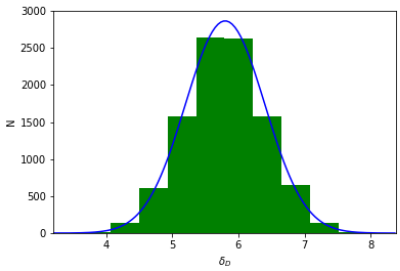

(b) Doppler factor δ_D

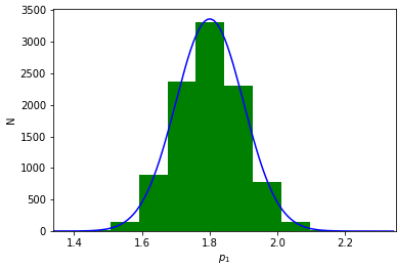

(c) Electron low energy distribution index p_1

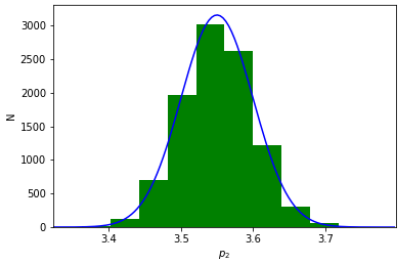

(d) Electron high energy distribution index p_2

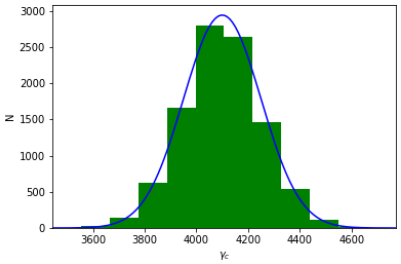

(e) Electron energy distribution break Lorentz factor γ_c'

Figure A.10: Random sample histograms for SSC model parameters.

References

[1] R. Blandford, D. Meier, and A. Readhead, "Relativistic Jets from Active Galactic Nuclei," *Annual Review of Astronomy and Astrophysics*, vol. 57, pp. 467–509, 2019.

[2] J. D. Finke, C. D. Dermer, and M. Böttcher, "Synchrotron self-Compton analysis of TeV X-ray-selected BL Lacertae objects," *The Astrophysical Journal*, vol. 686, no. 1, p. 181, 2008.

[3] S. Sahu, "Multi-TeV flaring in nearby High Energy Blazars: A photohadronic scenario," *arXiv preprint arXiv:1907.01174*, 2019.

[4] F. M. Rieger and A. Levinson, "Radio Galaxies at VHE energies," *Galaxies*, vol. 6, no. 4, p. 116, 2018.

[5] A. Abramowski, F. Acero, F. Aharonian, A. Akhperjanian, G. Anton, A. Balzer, A. Barnacka, U. B. De Almeida, Y. Becherini, J. Becker, *et al.*, "The 2010 very high energy γ-ray flare and 10 years of multi-wavelength observations of M 87," *The Astrophysical Journal*, vol. 746, no. 2, p. 151, 2012.

[6] F. A. Benkhali, N. Chakraborty, and F. M. Rieger, "Complex gamma-ray behavior of the radio galaxy m 87," *Astronomy & Astrophysics*, vol. 623, p. A2, 2019.

[7] H. Netzer, *The physics and evolution of active galactic nuclei*. Cambridge University Press, 2013.

[8] M. S. Longair, *High energy astrophysics*. Cambridge University Press, 2011.

[9] S. L. Shapiro and S. A. Teukolsky, *Black holes, white dwarfs, and neutron stars: The physics of compact objects*. John Wiley & Sons, 2008.

[10] R. Fender and T. Muñoz-Darias, "The balance of power: accretion and feedback in stellar mass black holes," in *Astrophysical Black Holes*, pp. 65–100, Springer, 2016.

[11] P. Du, C. Hu, K.-X. Lu, Y.-K. Huang, C. Cheng, J. Qiu, Y.-R. Li, Y.-W. Zhang, X.-L. Fan, J.-M. Bai, *et al.*, "Supermassive black holes with high accretion rates in active galactic nuclei. IV. Hβ time lags and implications for super-eddington accretion," *The Astrophysical Journal*, vol. 806, no. 1, p. 22, 2015.

[12] H. Netzer, "Revisiting the unified model of active galactic nuclei," *Annual Review of Astronomy and Astrophysics*, vol. 53, pp. 365–408, 2015.

[13] P. Padovani, D. Alexander, R. Assef, B. De Marco, P. Giommi, R. Hickox, G. Richards, V. Smolčić, E. Hatziminaoglou, V. Mainieri, *et al.*, "Active galactic nuclei: what's in a name?," *The Astronomy and Astrophysics Review*, vol. 25, no. 1, p. 2, 2017.

[14] S. Abdollahi, F. Acero, M. Ackermann, M. Ajello, W. B. Atwood, M. Axelsson, L. Baldini, J. Ballet, G. Barbiellini, D. Bastieri, J. B. Gonzalez, R. Bellazzini, A. Berretta, E. Bissaldi, R. D. Blandford, E. D. Bloom, R. Bonino, E. Bottacini, T. J. Brandt, J. Bregeon, P. Bruel, R. Buehler, T. H. Burnett, S. Buson, R. A. Cameron, R. Caputo, P. A. Caraveo, J. M. Casandjian, D. Castro, E. Cavazzuti, E. Charles, S. Chaty, S. Chen, C. C. Cheung, G. Chiaro, S. Ciprini, J. Cohen-Tanugi, L. R. Cominsky, J. Coronado-Blázquez, D. Costantin, A. Cuoco, *et al.*, "Fermi large area telescope fourth source catalog," *The Astrophysical Journal Supplement Series*, vol. 247, p. 33, mar 2020.

[15] U. Klein, U. Lisenfeld, and S. Verley, "Radio synchrotron spectra of star-forming galaxies," *Astronomy & Astrophysics*, vol. 611, p. A55, 2018.

[16] J. Kormendy and D. Richstone, "Inward bound—the search for supermassive black holes in galactic nuclei," *Annual Review of Astronomy and Astrophysics*, vol. 33, no. 1, pp. 581–624, 1995.

[17] R. Blandford and C. McKee, "Reverberation mapping of the emission line regions of Seyfert galaxies and quasars," *The Astrophysical Journal*, vol. 255, pp. 419–439, 1982.

[18] L. Ferrarese and D. Merritt, "A fundamental relation between supermassive black holes and their host galaxies," *The Astrophysical Journal Letters*, vol. 539, no. 1, p. L9, 2000.

[19] The EHT Collaboration *et al.*, "First M87 Event Horizon Telescope Results. VI. The Shadow and Mass of the Central Black Hole," *The Astrophysical Journal Letters*, vol. 875, p. 6, 2019.

[20] R. D. Blandford and R. L. Znajek, "Electromagnetic extraction of energy from Kerr black holes," *Monthly Notices of the Royal Astronomical Society*, vol. 179, no. 3, pp. 433–456, 1977.

[21] F. Rieger and F. Aharonian, "Variable VHE gamma-ray emission from non-blazar AGNs," *Astronomy & Astrophysics*, vol. 479, no. 1, pp. L5–L8, 2008.

[22] N. I. Shakura and R. A. Sunyaev, "Black holes in binary systems. Observational appearance.," *Astronomy and Astrophysics*, vol. 24, pp. 337–355, 1973.

[23] A. S. Wilson and E. J. M. Colbert, "The Difference between Radio-loud and Radio-quiet Active Galaxies," , vol. 438, p. 62, Jan. 1995.

[24] M. Chiaberge and A. Marconi, "On the origin of radio loudness in active galactic nuclei and its relationship with the properties of the central supermassive black hole," *Monthly Notices of the Royal Astronomical Society*, vol. 416, pp. 917–926, 09 2011.

[25] V. Beckmann and C. Shrader, *Active galactic nuclei*. John Wiley & Sons, 2013.

[26] R. Antonucci, "Unified models for active galactic nuclei and quasars," *Annual review of astronomy and astrophysics*, vol. 31, pp. 473–521, 1993.

[27] C. M. Urry and P. Padovani, "Unified schemes for radio-loud active galactic nuclei," *Publications of the Astronomical Society of the Pacific*, vol. 107, no. 715, p. 803, 1995.

[28] I. Ordovás-Pascual, S. Mateos, F. J. Carrera, K. Wiersema, X. Barcons, V. Braito, A. Caccianiga, A. Del Moro, R. Della Ceca, and P. Severgnini, "AGNs with discordant optical and X-ray classification are not a physical family: diverse origin in two AGNs," *Monthly Notices of the Royal Astronomical Society*, vol. 469, no. 1, pp. 693–704, 2017.

[29] C. Tadhunter, "An introduction to active galactic nuclei: Classification and unification," *New Astronomy Reviews*, vol. 52, no. 6, pp. 227–239, 2008.

[30] F. Acero, M. Ackermann, M. Ajello, A. Albert, W. Atwood, M. Axelsson, L. Baldini, J. Ballet, G. Barbiellini, D. Bastieri, *et al.*, "Fermi large area telescope third source catalog," *The Astrophysical Journal Supplement Series*, vol. 218, no. 2, p. 23, 2015.

[31] R. Falomo, E. Pian, and A. Treves, "An optical view of BL Lacertae objects," *The Astronomy and Astrophysics Review*, vol. 22, no. 1, p. 73, 2014.

[32] P. Padovani, P. Giommi, and A. Rau, "The discovery of high-power high synchrotron peak blazars," *Monthly Notices of the Royal Astronomical Society: Letters*, vol. 422, no. 1, pp. L48–L52, 2012.

[33] J. Torres-Zafra, S. A. Cellone, A. Buzzoni, I. Andruchow, and J. G. Portilla, "Redshift determination of the BL Lac object 3C 66A by the detection of its host galaxy cluster at z= 0.340," *Monthly Notices of the Royal Astronomical Society*, vol. 474, no. 3, pp. 3162–3172, 2018.

[34] D. Rosa González, H. Muriel, Y. Mayya, I. Aretxaga, J. Becerra González, A. Carramiñana, J. Méndez-Abreu, O. Vega, E. Terlevich, S. Coutiño de León, *et al.*, "New GTC spectroscopic data and a statistical study to better constrain the redshift of the BL Lac RGB J2243+ 203," *Monthly Notices of the Royal Astronomical Society*, vol. 482, no. 4, pp. 5422–5429, 2019.

[35] H. Muriel, C. Donzelli, A. C. Rovero, and A. Pichel, "The BL-Lac gamma-ray blazar PKS 0447-439 as a probable member of a group of galaxies at z= 0.343," *Astronomy & Astrophysics*, vol. 574, p. A101, 2015.

[36] G. Madejski and M. Sikora, "Gamma-ray observations of active galactic nuclei," *Annual Review of Astronomy and Astrophysics*, vol. 54, pp. 725–760, 2016.

[37] C. D. Dermer and B. Giebels, "Active galactic nuclei at gamma-ray energies," *Comptes Rendus Physique*, vol. 17, no. 6, pp. 594–616, 2016.

[38] R. Hartman, D. Bertsch, S. Bloom, A. Chen, P. Deines-Jones, J. Esposito, C. Fichtel, D. Friedlander, S. Hunter, L. McDonald, *et al.*, "The third EGRET catalog of high-energy

gamma-ray sources," *The Astrophysical Journal Supplement Series*, vol. 123, no. 1, p. 79, 1999.

[39] B. L. Fanaroff and J. M. Riley, "The morphology of extragalactic radio sources of high and low luminosity," *Monthly Notices of the Royal Astronomical Society*, vol. 167, no. 1, pp. 31P–36P, 1974.

[40] A. Capetti, F. Massaro, and R. D. Baldi, "FRIICAT: a FIRST catalog of FR II radio galaxies," *Astronomy & Astrophysics*, vol. 601, p. A81, 2017.

[41] S. P. Wakely and D. Horan, "TeVCat: An online catalog for Very High Energy Gamma-Ray Astronomy," *International Cosmic Ray Conference*, vol. 3, pp. 1341–1344, 2008.

[42] A. M. Hillas, "The origin of ultra-high-energy cosmic rays," *Annual review of astronomy and astrophysics*, vol. 22, no. 1, pp. 425–444, 1984.

[43] A. Aab, P. Abreu, M. Aglietta, I. Al Samarai, I. Albuquerque, I. Allekotte, A. Almela, J. A. Castillo, J. Alvarez-Muñiz, G. A. Anastasi, *et al.*, "Observation of a large-scale anisotropy in the arrival directions of cosmic rays above $8\times 10^{1}8$ eV," *Science*, vol. 357, no. 6357, pp. 1266–1270, 2017.

[44] Ice Cube Collaboration *et al.*, "Multimessenger observations of a flaring blazar coincident with high-energy neutrino IceCube-170922A," *Science*, vol. 361, no. 6398, p. eaat1378, 2018.

[45] G. B. Rybicki and A. P. Lightman, *Radiative processes in astrophysics*. John Wiley & Sons, 2008.

[46] J. D. Finke, "External Compton scattering in blazar jets and the location of the gamma-ray emitting region," *The Astrophysical Journal*, vol. 830, no. 2, p. 94, 2016.

[47] C. D. Dermer and G. Menon, *High energy radiation from black holes: gamma rays, cosmic rays, and neutrinos*, vol. 17. Princeton University Press, 2009.

[48] P. B. Graff, M. Georganopoulos, E. S. Perlman, and D. Kazanas, "A multizone model for simulating the high-energy variability of TeV blazars," *The Astrophysical Journal*, vol. 689, no. 1, p. 68, 2008.

[49] L. A. Anchordoqui, "Ultra-high-energy cosmic rays," *Physics Reports*, vol. 801, pp. 1 – 93, 2019. Ultra-high-energy cosmic rays.

[50] A. A. Abdo, M. Ackermann, M. Ajello, L. Baldini, J. Ballet, G. Barbiellini, D. Bastieri, K. Bechtol, R. Bellazzini, B. Berenji, *et al.*, "Fermi Large Area Telescope observations of markarian 421: The missing piece of its spectral energy distribution," *The Astrophysical Journal*, vol. 736, no. 2, p. 131, 2011.

[51] N. Sahakyan, "Lepto-hadronic γ-ray and neutrino emission from the jet of TXS 0506+ 056," *The Astrophysical Journal*, vol. 866, no. 2, p. 109, 2018.

[52] S. Mei, J. P. Blakeslee, P. Côté, J. L. Tonry, M. J. West, L. Ferrarese, A. Jordán, E. W. Peng, A. Anthony, and D. Merritt, "The ACS Virgo cluster survey. XIII. SBF distance catalog and the three-dimensional structure of the Virgo cluster," *The Astrophysical Journal*, vol. 655, no. 1, p. 144, 2007.

[53] M. Doherty, M. Arnaboldi, P. Das, O. Gerhard, J. A. L. Aguerri, R. Ciardullo, J. J. Feldmeier, K. C. Freeman, G. H. Jacoby, and G. Murante, "The edge of the M 87 halo and the kinematics of the diffuse light in the Virgo cluster core," *Astronomy & Astrophysics*, vol. 502, no. 3, pp. 771–786, 2009.

[54] L. Zhu, R. Long, S. Mao, E. W. Peng, C. Liu, N. Caldwell, B. Li, J. P. Blakeslee, P. Côté, J.-C. Cuillandre, *et al.*, "The Next Generation Virgo Cluster Survey. V. modeling the dynamics of M87 with the made-to-measure method," *The Astrophysical Journal*, vol. 792, no. 1, p. 59, 2014.

[55] B. Cook, C. Conroy, and P. van Dokkum, "Measuring Star Formation Histories, Distances, and Metallicities with Pixel Color–Magnitude Diagrams. II. Applications to Nearby Elliptical Galaxies," *The Astrophysical Journal*, vol. 893, no. 2, p. 160, 2020.

[56] The EHT Collaboration *et al.*, "First M87 Event Horizon Telescope Results. I. The Shadow of the Supermassive Black Hole," *The Astrophysical Journal Letters*, vol. 875, p. 1, 2019.

[57] H. D. Curtis, "Descriptions of 762 nebulae and clusters photographed with the Crossley reflector," *Publications of Lick Observatory*, vol. 13, pp. 9–42, 1918.

[58] J. Biretta, W. Sparks, and F. Macchetto, "Hubble Space Telescope observations of superluminal motion in the M87 jet," *The Astrophysical Journal*, vol. 520, no. 2, p. 621, 1999.

[59] E. S. Perlman, J. A. Biretta, F. Zhou, W. B. Sparks, and F. D. Macchetto, "Optical and Radio Polarimetry of the M87 jet at 02 Resolution," *The Astronomical Journal*, vol. 117, no. 5, p. 2185, 1999.

[60] E. S. Perlman, W. B. Sparks, J. Radomski, C. Packham, R. S. Fisher, R. Piña, and J. A. Biretta, "Deep 10 micron imaging of M87," *The Astrophysical Journal Letters*, vol. 561, no. 1, p. L51, 2001.

[61] K. Asada and M. Nakamura, "The structure of the M87 jet: A transition from parabolic to conical streamlines," *The Astrophysical Journal Letters*, vol. 745, no. 2, p. L28, 2012.

[62] C. Cheung, D. Harris, *et al.*, "Superluminal radio features in the M87 jet and the site of flaring TeV gamma-ray emission," *The Astrophysical Journal Letters*, vol. 663, no. 2, p. L65, 2007.

[63] D. Harris, C. Cheung, J. Biretta, W. Sparks, W. Junor, E. Perlman, and A. Wilson, "The Outburst of HST-1 in the M87 Jet," *The Astrophysical Journal*, vol. 640, no. 1, p. 211, 2006.

[64] R. C. Walker, P. E. Hardee, F. B. Davies, C. Ly, and W. Junor, "The structure and dynamics of the subparsec jet in M87 based on 50 VLBA observations over 17 years at 43 GHz," *The Astrophysical Journal*, vol. 855, no. 2, p. 128, 2018.

[65] A. Abdo, M. Ackermann, M. Ajello, W. Atwood, M. Axelsson, L. Baldini, J. Ballet, G. Barbiellini, D. Bastieri, K. Bechtol, *et al.*, "Fermi Large Area Telescope gamma-ray detection of the radio galaxy M87," *The Astrophysical Journal*, vol. 707, no. 1, p. 55, 2009.

[66] C. Ly, R. C. Walker, and W. Junor, "High-frequency VLBI imaging of the jet base of M87," *The Astrophysical Journal*, vol. 660, no. 1, p. 200, 2007.

[67] K. Hada, M. Kino, A. Doi, H. Nagai, M. Honma, K. Akiyama, F. Tazaki, R. Lico, M. Giroletti, G. Giovannini, *et al.*, "High-sensitivity 86 GHz (3.5 mm) VLBI observations of M87: deep imaging of the jet base at a resolution of 10 Schwarzschild radii," *The Astrophysical Journal*, vol. 817, no. 2, p. 131, 2016.

[68] A. Abdo, M. Ackermann, M. Ajello, W. Atwood, L. Baldini, J. Ballet, G. Barbiellini, D. Bastieri, B. Baughman, K. Bechtol, *et al.*, "Fermi large area telescope view of the core of the radio galaxy Centaurus A," *The Astrophysical Journal*, vol. 719, no. 2, p. 1433, 2010.

[69] R. Nemmen, "The Spin of M87," *The Astrophysical Journal Letters*, vol. 880, no. 2, p. L26, 2019.

[70] C. Kuo, K. Asada, R. Rao, M. Nakamura, J. Algaba, H. Liu, M. Inoue, P. Koch, P. Ho, S. Matsushita, *et al.*, "Measuring mass accretion rate onto the supermassive black hole in M87 using faraday rotation measure with the submillimeter array," *The Astrophysical Journal Letters*, vol. 783, no. 2, p. L33, 2014.

[71] F. Aharonian, A. Akhperjanian, M. Beilicke, K. Bernlöhr, H.-G. Börst, H. Bojahr, O. Bolz, T. Coarasa, J. Contreras, J. Cortina, *et al.*, "Is the giant radio galaxy M 87 a TeV gamma-ray emitter?," *Astronomy & Astrophysics*, vol. 403, no. 1, pp. L1–L5, 2003.

[72] D. Berge, L. Rob, C. Boisson, P. Vincent, G. Rowell, E. Moulin, J. Osborne, F. Feinstein, H. Volk, S. Pita, *et al.*, "Fast variability of TeV gamma-rays from the radio galaxy M87," *Science*, vol. 314, no. astro-ph/0612016, p. 1424, 2006.

[73] J. Albert, E. Aliu, H. Anderhub, L. Antonelli, P. Antoranz, M. Backes, C. Baixeras, J. Barrio, H. Bartko, D. Bastieri, *et al.*, "Very high energy gamma-ray observations of strong flaring activity in M87 in 2008 February," *The Astrophysical Journal Letters*, vol. 685, no. 1, p. L23, 2008.

[74] Veritas Collaboration and VLBA 43 GHz M87 Monitoring Team and HESS Collaboration and MAGIC Collaboration *et al.*, "Radio imaging of the very-high-energy γ-ray emission region in the central engine of a radio galaxy," *Science*, vol. 325, no. 5939, pp. 444–448, 2009.

[75] V. Acciari, S. Ansoldi, L. Antonelli, A. Arbet Engels, C. Arcaro, D. Baack, A. Babić, B. Banerjee, P. Bangale, U. B. de Almeida, *et al.*, "Monitoring of the radio galaxy M 87 during a low emission state from 2012 to 2015 with MAGIC," *Monthly Notices of the Royal Astronomical Society*, 2020.

[76] Benbow, Wystan and VERITAS Collaboration, "Highlights from the VERITAS AGN observation program," in *AIP Conference Proceedings*, vol. 1792, p. 050001, AIP Publishing LLC, 2017.

[77] M. Lister, M. Aller, H. Aller, M. Hodge, D. Homan, Y. Kovalev, A. Pushkarev, and T. Savolainen, "MOJAVE. XV. VLBA 15 GHz total intensity and polarization maps of 437 parsec-scale AGN jets from 1996 to 2017," *The Astrophysical Journal Supplement Series*, vol. 234, no. 1, p. 12, 2018.

[78] A. Carramiñana, D. R. González, S. C. de León, and A. L. Longinotti, "A survey of Active Galaxies with the HAWC Gamma-ray Observatory," *arXiv preprint arXiv:1908.06831*, 2019.

[79] D. E. Harris, C. C. Cheung, Ł. Stawarz, J. Biretta, and E. S. Perlman, "Variability Timescales in the M87 Jet: Signatures of E 2 Losses, Discovery of a Quasi Period in HST-1, and the Site of TeV Flaring," *The Astrophysical Journal*, vol. 699, no. 1, p. 305, 2009.

[80] S. De Jong, V. Beckmann, S. Soldi, A. Tramacere, and A. Gros, "High-energy emission processes in M87," *Monthly Notices of the Royal Astronomical Society*, vol. 450, no. 4, pp. 4333–4341, 2015.

[81] F. Tavecchio and G. Ghisellini, "Spine–sheath layer radiative interplay in subparsec-scale jets and the TeV emission from M87," *Monthly Notices of the Royal Astronomical Society: Letters*, vol. 385, pp. L98–L102, 03 2008.

[82] M. Georganopoulos, E. S. Perlman, and D. Kazanas, "Is the core of M87 the source of its Tev emission? Implications for unified schemes," *The Astrophysical Journal Letters*, vol. 634, no. 1, p. L33, 2005.

[83] D. Giannios, D. A. Uzdensky, and M. C. Begelman, "Fast TeV variability from misaligned minijets in the jet of M87," *Monthly Notices of the Royal Astronomical Society*, vol. 402, no. 3, pp. 1649–1656, 2010.

[84] J.-P. Lenain, C. Boisson, H. Sol, and K. Katarzyński, "A synchrotron self-Compton scenario for the very high energy γ-ray emission of the radiogalaxy M87-Unifying the TeV emission of blazars and other AGNs?," *Astronomy & Astrophysics*, vol. 478, no. 1, pp. 111–120, 2008.

[85] A. Levinson and F. Rieger, " Variable TeV emission as a manifestation of jet formation in M87?," *The Astrophysical Journal*, vol. 730, p. 123, mar 2011.

[86] A. Reimer, R. Protheroe, and A.-C. Donea, "M 87 as a misaligned synchrotron-proton blazar," *Astronomy & Astrophysics*, vol. 419, no. 1, pp. 89–98, 2004.

[87] M. Reynoso, M. Medina, and G. Romero, "A lepto-hadronic model for high-energy emission from FR I radiogalaxies," *Astronomy & Astrophysics*, vol. 531, p. A30, 2011.

[88] N. Fraija and A. Marinelli, "Neutrino, γ-ray, and cosmic-ray fluxes from the core of the closest radio galaxies," *The Astrophysical Journal*, vol. 830, no. 2, p. 81, 2016.

[89] A. U. Abeysekara, A. Albert, R. Alfaro, C. Alvarez, J. D. Álvarez, R. Arceo, J. C. Arteaga-Velázquez, H. A. A. Solares, A. S. Barber, B. Baughman, N. Bautista-Elivar, *et al.*, "The 2hwc HAWC observatory gamma-ray catalog," *The Astrophysical Journal*, vol. 843, p. 40, jun 2017.

[90] A. U. Abeysekara, A. Albert, R. Alfaro, C. Alvarez, J. D. Álvarez, J. R. A. Camacho, R. Arceo, J. C. Arteaga-Velázquez, K. P. Arunbabu, D. A. Rojas, H. A. A. Solares, V. Baghmanyan, E. Belmont-Moreno, S. Y. BenZvi, C. Brisbois, K. S. Caballero-Mora, T. Capistrán, A. Carramiñana, *et al.*, "Measurement of the crab nebula spectrum past 100 TeV with HAWC," *The Astrophysical Journal*, vol. 881, p. 134, aug 2019.

[91] A. Abeysekara, A. Albert, R. Alfaro, C. Alvarez, J. Álvarez, R. Arceo, J. Arteaga-Velázquez, H. A. Solares, A. Barber, N. Bautista-Elivar, *et al.*, "Observation of the crab nebula with the HAWC gamma-ray observatory," *The Astrophysical Journal*, vol. 843, no. 1, p. 39, 2017.

[92] J. Matthews, "A Heitler model of extensive air showers," *Astroparticle Physics*, vol. 22, no. 5-6, pp. 387–397, 2005.

[93] K. Malone, *A Survey of the Highest-energy Astrophysical Sources with the HAWC Observatory*. The Pennsylvania State University, 2018.

[94] E. Dwek and F. Krennrich, "The extragalactic background light and the gamma-ray opacity of the universe," *Astroparticle Physics*, vol. 43, pp. 112–133, 2013.

[95] G. de Vaucouleurs, A. de Vaucouleurs, G. Harold Jr, R. J. Buta, G. Paturel, P. Fouqué, *et al.*, *Third reference catalogue of bright galaxies*, vol. 3. Springer Science & Business Media, 2013.

[96] M. Punch, C. W. Akerlof, M. F. Cawley, M. Chantell, D. Fegan, S. Fennell, J. Gaidos, J. Hagan, A. Hillas, Y. Jiang, *et al.*, "Detection of TeV photons from the active galaxy Markarian 421," *Nature*, vol. 358, no. 6386, pp. 477–478, 1992.

[97] The HAWC collaboration, A. Abeysekara, *et al.*, "A survey of active galaxies at TeV photon energies with the HAWC gamma-ray observatory," *Submitted to ApJ*, 2020.

[98] M. Ajello, W. Atwood, L. Baldini, J. Ballet, G. Barbiellini, D. Bastieri, R. Bellazzini, E. Bissaldi, R. Blandford, E. Bloom, *et al.*, "3FHL: The Third Catalog of Hard Fermi-LAT Sources," *The Astrophysical Journal Supplement Series*, vol. 232, no. 2, p. 18, 2017.

[99] A. Domínguez, J. R. Primack, D. Rosario, F. Prada, R. Gilmore, S. M. Faber, D. C. Koo, R. S. Somerville, M. Pérez-Torres, P. Pérez-González, *et al.*, "Extragalactic background light inferred from AEGIS galaxy-SED-type fractions," *Monthly Notices of the Royal Astronomical Society*, vol. 410, no. 4, pp. 2556–2578, 2011.

[100] A. Sarkar, J. Chluba, and E. Lee, "Dissecting the Compton scattering kernel I: Isotropic media," *Monthly Notices of the Royal Astronomical Society*, vol. 490, no. 3, pp. 3705–3726, 2019.

[101] S. Sahu, C. E. L. Fortín, and S. Nagataki, "Multi-TeV Flaring from High-energy Blazars: An Evidence of the Photohadronic Process," *The Astrophysical Journal Letters*, vol. 884, no. 1, p. L17, 2019.

[102] J. Biretta, C. Stern, and D. Harris, "The radio to X-ray spectrum of the M87 jet and nucleus," *The Astronomical Journal*, vol. 101, pp. 1632–1646, 1991.

[103] V. Despringre, D. Fraix-Burnet, and E. Davoust, "First millimeter mapping of the jet and nucleus of m 87," *Astronomy and Astrophysics-A&A*, vol. 309, pp. 375–380, 1996.

[104] J. C. Tan, H. Beuther, F. Walter, and E. G. Blackman, "A Search for Molecular Gas in the Nucleus of M87 and Implications for the Fueling of Supermassive Black Holes," *The Astrophysical Journal*, vol. 689, no. 2, p. 775, 2008.

[105] Y. Shi, G. H. Rieke, D. Hines, K. Gordon, and E. Egami, "Thermal and nonthermal infrared emission from M87," *The Astrophysical Journal*, vol. 655, no. 2, p. 781, 2007.

[106] W. Sparks, J. Biretta, and F. Macchetto, "The jet of M87 at tenth-arcsecond resolution: optical, ultraviolet, and radio observations," *The Astrophysical Journal*, vol. 473, no. 1, p. 254, 1996.

[107] H. L. Marshall, B. Miller, D. Davis, E. Perlman, M. Wise, C. Canizares, and D. Harris, "A high-resolution X-ray image of the jet in M87," *The Astrophysical Journal*, vol. 564, no. 2, p. 683, 2002.

[108] K.-W. Wong, R. S. Nemmen, J. A. Irwin, and D. Lin, "Hard X-ray Emission from the M87 AGN Detected with NuSTAR," *The Astrophysical Journal Letters*, vol. 849, no. 1, p. L17, 2017.

[109] J. Aleksić, E. Alvarez, L. Antonelli, P. Antoranz, M. Asensio, M. Backes, J. Barrio, D. Bastieri, J. B. González, W. Bednarek, *et al.*, "MAGIC observations of the giant radio galaxy M 87 in a low-emission state between 2005 and 2007," *Astronomy & Astrophysics*, vol. 544, p. A96, 2012.

[110] Y. Yamada, M. Uemura, R. Itoh, Y. Fukazawa, M. Ohno, and F. Imazato, "Variations of the physical parameters of the blazar Mrk 421 based on the analysis of the spectral energy distribution," *arXiv preprint arXiv:2003.08016*, 2020.

[111] W. H. Press, S. A. Teukolsky, W. T. Vetterling, and B. P. Flannery, *Numerical recipes 3rd edition: The art of scientific computing*. Cambridge University Press, 2007.

[112] B. R. Ryan, J. C. Dolence, and C. F. Gammie, "bhlight: general relativistic radiation magnetohydrodynamics with Monte Carlo transport," *The Astrophysical Journal*, vol. 807, no. 1, p. 31, 2015.

[113] F. Tavecchio, L. Maraschi, and G. Ghisellini, "Constraints on the physical parameters of TeV blazars," *The Astrophysical Journal*, vol. 509, no. 2, p. 608, 1998.

[114] S. S. Kimura and K. Toma, "Hadronic High-energy Emission from Magnetically Arrested Disks in Radio Galaxies," *arXiv preprint arXiv:2003.13173*, 2020.

[115] G. Ghisellini, F. Tavecchio, and M. Chiaberge, "Structured jets in TeV BL Lac objects and radiogalaxies-Implications for the observed properties," *Astronomy & Astrophysics*, vol. 432, no. 2, pp. 401–410, 2005.

[116] MAGIC Collaboration, V. A. Acciari, S. Ansoldi, L. A. Antonelli, A. A. Engels, D. Baack, A. Babić, B. Banerjee, U. B. de Almeida, J. A. Barrio, J. B. González, W. Bednarek, L. Bellizzi, E. Bernardini, A. Berti, J. Besenrieder, W. Bhattacharyya, C. Bigongiari, A. Biland, O. Blanch, G. Bonnoli, Bošnjak, G. Busetto, R. Carosi, G. Ceribella, M. Cerruti, Y. Chai, A. Chilingarian, S. Cikota, and others., "Testing two-component models on very-high-energy gamma-ray emitting BL Lac objects," 2020.

List of Figures

List of Tables